Master's thesis

2019

Martin Madsen

Master's thesis

NTNU
Norwegian University of
Science and Technology
Faculty of Natural Sciences
Department of Materials Science and Engineering

NTNU
Norwegian University of
Science and Technology

Martin Madsen

Ceramic matrix composites based on silicon carbide and carbon fibers

June 2019

NTNU
Norwegian University of
Science and Technology

NTNU
Norwegian University of
Science and Technology

Ceramic matrix composites based on silicon carbide and carbon fibers

Martin Madsen

Chemical Engineering and Biotechnology
Submission date: June 2019
Supervisor: Kjell Wiik, IMA
Co-supervisor: Nikola Kanas, IMA

Norwegian University of Science and Technology
Department of Materials Science and Engineering

Acknowledgements

First I would like to thank my supervisor Kjell Wiik and co-supervisor Nikola Kanas at NTNU for excellent advice and discussions during the course of this project. From Saint-Gobain Ceramic Materials AS Lillesand I would like to thank Pål Runde for the chance to work with silicon carbide, Vidar Johannessen for sound advice on silicon carbide and Stephen Røstad Rugholm for much needed technical support. A special thanks goes to everyone at the Department of Research and Development at Saint-Gobain Ceramic Materials AS Lillesand for a warm welcome during my internship. Furthermore I would like to thank everyone involved with the project and who have helped me with the instruments at the Department of Material Science and Technology at NTNU. Finally I would like to thank everyone in the Functional Materials and Materials Chemistry Research Group for interesting weekly seminars and good advice during the course of this project.

Trondheim, June 2019

Martin Madsen

Abstract

Silicon carbide is well known for its excellent mechanical and thermal properties, which provide a wide range of industrial applications. SiC is, however, a brittle ceramic and even the smallest cracks can prove catastrophic. One way to address this problem is to reinforce the ceramic matrix with fibers, so called ceramic matrix composites. This master thesis will investigate the sinterability of SiC powders with 0, 10 and 15 vol% carbon fiber content using the spark plasma sintering method. After an optimization step to introduce fibers into the matrix, the three samples were sintered at 1850 ℃ with a pressure of 20 MPa and a holding time of 5 minutes. The samples were then polished and characterized. Phase composition measured with X-ray diffraction showed no significant change during sintering with fiber addition. The relative densities measured with Archimedes method showed a decrease from 92 % to 88 % with fiber addition. Vickers microindentation was used to measure the hardness and fracture toughness of the samples. The hardness showed a decrease with fiber addition and had very large local variations due to the presence of fibers. The fracture toughness increased with increasing fiber content and likewise showed local variations due to the fibers. The strength measured with the ring-on-ring method decreased with fiber addition. The bonds between the fibers and the matrix showed both chemical and mechanical character. During fracture, the fibers showed both fiber pullout and crack bridging as toughening mechanisms, dependent on their orientation to the fracture.

Table of Contents

1 Introduction

1.1 Background and motivation

Silicon carbide (SiC) is a light and highly covalent non-oxididic ceramic, formed at high temperatures by reaction between silica and carbon. The first documented natural occurrence of SiC was in a meteorite in Arizona, which was discovered by Dr. Moisson in 1893 [1]. It was, however, accidentally produced by E.G. Acheson already in 1891 [2], who was instead trying to make artificial diamonds by heating up clay by electric heat. The new material, called carborundum, had interesting diamond-like properties and the process, now called the Acheson process, was quickly patented by Acheson. Although SiC can be found naturally near diamond deposits [3], almost all of industrial SiC is made by the Acheson process.

SiC has a variety of excellent properties that grant it a wide range of applications. It is a very hard ceramic, almost as hard as diamond. This, combined with its relatively low cost compared to diamond, makes it an excellent abrasive and cutting material. SiC is also used as a refractory material in high temperature furnaces due to its high thermal shock resistance and chemical stability, even at elevated temperatures. SiC is also a valid candidate for applications where strength and structural stability is required. The defense industry uses dense sintered SiC for armour plating due to its low density and high strength. When doped SiC can also act as a semiconductor and be used as a heating element in furnaces. Some more novel applications include diesel particle filters and substrate for satellite mirrors.

While SiC is a versatile material, it has a major flaw. Like many other hard ceramics, SiC is very brittle and suffers catastrophic failure even with small cracks. For applications structural stability and strength are of importance, this provides a challenge, as the material is rendered useless after only a few impacts. One way to solve this problem is by increasing the fracture toughness of SiC by introducing carbon fibers into the SiC matrix, creating a so called ceramic matrix composite (CMC). This can increase the energy needed for fracture by various toughening mechanisms between the matrix and the fibers. The fibers need to be introduced into the matrix without degrading the other properties of SiC. For most applications a fine silicon carbide powder has to be sintered into a dense, solid ceramic. This can also be applied to the production of CMC with pressure sintering, such as spark plasma sintering (SPS).

1.2 Scope of the work

This work aims to identify the sinterability of SiC powders with various carbon fiber content using a SPS. The precursor powders are provided by Saint-Gobain Ceramic Materials, with 0, 10 and 15 vol% carbon fiber content. The sintered products will be characterized for density, phase composition, microstructure, hardness and fracture toughness, and flexural strength using the Archimedes' method, X-ray diffraction (XRD), electron backscatter diffraction (EBSD), Vicker's microindentation and ring-on-ring method, respectively. The bonding and interactions between the fibers and the matrix will be analyzed with the scanning electron microscope (SEM). The results will be discussed and the possibilities for further investigation will be looked into.

2 Theory

2.1 Silicon Carbide

2.1.1 Structure of SiC

The structure of SiC corresponds to a closed packing of Si atoms with C in half of the tetrahedral sites. SiC comes in a wide variety of different polytypes. The common building blocks of these polytypes are SiC_4 and CSi_4 tetrahedra and the difference bewteen the polytypes comes from the stacking order of these tetrahedra. The number of polytypes exceeds 250 [4], but the most common ones are the cubic 3C, the hexagonal 4H and 6H and the rombohedral 15R. Here the number denotes the number of layers in the unit cell and the letter refers to the crystal structure. The SiC structures are commonly referred to as α-SiC and β-SiC, where α-SiC is the combination of the hexagonal polytypes while β-SiC is the 3C polytype.

The stacking order of the layers of tetrahedra determines the polytype. 3C has a stacking sequence of ABC with all the tetrahedra pointing in the same direction. This results in a cubic zinc blende structure. The hexagonal polytypes also need a rotation around the [111] direction to return to the original position. This rotation is denoted by a dash in the stacking sequence. For 4H the sequence becomes ABA'C' and 6H becomes ABCB'A'C'. Accordingly the crystal structure corresponds to the hexagonal wurtzite structure. The rombohedral 15R polytype has a more complicated stacking sequence, ABCB'A'BCAC'B'CABA'C'. An illustration of the 3C and 6H polytypes can be seen in Figure 2.1 and 2.2, respectively. More details on the crystallography of the most common polytypes are given in Table 2.1.

When SiC is formed, it is commonly accepted that it takes the β-SiC structure at lower temperatures and the α-SiC structure at higher temperatures. In reality this is not that simple and different theories have been presented by Jepps *et al.* [7] and Inomata *et al.* [8]. The 3C polytype is the most stable polytype at lower temperatures, around 1400 ℃ to 1700 ℃ followed by 4H up to 2100 ℃. 6H is stable above 2100 ℃ with 15R being stable at even higher

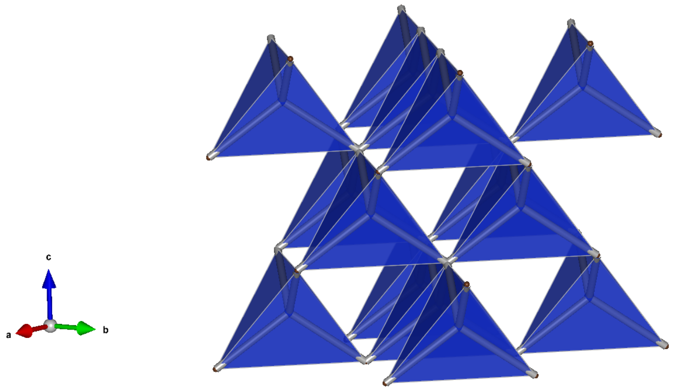

Figure 2.1: Visualization of the 3C polytype of SiC with a cubic zinc blende structure using the VESTA program [5]. The building blocks of the structure are SiC_4 tetrahedra.

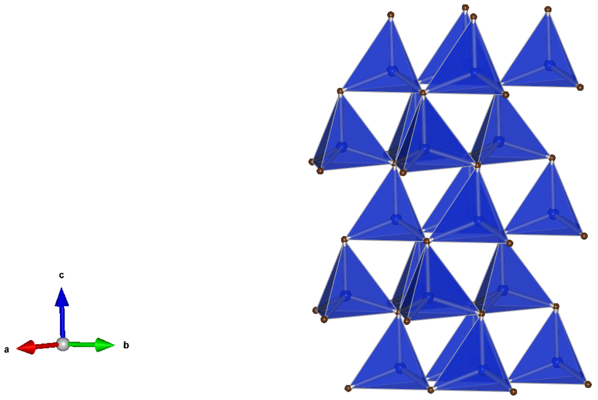

Figure 2.2: Visualization of the 6H polytype of SiC with a hexagonal wurtzite structure using the VESTA program [5]. The building blocks of the structure are SiC_4 tetrahedra.

Table 2.1: Crystallography of the most common SiC polytypes 3C, 4H, 6H and 15R at room temperature [6].

Property	3C	4H	6H	15R
Crystal structure	Zinc blende	Wurtzite	Wurtzite	Rombohedral
Space group	F-43m	P63mc	P63mc	R3m
Lattice parameter a [Å]	4.3596	3.0730	3.0806	12.691
Lattice parameter c [Å]	-	10.053	15.1173	-

temperatures. Beside temperature, impurities and growth conditions also seem to affect the stability of the polytypes, as suggested by Knippenberg *et al.* [9]. The growth rate of β-SiC is increased with overabundance of Si and N. Kistler-De Coppi *et al.* [10] concluded that additions such as aluminum, boron and nitrogen stabilise different polytypes and inhibit the growth of the crystals in certain directions, while nitrogen addition inhibited the 6H to 4H transformation. There is also conflicting consensus about the reversibility of β-SiC to α-SiC. Jepps *et al.* [7] have shown the formation of 3C polytype from 6H in the presence of nitrogen, while Knippenberg *et al.* [9] argued that the transformation is irreversible.

2.1.2 Properties of Silicon Carbide

Silicon carbide is a relatively light ceramic. The presence of strong covalent bonds between the Si and C atoms makes it an incredibly hard material corresponding to 9 on the Mohs scale. In fact there are only four other materials harder than SiC: diamond, cubic boron nitride and boron carbide. While being a hard ceramic, it still has a relatively high fracture toughness. Its thermal properties are also of interest. SiC has a high thermal shock resistance owing to its high thermal conductivity and low thermal expansion coefficient. It can withstand high temperatures in reducing atmosphere, as SiC does not melt, but decomposes into silicon vapor and graphite at higher temperatures. While being an insulator in the undoped state, when doped it acts as a semiconductor. SiC also has excellent chemical stability, reported to be stable in hydrofluoric acid and in a mixture of hydrofluoric, sulfuric and nitric acids [11]. Some of these properties are listed in Table 2.2 for the most common polytypes of SiC, 3C and 6H.

Table 2.2: The principal properties of the most common SiC structures, 3C and 6H [2, 6, 12, 13].

Property	β-SiC (3C)	α-SiC (6H)
Density $[\mathrm{g/cm^3}]$	3.166	3.211
Hardness $[\mathrm{GPa}]$	-	29
Young's modulus $[\mathrm{GPa}]$	392	410
Fracture toughness $[\mathrm{MPa}\sqrt{\mathrm{m}}]$	-	4.6
Thermal expansion coefficient at 300K $[\mathrm{K}^{-1}]$	3.5$\cdot 10^{-6}$	4-5$\cdot 10^{-6}$
Thermal conductivity $[\mathrm{W/mK}]$	320	490
Band gap at 4K [eV]	2.390	3.023

2.1.3 Production of Silicon Carbide

In 1891 G.E. Acheson tried producing artificial diamond by fusing together clay and coke. The result was a blue crystal and he called it carborundum, because he thought the product was a result of a reaction between carbon in the coke and alumina in the clay [14]. It was later found to be a reaction between carbon and silica. The process was patented, made more efficient via electrical heating and called the Acheson process. The process still remains, to this day, highly inefficient, with only about 10 to 15 per cent of the charge being successfully converted into SiC [15]. Since then there have been attempts to find new ways of making SiC but none have been able to compete with the Acheson process, which has been scaled up significantly. Today almost all silicon carbide is produced by this process.

The oven is an open electrical resistance oven with electrodes on both sides. It is often a few tens of meters long with a diameter of around 3 m. The electrodes are connected with a carbon core, most commonly petrol coke. Quartz sand is laid around the core so the core is completely covered by the sand. A voltage is applied and a current flows through the carbon core. The coke heats up due to resistance and peaks at around 1700-2500 $^\circ\mathrm{C}$, depending on the type and quality of silicon carbide that is desired. Carbon starts to react with the silicon in the quartz sand and the overall reaction is described by equation 2.1.

$$\mathrm{SiO_2(s) + 3\,C\,(s) \longrightarrow SiC\,(s) + 2\,CO\,(g)} \tag{2.1}$$

The reaction mechanism is complex and proceeds via gaseous species according to equations 2.2-2.5 [14].

$$\mathrm{SiO_2(s) + C\,(s) \longrightarrow SiO\,(g) + CO\,(g)} \tag{2.2}$$

$$\mathrm{SiO_2(s) + CO\,(g) \longrightarrow SiO\,(g) + CO_2(g)} \tag{2.3}$$

$$\mathrm{C\,(s) + CO_2(g) \longrightarrow 2\,CO\,(g)} \tag{2.4}$$

$$\mathrm{2\,C\,(s) + SiO\,(s) \longrightarrow SiC\,(s) + CO\,(g)} \tag{2.5}$$

Hence, managing the amount of gas in the furnace becomes an important task. The carbon monoxide gas is often burned to carbon dioxide to prevent buildup of the toxic gas and blow-outs in the furnace. This gives the furnace a characteristic blue flame, as seen in Figure 2.3.

Figure 2.3: The characteristic blue flame of the Acheson furnace, a result of carbon monoxide burn-off [16].

The middle of the core remains as carbon, while a shell of α-SiC is formed around it. The particle size goes radially outwards from coarse to fine and the quality of the product declines likewise. A shell of β-SiC can form just before an outer layer of unreacted sand at the outside. Temperature can be used to control the amount of α-SiC and β-SiC present, with higher temperatures favoring α-SiC. A cross section of the furnace is visualized in Figure 2.4.

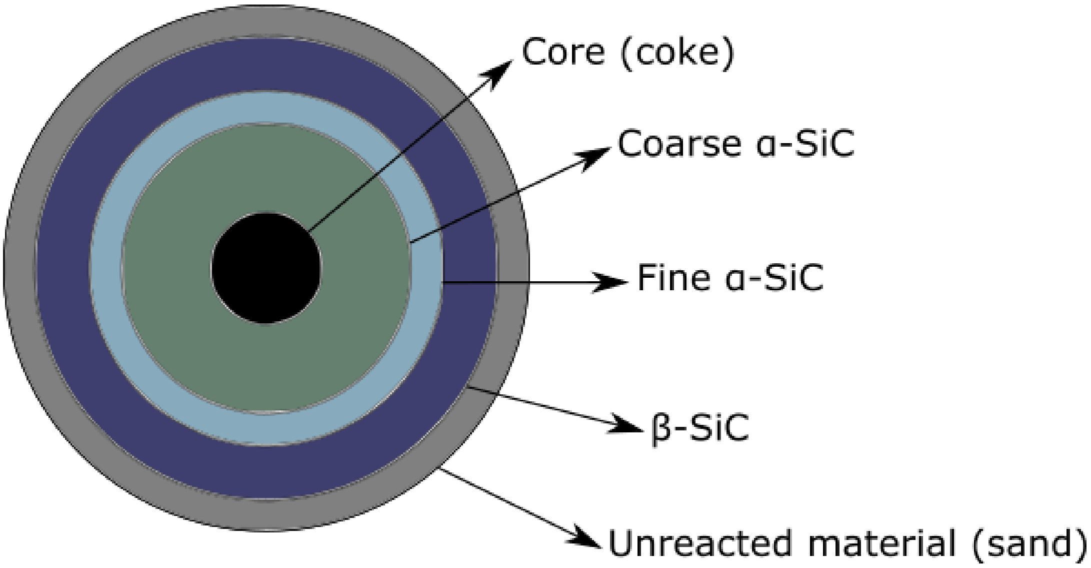

Figure 2.4: A visualization of the cross section of the oven in the Acheson process.

The process is carried out in batches, taking about 40-60 hours, while multiple furnaces are running in cycles to ensure efficiency. After the process is completed, the furnace is cooled and the quality product is collected. Undesired and unreacted material is recycled into another oven. Different ovens are used depending on the purity of the charge. High-purity and new charge is used in so-called "green ovens", while recycled charge is used in so-called "black ovens". This ensures the quality of the high purity products. Depending on the types of impurities present in the final product, it can have different colours, ranging from green with nitrogen to dark blue and black with aluminium [14], hence the notation of the ovens. Pure SiC is colorless, but it is difficult to produce due to the solubility of nitrogen from the air into SiC. After the product is collected, it is usually crushed and milled to semi-fine particles for further processing depending on the application.

2.2 Solid state Sintering

2.2.1 Pressureless Sintering

Mechanisms and driving forces of sintering

Solid state sintering is a form of sintering, where a solid material in powder form undergoes heat treatment over a period of time and becomes dense with the formation of bonds between particles and removal of pores [17]. Sintering is thermodynamically driven by reduction of the free energy of the system, either by surface energy reduction, applied pressure or chemical reactions. In pressureless sintering only heat is added to the system, so the only way to reduce the energy of the system is to reduce the surface energy of the particles [18].

The surface energy of the system is mainly is reduced by the reduction of surface area. In solid state sintering this happens due to mass transport and leads to either densifying or coarsening of the material. Densification is achieved by shrinkage of the material by pore removal and formation of grain boundaries. Coarsening happens due to Ostwald ripening, where smaller particles are consumed by larger ones. This leaves the overall volume of the material unchanged and no densification occurs. These two mechanisms are always competing and can by controlled with temperature. They can further be divided into mass transport mechanisms, as seen in Table 2.3.

Table 2.3: Mass transport mechanisms categorized by source of matter and densifying/non-densifying character.

Mechanism	Source of matter	Densifying	Non-densifying
Surface diffusion	Surface		✓
Lattice diffusion	Surface		✓
Vapour transport	Surface		✓
Grain boundary diffusion	Grain boundary	✓	
Lattice diffusion	Grain boundary	✓	
Plastic flow	Dislocations	✓	

Both of these mechanisms are driven by diffusion which is governed by Fick's first law given in equation 2.6.

$$J_i = -D_i \frac{c}{R \cdot T} \nabla \mu_i \tag{2.6}$$

Here J is the flux of a species, D is the diffusion constant, c is the concentration, R is the gas constant, T is the temperature and μ is the chemical potential. As seen from the equation, matter moves from a high chemical potential region to a low chemical potential region. Surface curvature has a significant role in mass transport. On a convex surface, where the curvature is positive, the atom will have a higher chemical potential than if the atom was on a flat surface. Likewise, if the atom is on a concave surface, where the curvature is negative, the atom will have a lower chemical potential than on a flat surface. This, coupled with Fick's first law, means that matter will diffuse from a convex surface to a concave surface, meaning that when enough time has passed, the surface will become flat. Vacancies move the opposite way, from concave to convex surface. This is illustrated in Figure 2.5.

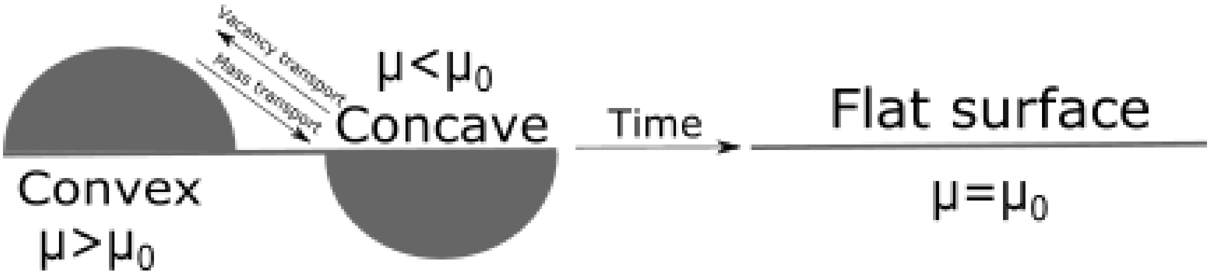

Figure 2.5: The transport of material goes from the convex surface, with a higher chemical potential, to a concave surface, with a lower chemical potential. Given time, this will result in a flat surface. Vacancies move the opposite way.

The extent of the curvature also has implications on the driving forces of pore removal and grain growth. The relationship between the solid particle and the pore can be described by equation 2.7.

$$\gamma_{GB} = 2\gamma_{SV} cos(\frac{\theta}{2}) \tag{2.7}$$

Here γ_{GB} is the grain boundary energy, γ_{SV} is the solid/vapour interface energy and θ is the dihedral angle. When the surface is concave, the dihedral angle is less than 180 °and the pore will close. The opposite is true for convex surface. When the pore is surrounded by many grains, the surface will be flat and the driving force for pore closure is lost [19]. This is analogous for grain growth.

Sintering stages

Solid state sintering is usually divided into three stages, illustrated in Figure 2.6. In the initial stage the particles rearrange and contact is formed between the particles. In the contact points necks start to form as surface diffusion and gas vaporization-condensation are the dominating mass transport mechanisms. The increase in relative density in this stage is only about 5 %. The end of the initial stage is when necks have formed and start to grow.

Figure 2.6: An illustration of the three sintering stages. In the initial stage the particles rearrange and necks start to form. In the intermediate stage the pores size is reduced with diffusion and shrinkage occurs. In the final stage the porosity is closed and pores are removed by vacancy diffusion and grain boundary movement.

The intermediate stage is where most of the densification occurs. As necks grow, open pores begin to shrink while grain boundaries are formed and the material becomes denser. The dominating mass transport mechanisms here are grain boundary and lattice diffusion. Usually the relative density increases from 65% to as high as 92%. At this point the pores are closed and grain growth will take over, signifying the end of the intermediate stage.

The final stage is when the porosity is closed and the pores are either located at the triple points between grains or inside grains themselves. Grain growth is dominant and further densification is achieved by removal of the pores at the grain boundaries by vacancy diffusion. If the grain boundary movement is too fast, pores can be trapped inside the grains. The pores that are isolated inside grains can not be removed and should be avoided by proper control of the grain growth rate. A final density of the material is achieved during this stage. The change in relative density during each of the three stages is illustrated in Figure 2.7.

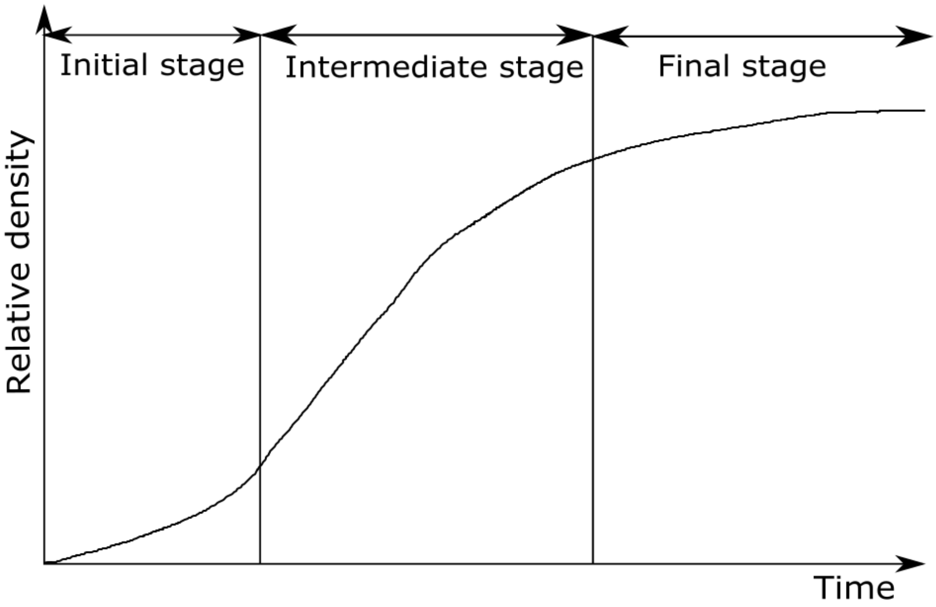

Figure 2.7: Change of relative density during the three sintering stages. The initial stage sees a density change of 60% to 65%, the intermediate stage from 65% to 92% and the final stage from 92% close to 100%.

2.2.2 Pressure-assisted sintering

Hot-pressing

Besides temperature and chemical reactions, pressure can be applied during sintering. One method that utilizes pressure applied along with temperature is hot pressing. The same mechanisms are present in hot pressing as are in pressureless sintering, but the presence of pressure enhances the driving forces of densification significantly. In the initial stage pressure helps with the rearrangement of particles, which in turn help the particles to make contact with each other and start the densification. The grains tend to flatten out and have a preferred growth direction perpendicular to the direction of the applied pressure. Higher densities can be achieved and sintering time can be reduced with hot pressing. Additionally due to enhanced driving forces, the need for sintering additives can be reduced. As a disadvantage, hot pressing can be more expensive as dies and punches need to be utilized for pressure addition and the furnaces tend to be more complex compared to pressureless sintering.

Spark plasma sintering

Spark plasma sintering, also known as field-assisted sintering, is a another pressure-assisted sintering method that utilizes electric current for heating. A low voltage is applied and direct current is pulsed through electrodes that are in contact with a graphite die. As graphite is conductive, the current then passes through the die and heats it up by resistance. If the powder in the die is also conductive, the current will directly pass through the material and heat it directly. This in turn allows the method to achieve very rapid heating rate and reduce sintering time from hours to as low as a few minutes [20]. With the use of nanopowders and applied pressure, near theoretical densities have been achieved with little grain growth and clean grain boundaries [21, 22].

The system consists of pistons that apply mechanical load by hydraulic pressure and at the same time act as high power electrodes for the current to pass through. The electrodes are usually graphite electrodes. The voltage applied is usually lower than 10 V, while the current can reach as high as 10 kA and the pressure ranges from 50 kN to 250 kN [23]. The current is pulsed on and off with intervals of a few milliseconds, usually 12 ms on and 6 ms off. Heating rates can reach up to 1000 °C/min, depending on the contact geometry and material of the die and powder. Temperatures can go up to 2400 °C for graphite dies. The cooling rate is slower, but can be increased with external cooling. Either thermocouples, for low temperature, or pyrometers, for high temperature, are used for temperature measurement. The chamber itself can be vacuumed to low or high vacuum, resulting in either reduced or inert atmosphere. External water cooling and carbon wool is used to keep the chamber from overheating. A schematic illustration of the SPS system is shown in Figure 2.8.

The mechanisms and interaction between the current and powder are not fully understood. The name spark plasma sintering would imply that there is a formation of plasma

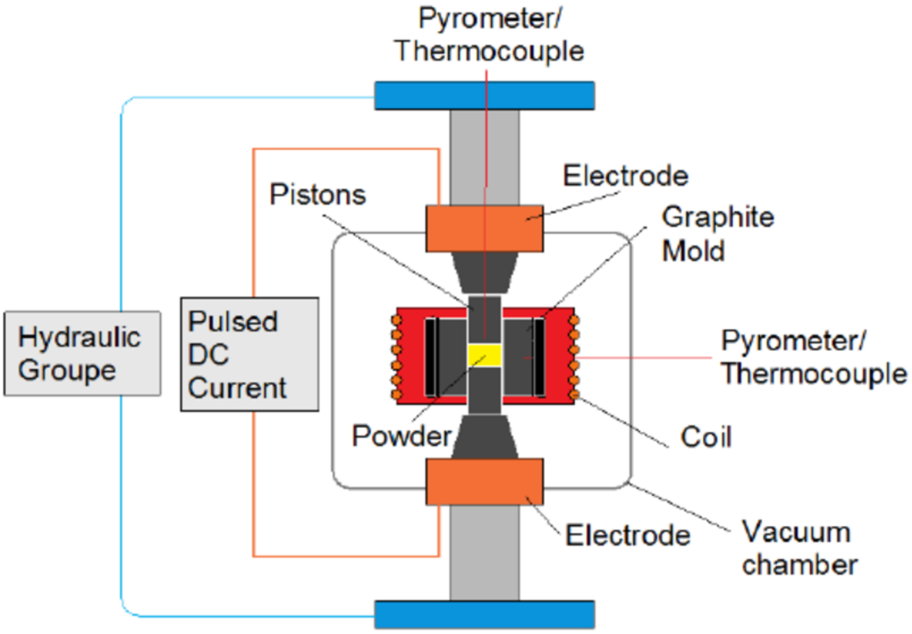

Figure 2.8: A schematic diagram of a SPS oven [24].

and electric arcs between the particles, but both of these have been reported to be missing by Hulbert *et al.* [25]. Others have claimed that there indeed is momentary spark plasma generated on the microgaps in the powder, like reported by Zhang *et al.* [26]. The current itself seems to flow along preferred percolating paths, due to the inhomogeneus nature of the powder. The Joule heating occurs more efficiently along these paths and creates hot zones, which can become much hotter than the set sintering temperature. The sintering mechanisms are dominated by local temperature gradients, rather than partial melting and crystallization found in conventional sintering. The fingerprint of these paths can be found in the final microstructure. The evolution of density and the microstructure of nanocrystalline silicon along with corresponding simulations were studied by Schwesig *et al.* [27].

Despite the lack of clear understanding of the mechanisms present in the process, SPS is widely used as a sintering method for novel and functional materials. The rapid heating and low sintering time contribute to highly dense and homogeneous final product.

2.2.3 Sintering of SiC

Silicon carbide is difficult to sinter to high densities by conventional methods. This is mainly due to strong bonds between Si and C due to the highly covalent character of SiC. This inhibits vacancy diffusion and leads to a low self diffusion in SiC. The mass transport mechanisms that are dominant during sintering are surface diffusion and vapour transport. Those lead to coarsening of the grains and don't contribute to densification. To achieve high densities, high temperature and pressure needs to be applied by either hot-pressing or spark plasma sintering. A sintering temperature of 2500 °C and a pressure of 50 kbars was used by Nadeau [28] to achieve near theoretical density. These values are too high for most practical cases, so sintering additives are usually added to the precursor powders to enhance the densification processes. For solid-state sintering carbon and boron are the most used additives. A small amount of these will significantly increase the final density, even at lower temperatures and pressure.

In recent years, SPS technology has also been used to sinter SiC to high densities with and without the use of sintering additives, with lower sintering temperatures than conventional sintering. Tamari *et al.* managed to achieve 98 % relative density of a SiC powder with alumina and yttria as sintering additives [29]. They used a sintering temperature of 1800 °C with a holding time of 5 minutes and an applied pressure of 30 MPa. Yamamoto *et al.* managed to sinter a nanopowder of SiC without additives to 98 % relative density at 1700 °C with an applied pressure of 40 MPa [30]. Hayun *et al.* sintered a SiC powder with an average grain size of 0.55 μm without additives at 2050 °C with an applied pressure of 69 MPa and a holding time of 10 min [31]. They achieved a relative denisity of 98 %.

Carbon addition

Carbon is one of the sintering additives used for sintering silicon carbide. Many forms of carbon are used, but the most prevalent are carbon black and phenolic resin. Carbon black in itself acts as the carbon source, while resin pyrolyses into graphite during sintering. Prochazka [32] proposed that the silica that forms on the surface of the SiC particles is removed by carbon by the a two-step reaction at 1520 °C shown in equations 2.8 and 2.9.

$$\mathrm{SiO_2(s) + C\,(s) \longrightarrow SiO\,(g) + CO\,(g)} \tag{2.8}$$

$$\mathrm{SiO\,(g) + 2\,C\,(s) \longrightarrow SiC\,(s) + CO\,(g)} \tag{2.9}$$

Silica can also reduce at 1870 °C by the reaction given in equation 2.10.

$$\mathrm{2\,SiO_2(s) + SiC\,(s) \longrightarrow 3\,SiO\,(s) + CO\,(g)} \tag{2.10}$$

The formation of a network of pores is also linked to SiO [33]. Apart from removal of silica, carbon addition has also been shown, by Datta *et al.* [34], to increase diffusivity in SiC. The theory is that carbon reduces the amount of Si in the atmosphere and thus increases the amount of Si vacancies. This, in turn, increases the bulk diffusivity. Empirically, the amount of carbon added to reach highest density is around 4 wt% [35].

Boron addition

Boron is another additive that increases the final density of sintered SiC. Boron can either be intorduced to the powder in elemental form, in the form of boron carbide, B_4C, or as boron nitride, BN, as shown by Prochazka [32] and Murata *et al.* [36]. The solubility of of the boron source needs to be taken into account to determine the amount of the boron source needed to achieve maximum density. Murata *et al.* [36] also found out that there is a decline in density after the solubility limit of the boron source in SiC is reached. For boron carbide it was 0.5 wt% and for boron nitride it was 1.25 wt% [36].

These are mostly empirical numbers and while it is clear that boron addition increases density, the exact mechanisms involved are less clear. The leading theory is that boron substitutes both silicon and carbon in the SiC matrix, as reported by Datta *et al.* [34] and confirmed by Tajima *et al.* [37]. This is due to their relatively similar covalent radii. Carbon substitution is somewhat favored due to smaller radii difference with boron, while the bonds created between boron and carbon are more stable than those formed between boron and silicon, favoring silicon substitution. Since the radii of the atoms differs somewhat, vacancies are formed due to the frustration of the lattice. This in turn increases the self diffusion of SiC via vacancies and enhances overall densification.

2.3 Ceramic Matrix Composites

This will be a general and brief overview on ceramic matrix composites.

Ceramics in general are a versatile group of materials with a wide range of useful properties and applications. What most of the materials in this class suffer from, is brittleness. Most ceramic materials have low resistance to fracture and when a crack appears the failure is often catastrophic. In order to improve the mechanical reliability of ceramics, their fracture toughness needs to be improved. One way is to include fibres of a material with different properties into the matrix of the host material.

Composites are a class of materials, where useful properties of different materials are used in a way that overall improves the properties of the combination of these materials contra when they are on their own [38]. Early composites include plywood and concrete. In recent history, more complex forms of composites have been made, for different applications. One way to class composites is to define what type of matrices are the host of the material. These include metals for metal matrix composites, polymers for polymer matrix composites and the topic of this project, ceramics for ceramic matrix composites. The guest material is usually continuous or short fibres made from carbon, silicon carbide or alumina, depending on the application. A schematic illustration of different composite materials is given in Figure 2.9. The fibers can be present in the precursor powder and then sintered or introduced into the matrix with liquid infiltration. The composite material usually has higher strength and resistance to failure than the matrix itself owing to different toughening mechanisms, which overall increase the energy needed for the crack to initiate and propagate. These will be discussed in the next section.

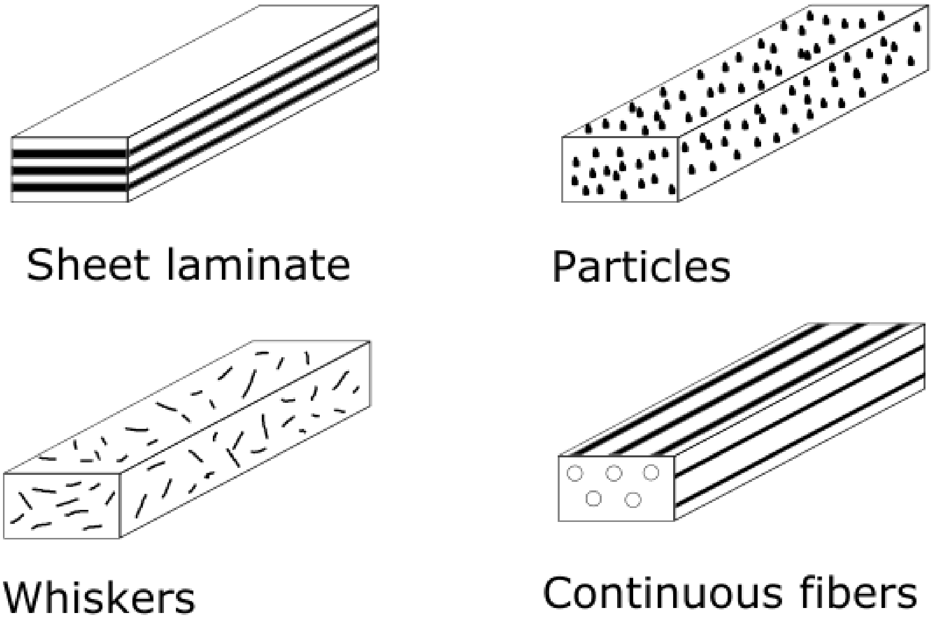

Figure 2.9: A basic illustration of different composite types.

2.3.1 Fracture Toughening

The main function of fibers in CMC is to increase the toughness of the matrix material. Depending on the type and dimensions of the fibre, there are three main ways the resistance to cracking can be increased: fiber pullout, crack bridging and crack deflection. The type of toughening mechanism depends largely on the bonding between the fiber and matrix as well as the way the crack hits the fiber. Each of these will increase the energy needed for the crack to grow and therefore slow down the propagation of the crack. The main goal is to prevent catastrophic failure.

When a crack encounters an obstacle, like a harder particle, the energy needed to pierce through that obstacle is greater than the energy needed to change the direction of propagation. The crack is deflected around the obstacle and the path of propagation is obstructed. This is called crack deflection and the result is a higher energy and time requirement before a fracture can occur. An illustration of this mechanism is given in Figure 2.10a.

When a fiber and the matrix are not too rigidly bonded, some of the energy needed

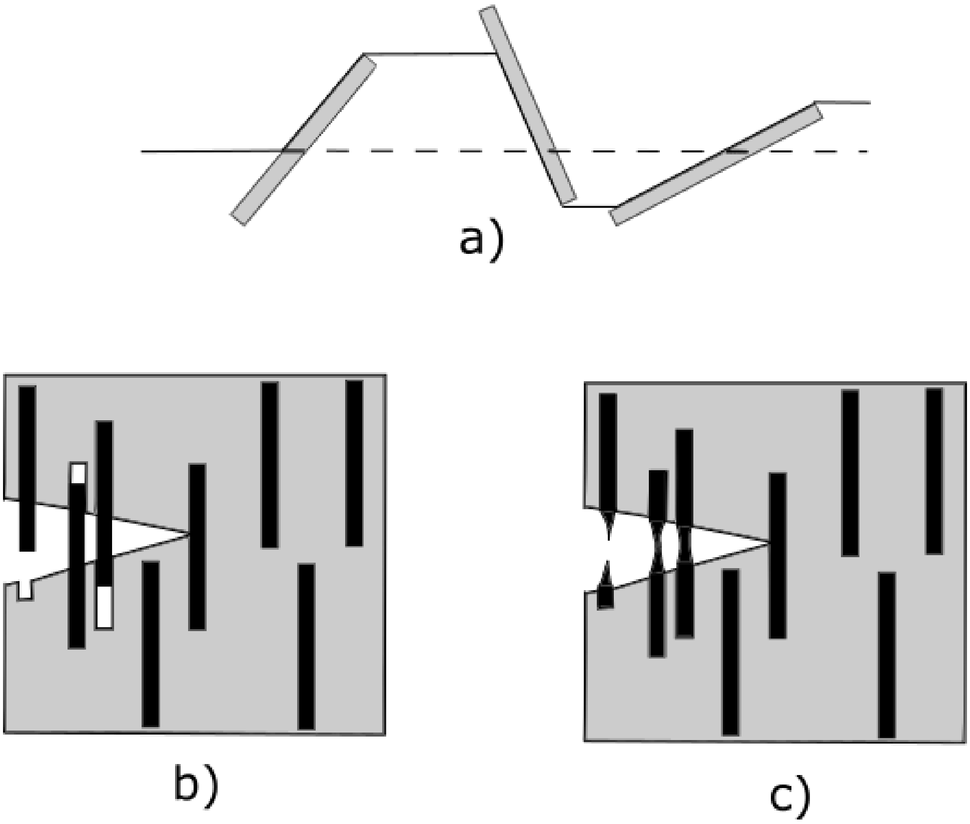

Figure 2.10: The three main toughening mechanisms a) crack deflection, b) fiber pullout and c) crack bridging.

to propagate a crack is instead absorbed by debonding the fiber from the matrix. This is called fiber pullout. Along with the debonding energy, the fiber will also move, causing friction and absorbing even more energy. The result is that it takes more energy to pull apart the matrix. An illustration of this mechanism is given in Figure 2.10b.

When the fibers are ductile, after a certain energy has been used to pull the fibers out, the fibers can start plastically deforming and bridge the gap, holding together the matrix. This is called crack bridging. The amount of energy that can be absorbed this way depends on the ability for fibers to plastically deform. This is a great way to halt the propagation of cracks, since a lot more energy is needed for the crack to pull apart the fibers. An illustration of this mechanism is given in Figure 2.10c.

2.4 Carbon Fibers

Carbon fibers are fibrous materials which are almost completely made up of carbon with a graphite-like structure. They are one of the most widely used fibers in composite materials due to their desirable mechanical, electric and thermal properties. They can be formed into a number of different forms, such as long fibers, whiskers and fabric, to name a few. Carbon fibers are somewhat more expensive than glass or plastic fibers, but considerably cheaper than more novel types of fibers, such as those made from SiC and other ceramics. The main area of usage of carbon fibers are the aerospace and civil engineering sectors, but their properties are also valued as a composite material. The structure, properties and production of carbon fibers will be presented in this section.

2.4.1 Structure of carbon fibers

The most stable form of carbon is graphite. It has a two-dimensional hexagonal structure with strong in-plane bonds. In the third dimension it has a layered structure held together by weak van der Waals forces. Graphite is, thus, crystalline and has a long range order in all directions, with most of the interesting properties appearing in-plane of the two-dimensional sheets. The structure of carbon fibers is more complex, depending on their precursors, the two most widely used are polyacrylnitrile (PAN) and mesophase pitch.

PAN-based fibers have a fibrillar structure, due to the structure of the polymer precursor. Even though the fibers have two-dimensional crystalline order in the form of graphite sheets, they lack long range three-dimensional order graphite has. In stead Johnson [39] found that the graphite sheets in the fibers are considerably folded, resulting in a turbostratic microstructure. The graphite layers have more order and preferred orientation near the surface of the fiber and become disordered towards the center, often with angles of 180 °. An image of the microstructure of PAN-based fibers proposed by Johnson is shown on Figure 2.11. The microstructure was further studied by Guigon *et al.* [40], where it was confirmed that the sheets prefer to fold around the fiber axis, though not always aligned. This resulted in the generation of needle-like pores parallel to the axis. This, combined with the low degree of graphitization, larger inter-layer spacing than graphite and smaller crystallite size, allows for more movement and reordering of the layers, which generally gives PAN-based fibers a higher tensile strength [41].

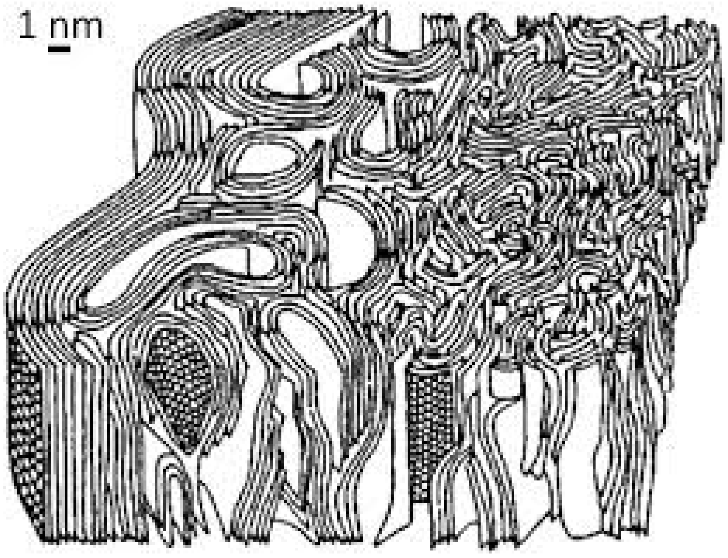

Figure 2.11: The microstructure of PAN-based carbon fibers proposed by Johnson [39]. The fiber axis is from top to bottom.

Fibers based on mesophase pitch are much more ordered and have a higher order of graphitization than PAN-based fibers. As the liquid precursor is spun into fibers, the molecules reorder themselves in a transverse microstructure and in an orientation parallel to the fiber axis. This happens due to the capillary forces present during the formation in the fibers [41]. During graphitization the structures are frozen in place and do not change. Depending on the method of spinning, the texture can have multiple forms, as studied by Mochida *et al.* [42]. The graphite sheets can either radially form from the center of the fiber, form a flat-layer structure with a preferred orientation, have a co-centric onion skin structure or be randomly oriented in the fiber. A schematic of these textures is shown on Figure 2.12.

The higher three-dimensional order of the pitch-based fibers leads to a more rigid structure that is more prone to lattice flaws. This results in a lower tensile strength than PAN-based fibers, though it also makes them stiffer with a higher elastic modulus.

2.4.2 Properties of carbon fibers

As mentioned before, carbon fibers have interesting properties that make them useful in a wide variety of applications. Being mostly made out of carbon, they have a low density.

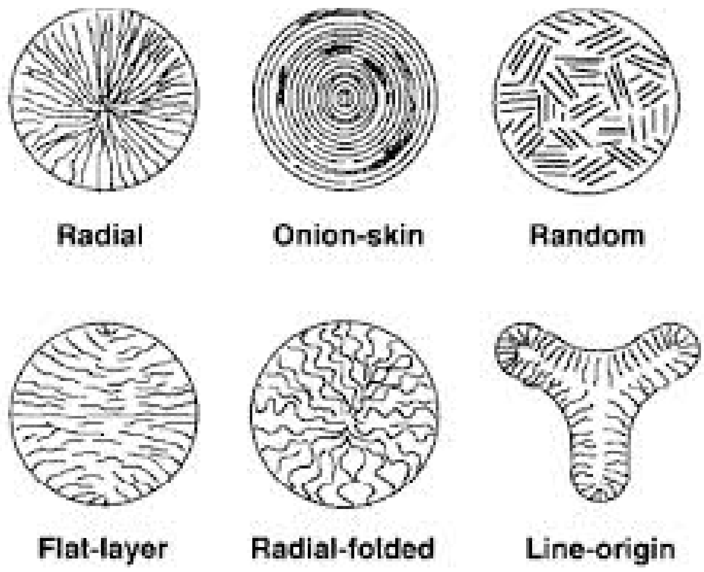

Figure 2.12: The different types of transverse textures found in pitch-based carbon fibers [41]. The fiber axis is out of the page.

Strong covalent bonds between the carbon atoms in plane of the graphite layers make the fibers stiff with a high elastic modulus. The lack of long range order give them high tensile and compressive strength, due to the freedom of movement of the layers and their ability to reorder. With a structure of graphite comes high electrical and thermal conductivity. PAN-based fibers generally have a lower density and higher tensile strength than pitch-based fibers, while pitch-based fibers have higher elastic modulus and better thermal and electrical conductivity than their PAN-based counterpart. Pitch-based fibers are also generally more expensive to produce. The properties can vary a lot depending on the processing of the fibers, but the general range of these properties for both PAN- and pitch-based fibers are given in Table 2.4.

Table 2.4: The principal properties and their ranges of PAN- and pitch-based carbon fibers [43].

Property	PAN-based fibers	Pitch-based fibers
Density $[\mathrm{g/cm^3}]$	1.79-1.91	1.90-2.20
Tensile strength $[\mathrm{GPa}]$	3.8-6.37	1.38-3.10
Compressive strength (along fiber axis) $[\mathrm{GPa}]$	0.9-2.88	0.2-1.15
Young's modulus $[\mathrm{GPa}]$	228-590	159-965
Thermal conductivity $[\mathrm{W/mK}]$	0.08-0.14	0.22-11
Electrical conductivity $[\mathrm{S/cm}]$	$5.56{\cdot}10^4$-$1.25{\cdot}10^5$	$7.69{\cdot}10^4$-$9.09{\cdot}10^5$

2.4.3 Production of carbon fibers

Most of the carbon fibers today are made from either a PAN or a pitch precursors. As discussed before, fibers made from either precursor have very different structures and properties. Also the production of the fibers differ and will be discussed here.

PAN is a polymer, with a linear structure and nitrile groups, which make it highly polar. Pure PAN is rarely used for fiber production, due to its low glass transition temperature, and thus the precursor usually contains up to 15% of other monomers to increase that temperature [44]. Wet spinning is usually used to produce fibers from PAN, which is dissolved into a polar solvent. The solution is extruded in a coagulation bath and then the fibers are spun at around 100 °C through capillaries. As the precursor is a polymer, the fibers tend to get a fibril structure. The fibers are then stabilized at temperatures of 200 °C to 300 °C in oxidizing atmosphere under tension. This step is needed to make sure that the fibrous structure remains even after the carbonization step. The linear PAN is cyclized into closed rings and a ladder polymer is formed. Hydrogen is evolved and oxygen pickup occurs, while the fibers are densified. Thereafter the fibers are carbonized in inert nitrogen atmosphere at 1000 °C to 1500 °C [41]. Volatile gasses such as ammonia, methane, hydrogen, carbon monoxide and carbon dioxide evolve during the pyrolysis, taking most of the non-carbon atoms with them. The mass of the fiber is reduced by about 60 wt% and a final diameter is achieved, around 7 μm. The temperature can be varied for different strengths and stiffnesses. A schematic illustration of the wet-spinning process is shown in Figure 2.13.

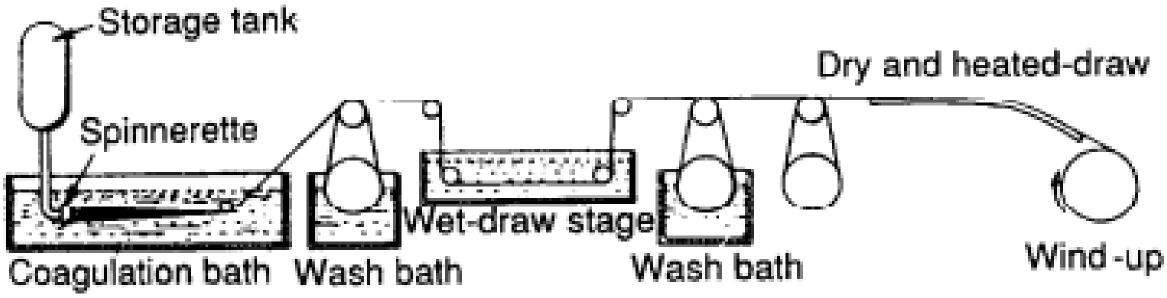

Figure 2.13: A schematic showing the wet-spinning process of producing PAN-based carbon fibers [41].

The precursor for pitch-based fibers is mesophase pitch. This is by either coal or petroleum tar each having their advantages [41]. The mesophase pitch is a thermotropic crystal and consists of large aromatic hydrocarbons. Isotropic pitch is sometimes used to lower the softening point of the mesophase pitch [44], though pure mesophase pitch precursor is desired for better properties of the fiber. While PAN-based fibers are usually wet-spun, pitch-based fibers are melt-spun. This is possible due to the pitch precursor softening and flowing far below the temperature at which they degrade and decompose. The advantage of melt-spinning is the absence of a solvent, which could cause stability problems for the fibers. The pitch is melted and the pressure of the melt is increased through an extruder. A metering pump is used to stabilize the melt and push it through the spineret. As the melt exits the spineret, it is quenched and fibers are drawn by a windup device. The fibers are then stabilized between 200 °C and 300 °C to convert it from a thermoplastic to a thermoset material and to avoid relaxation during the final heat treatment. The carbonization is then carried out at temperatures between 1000 °C and 1500 °C. As with carbonization of PAN-based fibers, non-carbon atoms are removed by volatile gasses, but due to the pitch precursor being 90% carbon, the weight loss is only about 20-30 wt%. This means that the final fiber diameter is thicker than for the PAN-based fibers and they need to be further spun to achieve smaller diameters. A schematic illustration of the melt-spinning process is shown in Figure 2.14.

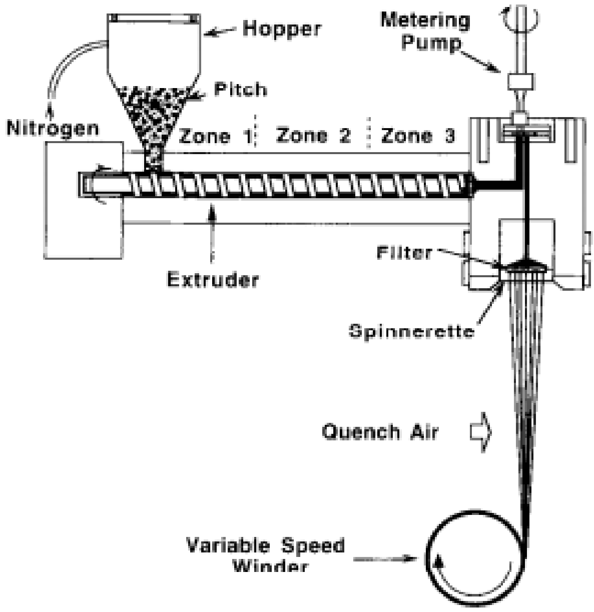

Figure 2.14: A schematic showing the melt-spinning process of producing pitch-based carbon fibers [45].

2.5 Review of carbon fiber reinforced SiC

Since the introduction of reliable fabrication techniques of carbon fibers, composites based on these fibers have been a hot topic in research. This includes composites based on SiC matrix, which have been studied by various fabrication methods over the last few decades. This section will give a brief overview of some of these studies, their fabrication method and the results they achieved.

Nakano *et al.* [46] fabricated unidirectionally oriented carbon fiber reinforced SiC composites by slurry impregnation. The SiC particles were β-SiC with 0.3 μm particle size and the fibers were pitch-based carbon fibers. The fiber content was found to be around 33 vol%. The powder was hot-pressed at 1850 °C in argon atmosphere. Flexural strength was tested by three point-bending and fracture toughness was tested by single edge notched beam under four-point bending. The open porosity of the sample was around 5 %. The flexural strength and fracture toughness measured at room temperature were found to be 420 MPa and 13 $\mathrm{MPa}\sqrt{\mathrm{m}}$ respectively.

The same author [47] also fabricated three dimensional carbon fiber reinforced SiC composites by repeated liquid infiltration of the slurry and fibers. The precursors they used were fine β-SiC with a grain size of 0.4 μm and pitch based fibers with a diameter of 10 μm with a fiber volume content of 36 vol%. After a pyrolisation step, the powder was hot-pressed in argon atmosphere at 1850 °C with a pressure of 7.4 MPa. Felxural strength and fracture toughness were measured as before. The open porosity of the hot pressed sample was found to be around 3 % with a flexural strength of 106 MPa and a fracture toughness of 3.1 $\mathrm{MPa}\sqrt{\mathrm{m}}$ at room temperature. They also reported significant deterioration of the fibers in the matrix and little deflection of the crack by the fibers. The difference between the measured strength and fracture toughness between three-dimensional and unidirectional fibers were attributed to the amount of fibers in the stress direction.

More recent examples of carbon fiber reinforced SiC have been fabricated with the use of spark plasma sintering. Ding *et al.* [48] mixed a slurry of nano-β-SiC with a particle size of 60 nm and PAN-based carbon fibers with a diameter of 6 μm and length of 2-3 mm. The fiber content of the slurry was 20 vol%. The slurry was dried and sintered at 1650 ℃ with an applied pressure of 25 MPa and a holding time of 3 minutes. Subsequent strength testing was carried out by three-point bending. They reported a strength of 170 MPa for the samples with fibers and an open porosity of about 3 %. The samples without fibers showed a higher strength of 425 MPa and a lower open porosity of 0.67 %. They attributed the lower strength to cracks formed during sintering. However, they also reported noncatastrophic fracture behaviour in their composites. SEM micrographs of the fracture surfaces of the samples made by the author can be seen in Figure 2.15.

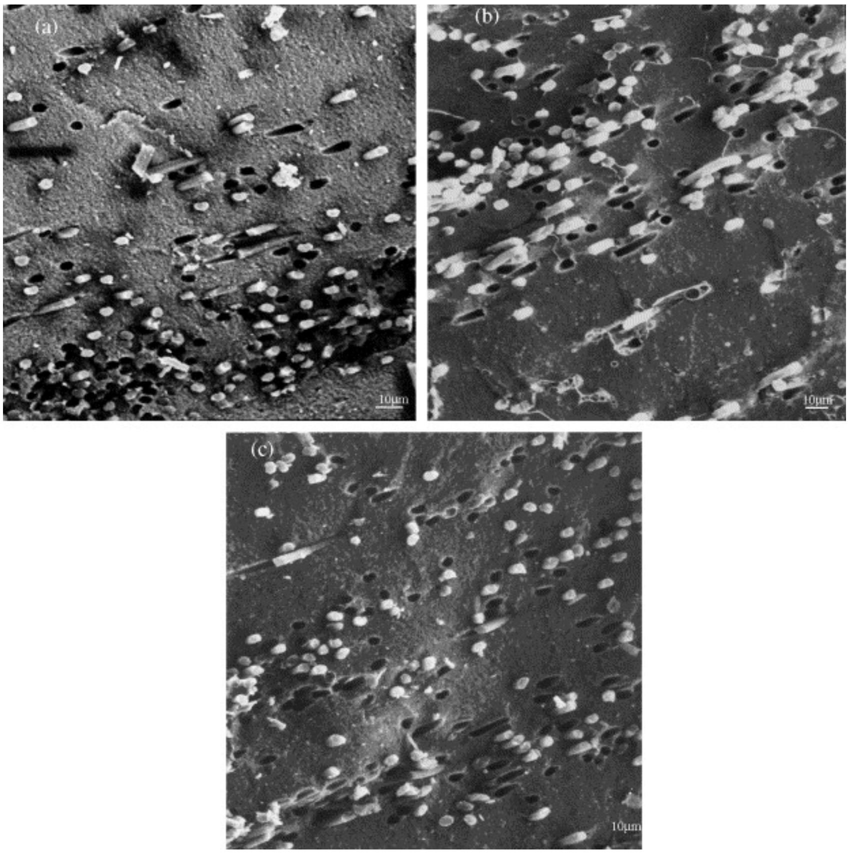

Figure 2.15: SEM micrographs of the fracture surfaces of the composites made by Ding *et al.* showing fiber/matrix interaction [48].

Ghasali *et al.* [49] also fabricated composites utilizing spark plasma sintering. They used SiC nanopowders with an average particle size of 50 nm and carbon fibers with a diameter of 5 μm and length of 30 μm as precursors. The volume fraction of fibers was 1 vol%. The powder was sintered at 1900 and 2200 ℃ with an applied pressure of 50 MPa and at 8 and 6 minutes of holding time under vacuum conditions. The higher temperature was because of no addition of sintering aids. The porosity of the samples were 11 and 3 vol%, respectively. Strength was measured by three-point bending and fracture toughness by Vickers microindentation. For strength these values were 291 and 427 MPa for 1900 and 2200 °C samples and the fracture toughness values were 2.8 and 4.2 $\mathrm{MPa}\sqrt{\mathrm{m}}$, respectively. They also reported a good bonding between fibers and matrix with a thin SiC layer in the interface as a result of the reaction between carbon in the fibers and silica on top of SiC particles. SEM micrographs of the polished samples made by the author can be seen in Figure 2.16.

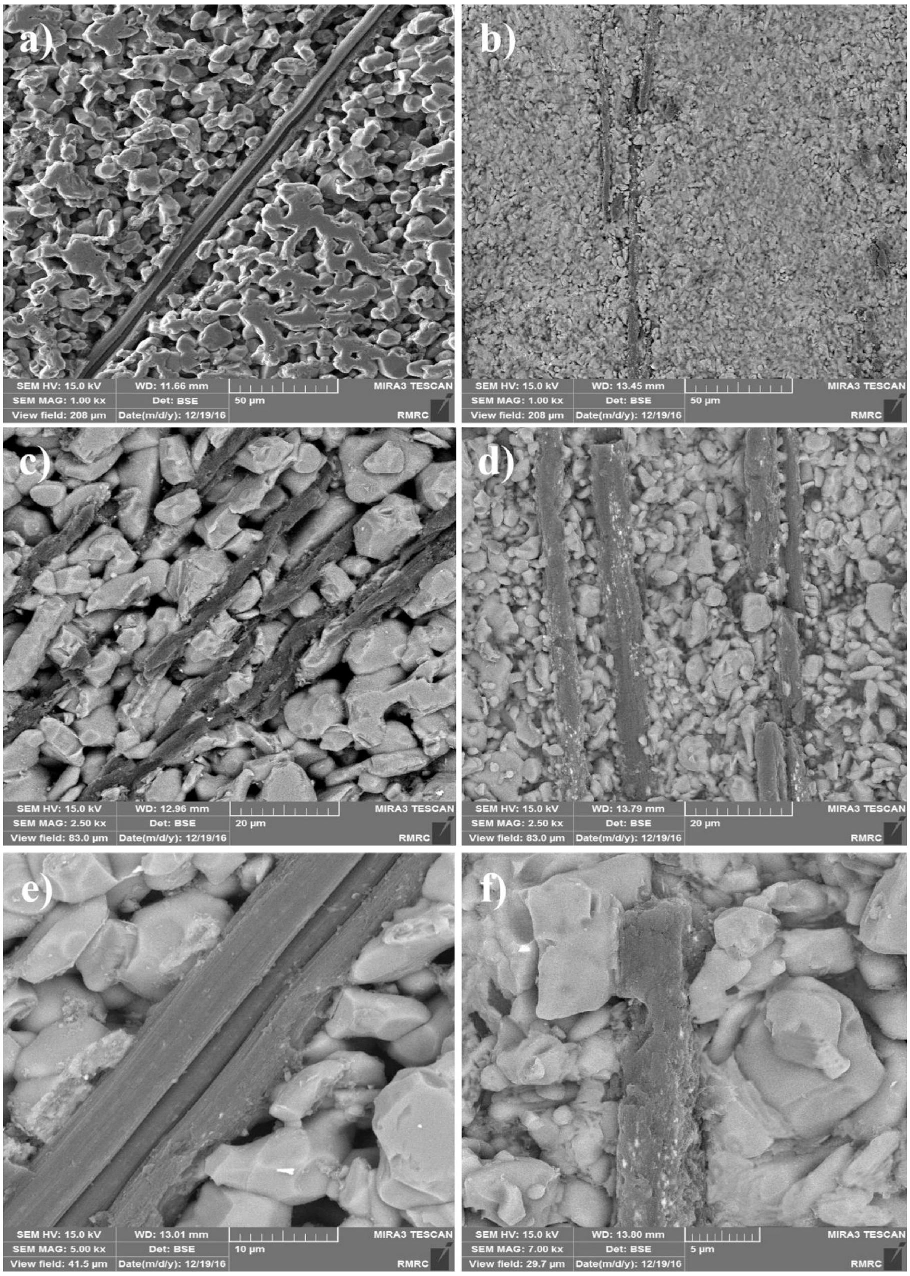

Figure 2.16: SEM micrographs of the composites made by Ghasali *et al.* showing fiber/matrix bonding [49].

3 Experimental

3.1 Powders and apparatus

A simple flowchart of the process of the preparation of the powders can be seen on Figure 3.1.

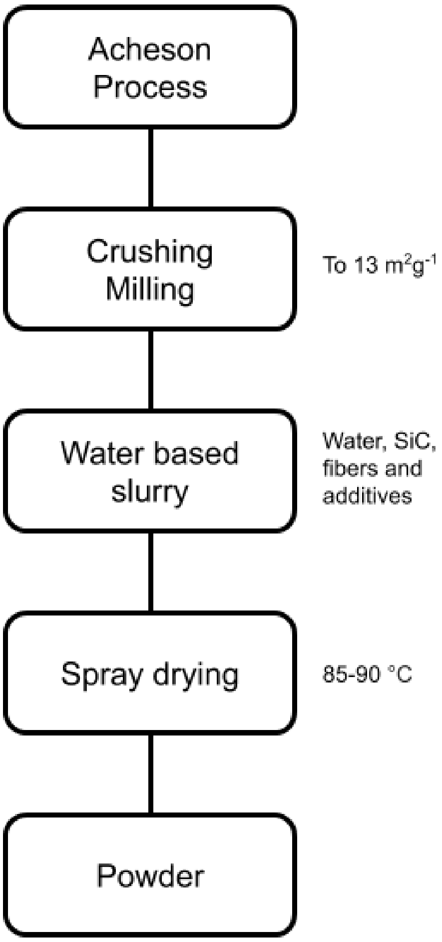

Figure 3.1: Flowchart of the production of the precursor powders.

Silicon carbide was produced by Saint-Gobain Ceramic Materials AS Lillesand via the Acheson process. The crude material was then crushed and milled to a desired particle size. Three water based slurries were made with SiC and 0, 10 and 15 vol% carbon fibers along with boron carbide and carbon black as sintering additives. The SiC powder used as basis was Sintex 13C which is an α-SiC powder with a specific surface area of 13 m^2g^{-1}. Binders and dispersants were added for slurry and granulate stabilization. Extra carbon was added to the powders with fibers to protect the fibers during sintering. The slurries were mixed in a planetary ball mill with rubber balls for around 24 hours. The pH and water content were monitored until a stable slurry was achieved. Then the slurries were spray dried. The slurries were pumped through a nozzle and atomized in the drying chamber to form round, soft granulates. These were then collected in a cyclone. The compositions of the powders are summarized in Table 3.1.

Table 3.1: The vol% and wt% of carbon fibers and wt% of boron carbide and carbon black of the three precursor powders.

Powder	vol% fibers	wt% fibers	wt% boron carbide	wt% carbon black
1	0	0	1.2	2-3
2	10	6.3	1.2	3.4
3	15	10.0	1.2	3.4

The fibers used were PX 35 PAN-based milled carbon fibers made by ZOLTEK. The properties of the fibers are summarized in Table 3.2.

Table 3.2: Density, tensile strength and modulus, carbon content, diameter and length of the ZOLTEK PX 35 carbon fibers used [50].

Property	PX 35
Density $[\mathrm{g/cm^3}]$	1.81
Tensile strength [GPa]	4.137
Youngs modulus [GPa]	242
Carbon content [%]	95
Fiber diameter [μm]	7.2
Average fiber length [μm]	100-150

SEM images of the powders with 0, 10 and 15 vol% carbon fiber can be seen in Figure 3.2a, Figure 3.2b and Figure 3.2c, respectively. Figure 3.2d shows a SEM image of the fibers.

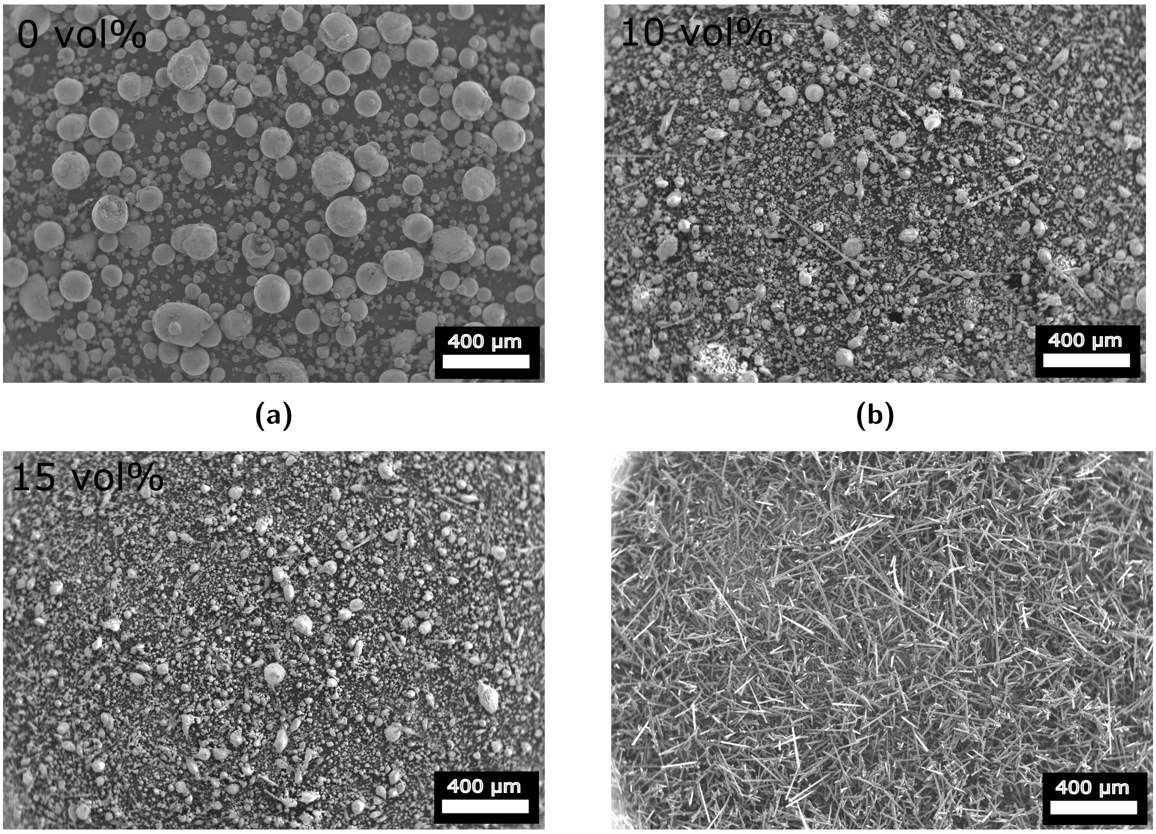

(a) (b) (c) (d)

Figure 3.2: SEM images of the three precursor powders with a) 0 vol%, b) 10 vol% and c) 15 vol% carbon fibers. The round particles are SiC granulates while the long particles are the fibers. d) SEM image of the fibers.

Table 3.3 shows the apparatus used for sample preparation and characterization along with their model and application.

Table 3.3: The apparatus used for preparation and characterization of the samples with their model and application.

Apparatus	Model	Application
Spark plasma sintering	SPS 825 Dr. Sinter	Sintering with external pressure
Polishing	Struers Tegrapol-31	Surface preparation
EBSD	Hitachi SU-6600	Microstructure analysis
XRD	D8 Focus	Phase analysis
SEM	Hitachi S-3400N	Surface analysis
SEM	Zeiss Supra 55PV	Fracture analysis
Vickers indentation	Zwick/Roell ZHV30	Hardness/fracture toughness measurement

3.2 Procedures

3.2.1 Spark plasma sintering

The sintering was done with the SPS 825 Dr.Sinter unit, shown in Figure 3.3a. A graphite die with two punches and an inner diameter of 28 mm was used. Graphite paper was put between the punches and the die and also between the powder and the punches. This is to reduce the sticking of the powder to the die and punches during sintering and for easier ejection after sintering as well as to protect the sample and the die/punches. The powder of about 7 g was put into the die atop one of the punches and the die was shaken gently to get an even distribution. The top punch was then inserted. An initial pressure of 2 MPa was applied for stability. The die was covered with thick graphite wool for thermal insulation and was placed symmetrically between the electrodes of the sintering unit. Graphite disks were used to get the correct height. Additional graphite wool was used for even more thermal insulation due to the high temperature. The wool was tied in place with graphite thread. The temperature was measured with a pyrometer, which was aligned with a hole in the die for accurate temperature measurement starting from 400 °C. A starting pressure of 3 MPa vas applied and the chamber was evacuated to about 20-30 Pa. Figure 3.3b shows the sample between the electrodes in the sintering chamber and Figure 3.3c shows a prepared sample with a hole for the pyrometer. After the sintering the sample was cooled to about 250 °C and taken out. A uniaxial press was used to take out the sample from the die and excess carbon paper was removed with a sandblower using nut shells. The sintering process was monitored by sensors measuring z-displacement and chamber gas pressure.

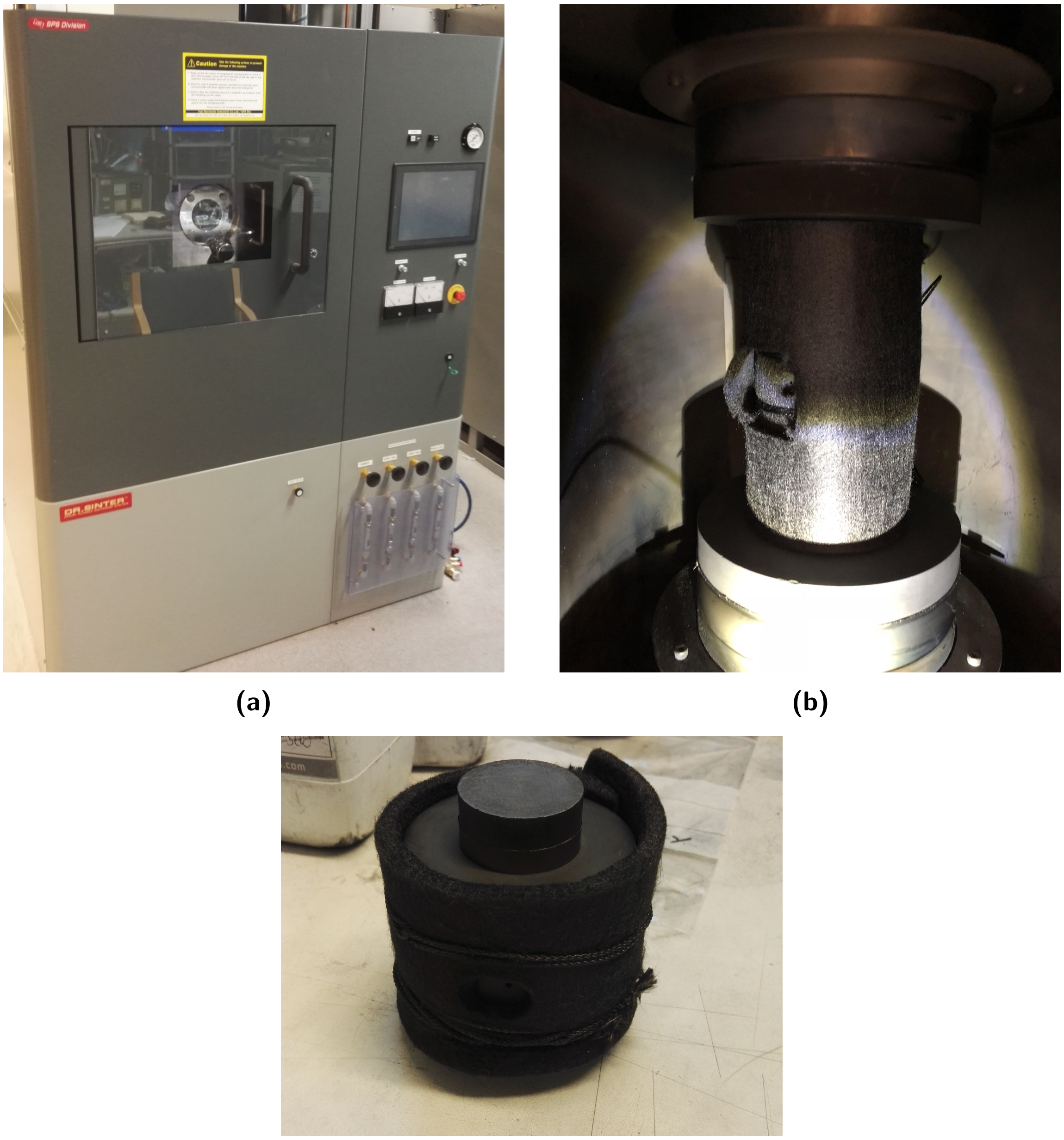

(a)

(b)

(c)

Figure 3.3: a)The SPS 825 Dr.Sinter sintering unit. b) The sample between the electrodes, ready to sinter, with extra graphite wool. c) A fully prepared sample in the die with punches inserted and graphite wool cover.

A sintering study was conducted to optimize sintering program. This was done to introduce fibers into the matrix while also minimizing the grain growth. The parameters that were changed are given in Table 3.4, with the first four samples belonging to the optimization step. After a suitable program was found, three more samples were made with 0, 10 and 15 vol carbon fiber content, the next three samples in Table 3.4. Finally one sample without fibers was made for the strength test along with three samples with 10 vol% carbon fiber content and four samples with 15 vol% carbon fiber content.

Table 3.4: The samples that were sintered along with the sintering parameters: top temperature, heating rate, holding time and paper thickness. The applied top pressure was the same for all samples at 20 MPa.

Sample	Temperature [°C]	Heating rate [°C/min]	Holding time [min]	Paper thickness [mm]
2050-15	2050	75	15	0.1
2050-5	2050	75	5	0.1
1850-thin	1850	200	3	0.1
1850-thick	1850	200	3	0.25
0% main	1850	200	5	0.25
10% main	1850	200	5	0.25
15% main	1850	200	5	0.25
0% str-1	1850	200	5	0.25
10% str-1	1850	200	5	0.25
10% str-2	1850	200	5	0.25
10% str-3	1850	200	5	0.25
15% str-1	1850	200	5	0.25
15% str-2	1850	200	5	0.25
15% str-3	1850	200	5	0.25
15% str-4	1850	200	5	0.25

3.2.2 Polishing

The polishing was done with Struers Tegrapol-31. The samples were cast in epoxy and hardened overnight. The polishing was done with diamond disks and paste and the steps are given in Table 3.5. A counter rotation was applied to the polishing disk and sample holder. Between the final three steps, ultrasonic bath in ethanol was used to remove any particles from the surface. After the samples were polished, the samples were left in a beaker with chloroform for over two days to remove the epoxy.

Table 3.5: The polishing steps done on each sample with the disk and lubricant used, applied force, time and speed of polishing. The samples were all 28 mm in diameter and cast in epoxy.

Step	Polishing disk	Grit size [mesh]	Lubricant	Force [N]	Time [min]	Speed [rpm]
1	MD-Piano	80	Water	45	60	300
2	MD-Piano	200	Water	35	15	300
3	MD-Piano	1200	Water	20	15	300
4	MD-Allegro	-	DiaPro All/Lar 9 μm	15	15	150
5	MD-Dac	-	DiaPro Dac 3 μm	10	10	150
6	MD-Nap	-	DiaPro Nap 1 μm	10	5	150

3.2.3 Density measurement

The density was measured with standard Archimedes method in a vacuumed container [51]. The dry weight, m_1, of the pellets were measured. The samples were then put in an exicator and the atmosphere was vacuumed. Pure isopropanol was introduced and the chamber was vacuumed again to ensure all pores were filled with the liquid. The temperature of isopropanol was measured. The immersed weight, m_2, and the wet weight, m_3 were measured. The density, apparent and total porosity were calculated using the equations given in Appendix A.

3.2.4 Phase analysis

The phase composition was analyzed using X-ray diffraction with the D8 Focus diffractometer. The diffractometer was working in Bragg-Brentano geometry (2Θ-Θ) and the 2Θ angle ranged from 10°to 80°. The scanning time was 60 minutes. The X-ray source was a copper filament with a K_α wavelength of 1.54060 nm. The diffractograms were analysed with the EVA program for peaks found in PDF-4 database to identify the peaks. The TOPAS software was used for quantitative phase analysis with the utilization of Rietveld refinement.

3.2.5 Microstructural analysis

The microstructure was analysed with a Hitachi SU-6600 field emission SEM with and electron backscatter diffraction (EBSD) detector attached to it. Prior to analysis the sample was ion milled for about 20 minutes in argon gas to ensure good surface quality. In the SEM, the sample was tilted to 70° and the image was focused at 50 and 200 magnification. The applied voltage was 20 kV with a working distance around 25 mm. The NORDIF 3 program was used to scan the sample for EBSD patterns. The background was substracted and calibration patterns were acquired. After-scan analysis of the patterns was done in the EDAX-TSL OIM 7 Data Collection program and the inverse pole figures (IPF) were obtained from the EDAX-TSL OIM 7 Data Analysis program.

3.2.6 Mechanical properties

Hardness

Vickers micro-indentation was used for hardness measurement. The hardness measurement unit was Zwick/Roell ZHV30, which was connected to a light microscope. The load was set to 1 kg with a dwell time of 10 s. 10 indents were made on each sample. The Vickers hardness, HV, was calculated from the following formula [52],

$$HV = \frac{1.854 \cdot F}{d^2} \tag{3.1}$$

where F is the load in kg and d is the average of the two diagonals of the indent in mm.

Fracture toughness

The fracture toughness was measured on the same indents. An average length of four cracks was used to calculate the fracture toughness, K_{IC}, with the following formula [52],

$$K_{IC} = 0.016\Big(\frac{E}{HV}\Big)^{\frac{1}{2}} \cdot \Big(\frac{P}{c^{\frac{3}{2}}}\Big) \tag{3.2}$$

where E is the Young's modulus in GPa, HV is the hardness in GPa, P is the force in N and c is the crack length in $\mu\mathrm{m}$.

Flexural strength

The strength of the sintered samples was measured by Saint-Gobain Ceramic Materials AS with the ring-on-ring method. A schematic of the method is shown in Figure 3.4.

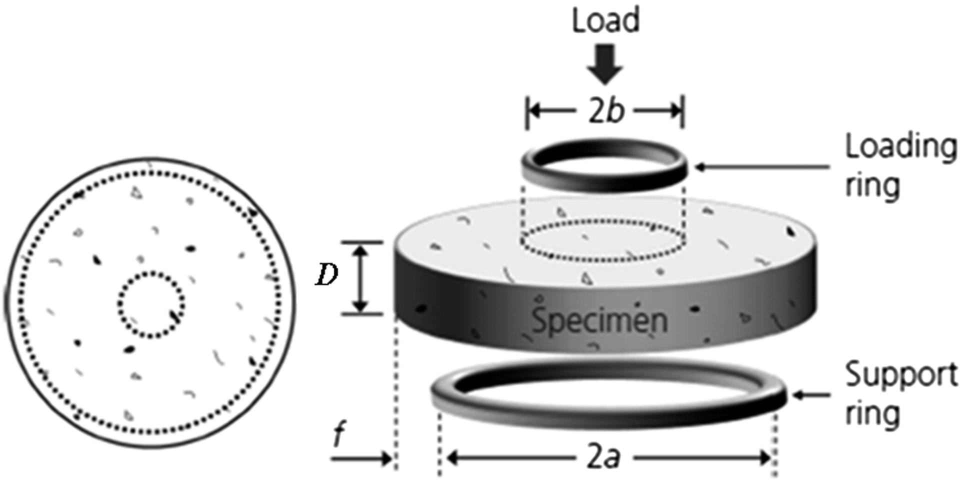

Figure 3.4: A schematic of the ring-on-ring flexural strength testing method [53].

The ring-on-ring method is a biaxial flexural strength test method. A cylindrical sample is put between a small ring and a larger ring and a load is applied from above. The stress is distributed equally in all directions in-plane. This makes it a good method to measure the flexural strength of brittle materials.

3.2.7 Fracture analysis

The fracture surface was analyzed with Hitachi S-3400N SEM and the Zeiss Supra 55 PV field emission SEM. The samples were broken into pieces with a hammer and mounted on sample holders with double sided tape. Coating was not necessary, because SiC is sufficiently conducting. The voltage, probe current and working distance were chosen after need for sharpest images, with a typical voltage of 5-10 kV and a working distance of 5-7 mm. Additionally, the fracture surface of the samples broken during the strength test were analyzed.

4 Results

The results attained from the experimental work will be presented in this section. The results will be divided into two parts. First a preliminary sintering study will be presented, with a focus on how different sintering parameters affect the microstructure and density of the samples and more importantly how the stability of the fibers is affected by the parameters. The second part will present the characterisation of the main samples with fibers and will focus on phase compositions, densities, microstructures and fiber/matrix interactions of the samples. Finally the mechanical properties of the samples will be presented.

4.1 Optimization of Sintering Parameters

The aim of this part is to optimize the sintering program to achieve a better microstructure and more importantly, to get the fibers into the matrix. This is based on the results of Skarpeid [54] and the authors own specialization project [55]. The sintering data collected *in situ* by the SPS will be presented, as well as the microstructure and densities of the sintered samples. The effect of the sintering on the fibers will also be presented.

4.1.1 Sintering Curves

The heating rate for the initial sintering program was 75 °C/min, the top temperature was 2050 °C, the applied top pressure was 20 MPa and the holding time was 15 minutes at top temperature. A sharp shrinkage of the sample was observed after the removal of silica, at around 1500 °C. When the sample reached the top temperature, no more shrinkage was observed. Instead the sample seemed to be expanding, which indicates that the sintering was done by that point.

The holding time was then reduced to 5 minutes, while the rest of the parameters were kept unchanged. The sample showed similar shrinkage and expansion trends. A sintering run was done with the same parameters, but without any powder, to gather the background z-displacement data of the die and papers. The background data showed that most of the expansion at high temperatures is caused by the die and papers as carbon has much higher thermal expansion than SiC. This gave an indication that the densification was done before reaching the top temperature as the shrinkage of the sample had stopped. The conclusion was that the sintering temperature was too high. The sintering curves for these initial tests can be seen in Appendix B. Also all of the sintering curves shown from now on have had their respective backgrounds subtracted.

For the next sample the temperature was reduced to 1850 °C, the heating rate was increased to 200 °C/min and the holding time was reduced to 3 minutes. The applied top pressure remained the same. The sintering data can be seen in Figure 4.1a. It can be seen that there are two gas evolutions, one that starts at around 400 °C and another that starts at around 1200 °C. The first one corresponds to volatile organic species and the second one is CO gas as a result of removing silica form the surface of the particles by the same reaction that is present in formation of SiC, Equation 2.1. The z-displacement shows shrinkage as a negative slope and expansion as a positive slope. With the background subtracted, the curve looks smoother and can be compared to a dilatometry curve. It can be seen that the densification starts around the same time as the second gas evolution, which was the same as for the initial tests. When the pressure is increased the densification becomes more rapid. At top temperature there is again some initial expansion but the curve stabilizes after around half a minute.

For the next sample the sintering program was unaltered. The thickness of the carbon paper that is put between the sample and the die was changed from 0.1 mm to 0.25 mm. The resulting sintering data can be seen in Figure 4.1b. It can be seen that there is no longer any expansion during sintering. The second gas evolution also starts much later, at around 1500 °C with a peak just before top temperature. A side by side comparison of the gas evolutions and shrinkage during sintering with thick and thin paper can be seen in Figures 4.2a and 4.2b. There is a clear delay of both gas peaks with the use of thicker paper as well as a much faster evolution at the second peak. Densification also shows a similar delay.

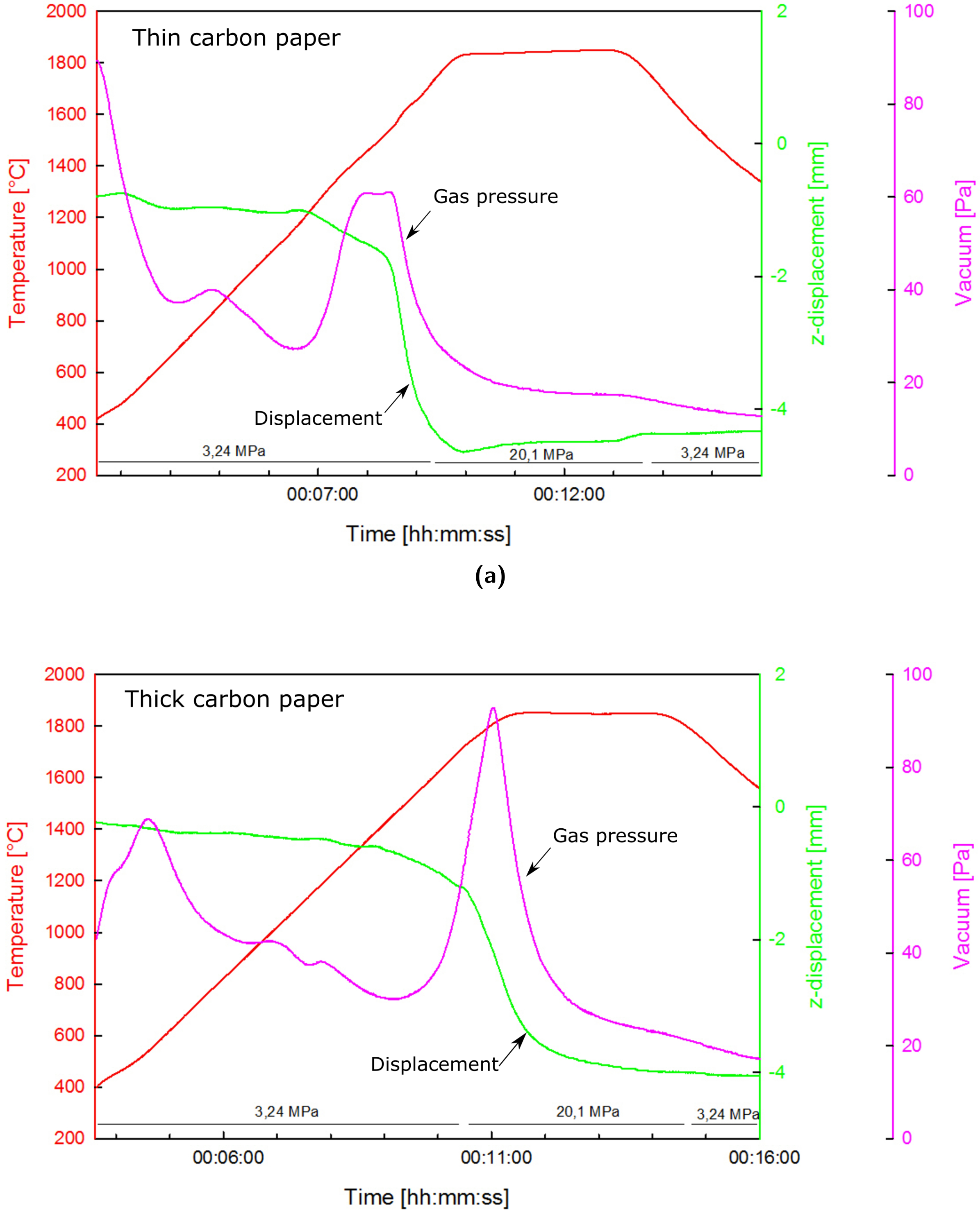

(b)

Figure 4.1: The sintering data gathered from the SPS for a) sintering at 1850 °C and with a thin carbon paper and b) sintering at 1850 °C and with a thick carbon paper. The red curve is the temperature, the green curve is the displacement in the z direction, the pink curve is the chamber gas pressure and the black lines show the pressure change.

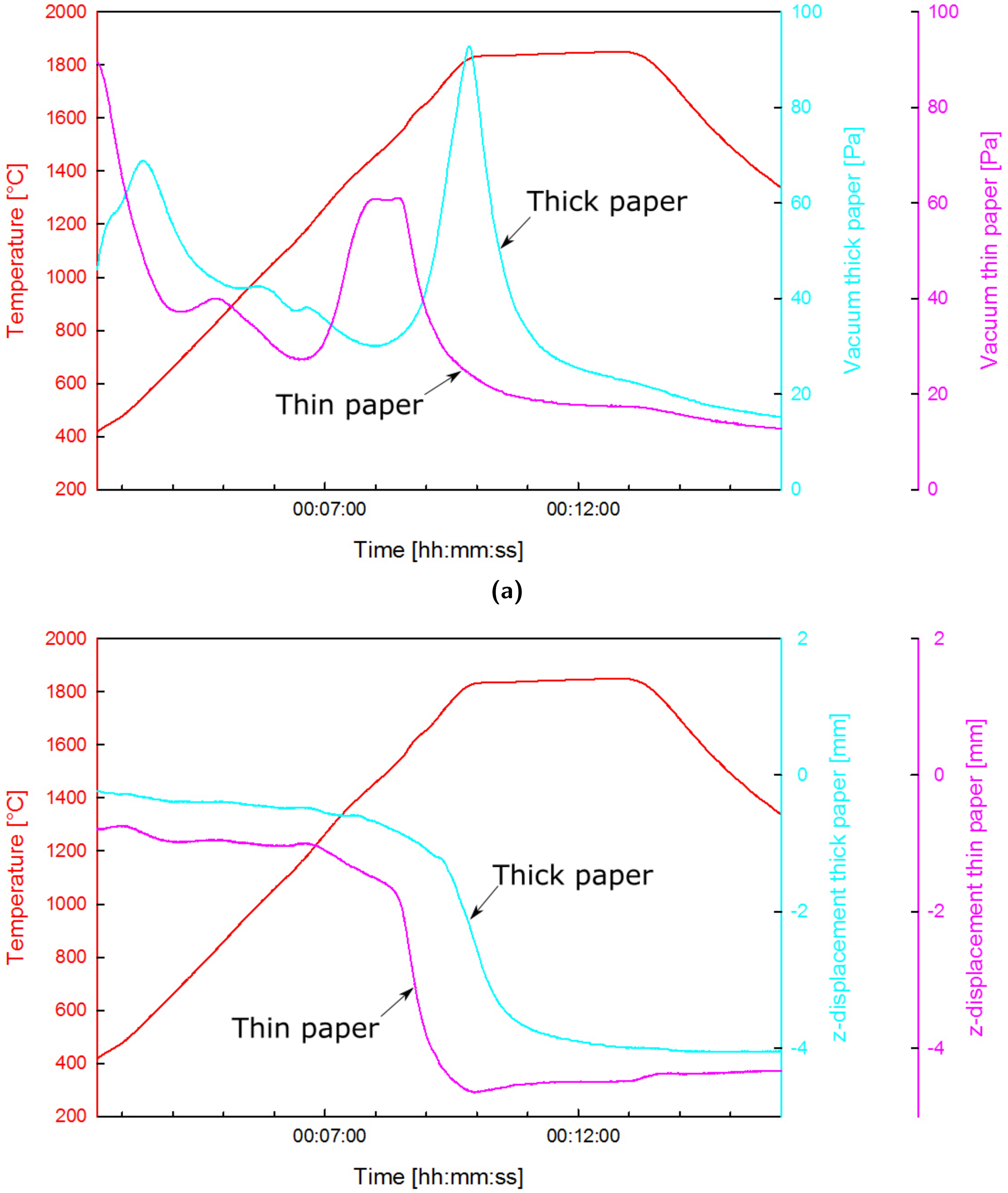

(a)

(b)

Figure 4.2: A side by side comparison of a) the chamber gas pressure and b) the shrinkage of the samples sintered with thick and thin paper.

4.1.2 Densities

The relative densities and porosities of the samples measured with the Archimedes method can be seen in Figure 4.3 and Figure 4.4, respectively. The theoretical densities of the samples was set to that of α-SiC, 3.21 g/cm^3, with none of the additives taken into consideration.

It can be seen in Figure 4.3 that the relative densities for the first three samples remain relatively similar, at around 98 %. Temperature and holding time do not seem to influence the densities. There is, however, a sharp drop in relative density when thick carbon paper is used, to around 90 %. The porosities show a similar trend, as seen in Figure 4.4. The open porosities remain around 1 % for the first three samples, which should ideally not exist above 92 % relative density and are therefore side effect of the measurement method. Analogous with the drop in relative density, the sample with thick carbon paper shows a sharp increase in open porosity, to about 8 %. The closed porosities remain relatively similar for all samples, at around 1.5-2 %.

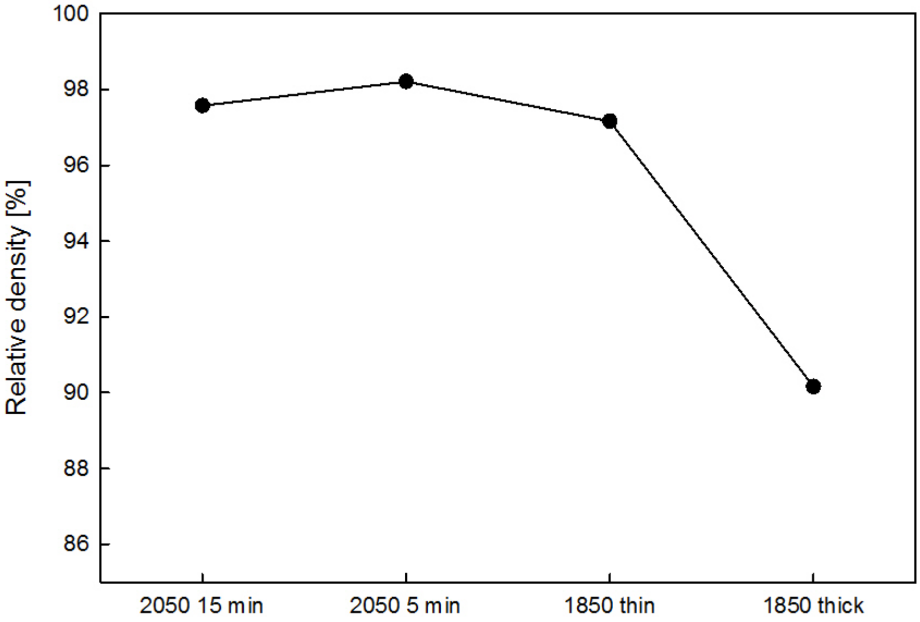

Figure 4.3: The relative densities of the samples sintered at 2050 °C with 15 and 5 min holding time and at 1850 °C with a thin and a thick carbon paper. The lines are a guide to the eye.

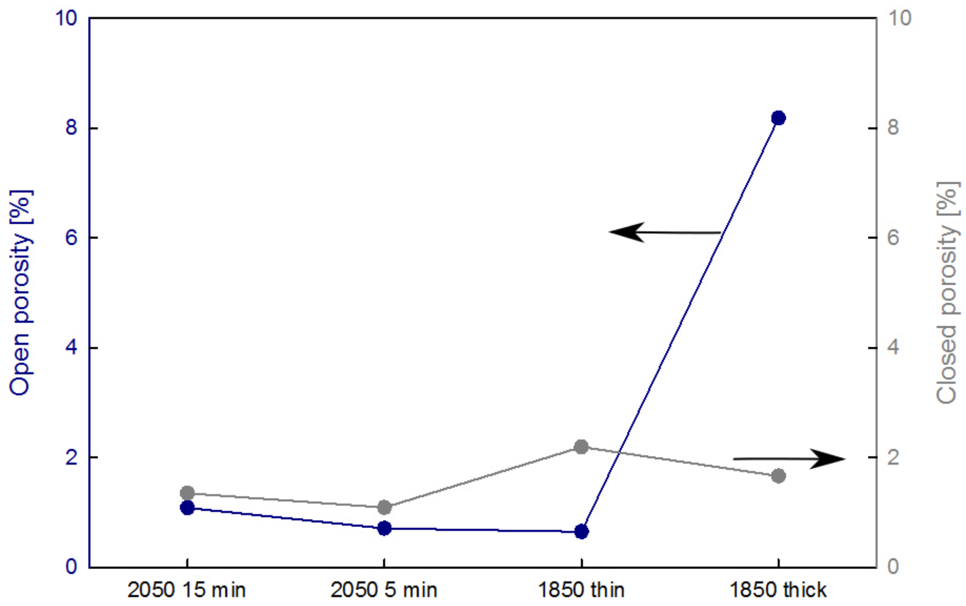

Figure 4.4: The porosities of the samples sintered at 2050 °C with 15 and 5 min holding time and at 1850 °C with a thin and a thick carbon paper. The blue points are the open porosities while the grey points are the closed porosities. The lines are a guide to the eye.

4.1.3 Microstructure

The microstructures of the samples measured by EBSD can be seen in Figures 4.5a-4.5d. The different colors indicate different crystallographic orientations of the grains. From Figure 4.5a it can be seen that with a holding time of 15 minutes at 2050 °C the grains are large and elongated, with a thickness of about 100 μm and a length up to 500 μm. Figure 4.5b shows the microstructure for the sample sintered at 2050 °C with a holding time of 5 minutes. The image quality is lower most likely due to poorer surface treatment, but the largest grains are still visible with similar dimensions. When the temperature is reduced to 1850 °C the grains are still long, but the thickness has decreased considerably, as seen in Figure 4.5c. There are also more of the smaller grains present compared to the samples sintered at 2050 °C. Figure 4.5d shows the microstructure when the carbon paper was changed. Even with a larger magnification, as indicated by the change in the scale bar, there seem to be no grains present. The grains are most likely smaller than the resolution limit at that magnification and very little grain growth has occurred. SEM images corresponding to the IPFs are shown in

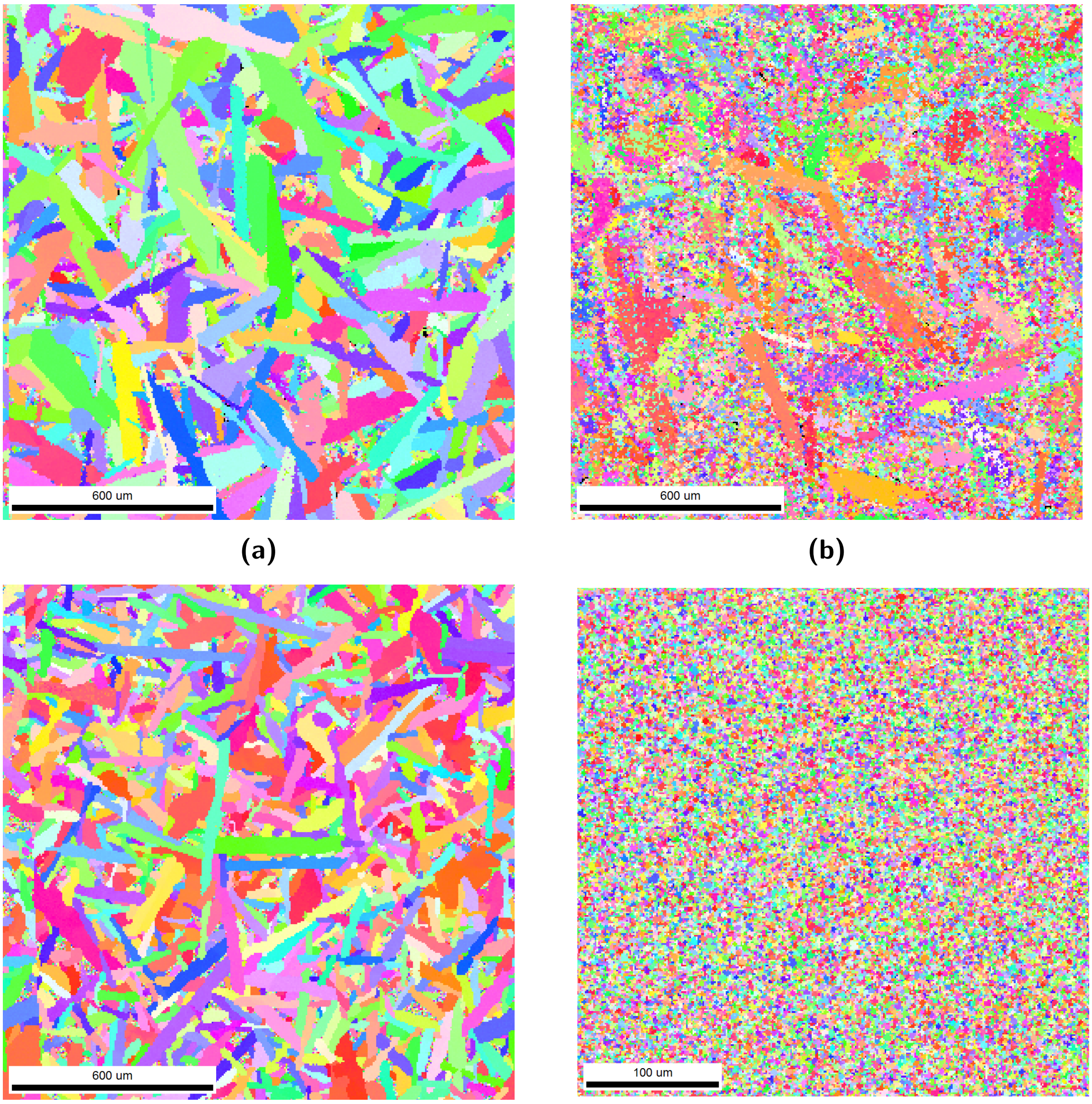

(a) (b)

(c) (d)

Figure 4.5: IPFs obtained from EBSD. a) Sample sintered at 2050 °C and 15 minutes holding time. b) Sample sintered at 2050 °C and 5 minutes holding time. c) Sample sintered at 1850 °C and with a thin carbon paper. d) Sample sintered at 1850 °C and with a thick carbon paper. The colors indicate different orientations of the grains.

4.1.4 Fibers

All the changes done to the sintering parameters also changed the stability and morphology of the fibers in the sintered samples. There were no fibers present after sintering at 2050 °C with a 15 minute holding time, as was also the case during the specialization project. This was also the case when the holding time was reduced to 5 minutes. When the temperature was reduced to 1850 °C, the fibers appeared, although in a deformed state, as seen in Figure 4.6a. The fibers have clearly been in the matrix at some point, but appear to have decomposed and lost their fiber-like properties. They have rough surfaces and have reacted with the matrix. They are more likely just a secondary graphite phase. The fibers also did not stick out of the fracture surface and followed the topography of the fracture. This indicates that they are cut through without providing any toughening to the matrix further supporting the observation that they are a secondary phase.

Figures 4.6b shows the SEM image of the fibers when thick paper was used during sintering. Compared to the sample sintered with thin paper, the fibers have not degraded at all during sintering and appear fiber-like. It can be seen that the fiber is in contact with the matrix but has its original surface morphology. The fracture surface also showed that the fibers had been pulled out during fracture. The diameter of the fibers was also in the range of 7-10 μm as was the case for the original fibers.

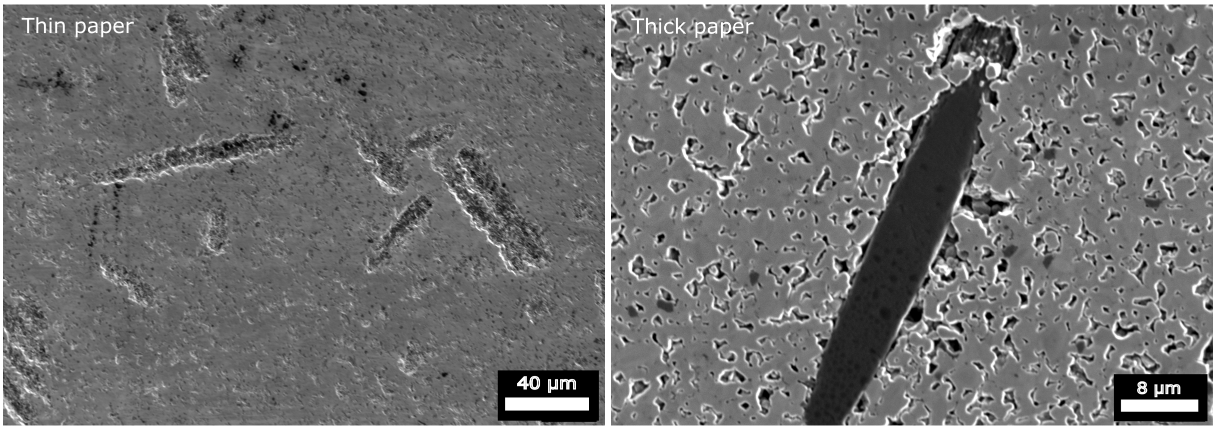

(a) (b)

Figure 4.6: SEM images of the fibers after sintering with a) thin carbon paper and b) thick carbon paper.

4.1.5 Summary of optimization study

The main purpose of the optimization part was to introduce fibers into the matrix while also reducing the grain size of the matrix. The heating rate was increased from 75 ℃/min to 200 ℃/min and sintering temperature was reduced from 2050 ℃ to 1850 ℃. The holding time was also reduced to 3 minutes from 15 minutes. Additionally the thickness of the carbon paper that protects the sample during sintering was increased to 0.25 mm from 0.1 mm. As a result the density went down to 92 % from 98 % and the microstructure showed very small grains with considerable porosity. The fibers, on the other hand, appeared in the matrix after these changes were done and were unharmed during sintering. As the main goal of this thesis is to study the effect of fibers on the SiC matrix and due to time constraints, these sintering parameters were used in further investigation.

4.2 Main Sintering and Characterization

With the fibers in the matrix, this part will focus on the differences between the three samples with 0, 10 and 15 vol% fiber content. The sintering temperature was 1850 ℃, with a heating rate of 200 ℃/min, a holding time of 5 minutes and an applied top pressure of 20 MPa. Thick carbon paper was used for these samples. The results from the sintering data obtained from the SPS, phase composition by XRD, densities by the Archimedes method and microstructure with EBSD will be presented here. The mechanical properties will be presented and finally focus will be given to the fiber/matrix interactions using SEM.

4.2.1 Sintering Curves

The sintering data for the three samples with 0, 10 and 15 vol% carbon fibers can be seen in Figures 4.7a, 4.7b and 4.7c. All the samples show a similar gas evolution, with the silica removal starting at around 1500 ℃ and with a peak at 1800 ℃, just before the top temperature. The shrinkage curves looks similar as well. There is very little change before the removal of silica and the rapid densification starts just after the gas evolution begins. The shrinkage slows significantly by the end of the holding time, though it does not stop completely, meaning densification is still ongoing. The bump in the end is due to pressure release.

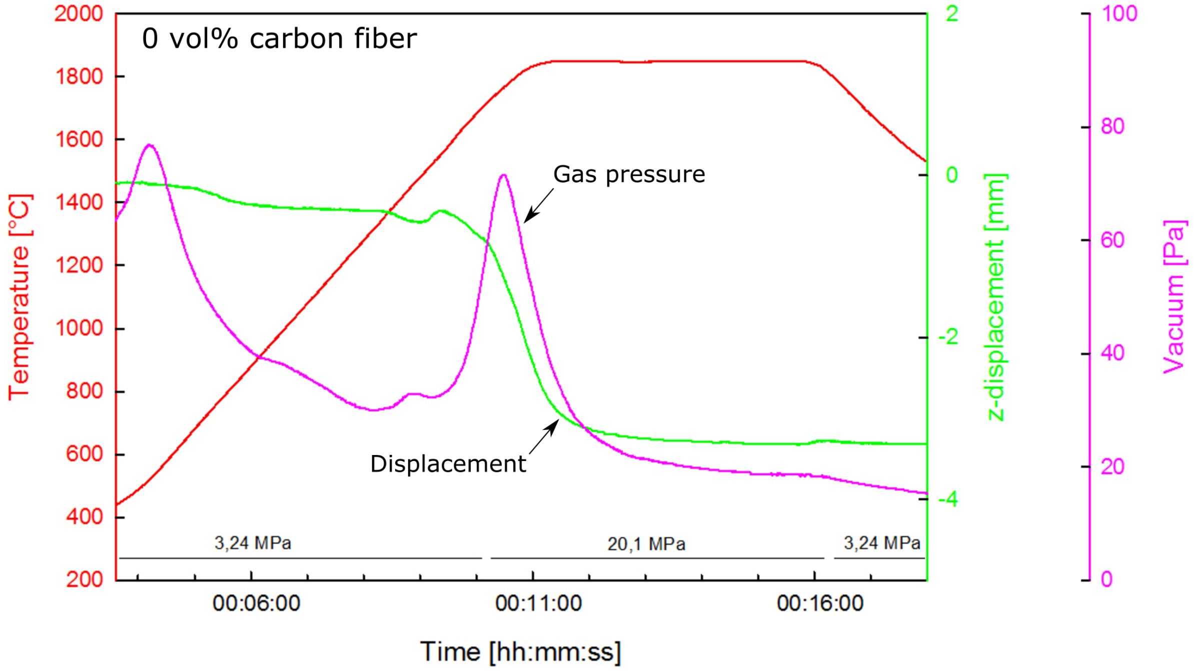

(a)

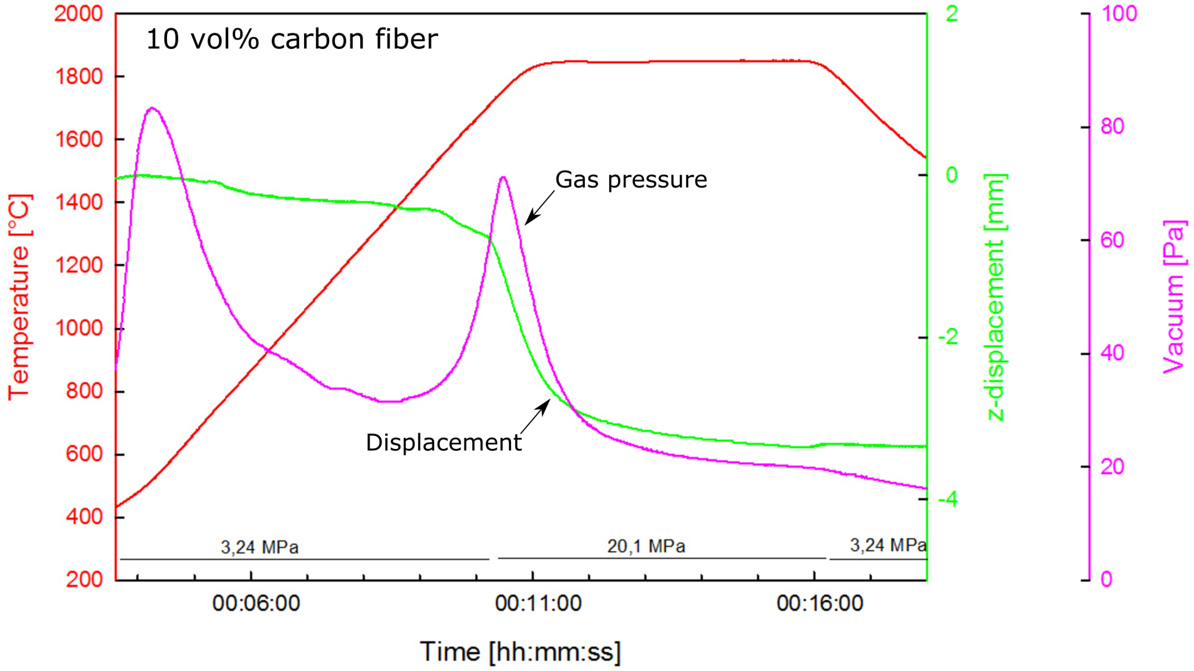

(b)

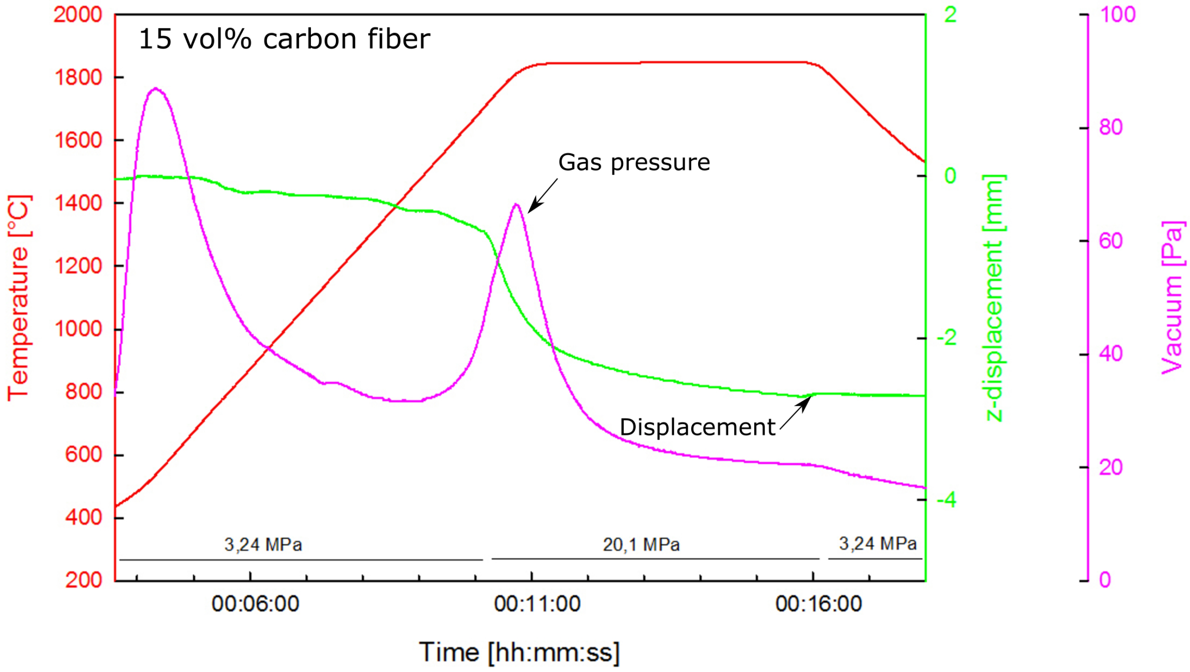

(c)

Figure 4.7: The sintering data gathered from the SPS for samples sintered at 1850 °C. a) The 0 vol% carbon fiber sample. b) The 10 vol% carbon fiber sample. c) The 15 vol% carbon fiber sample. The red curve is the temperature, the green curve is the displacement in the z direction, the pink curve is the chamber vacuum and the black lines show the pressure change.

Figure 4.8a shows a comparison of the gas evolution for all the samples. The 0 and 10 vol% samples show identical peaks, while the peak for the 15 vol% sample lags slightly after and ends up in the top temperature region. This has an effect on the densification of the 15 vol% sample as seen in Figure 4.8b, which shows a comparison of the displacement curves of the samples. Again the first two samples show nearly identical curves, while the rapid densification stops much sooner for the final sample. Also the curve does not flatten out as much, indicating that the densification does not stop by the end of the holding time. The result is a much lower shrinkage for the third sample.

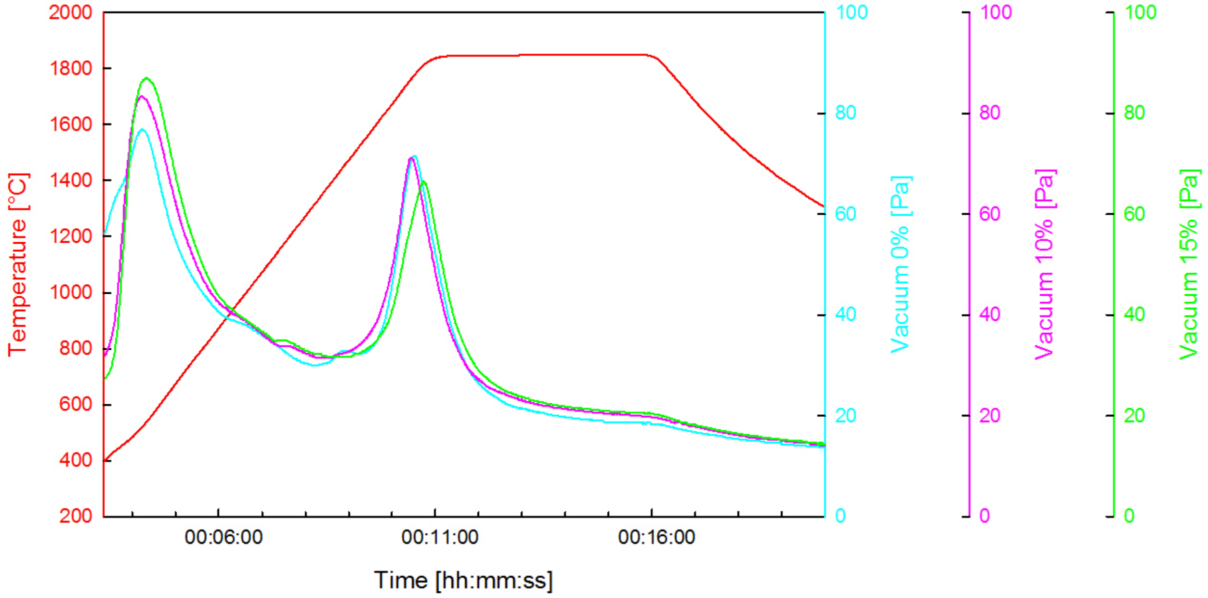

(a)

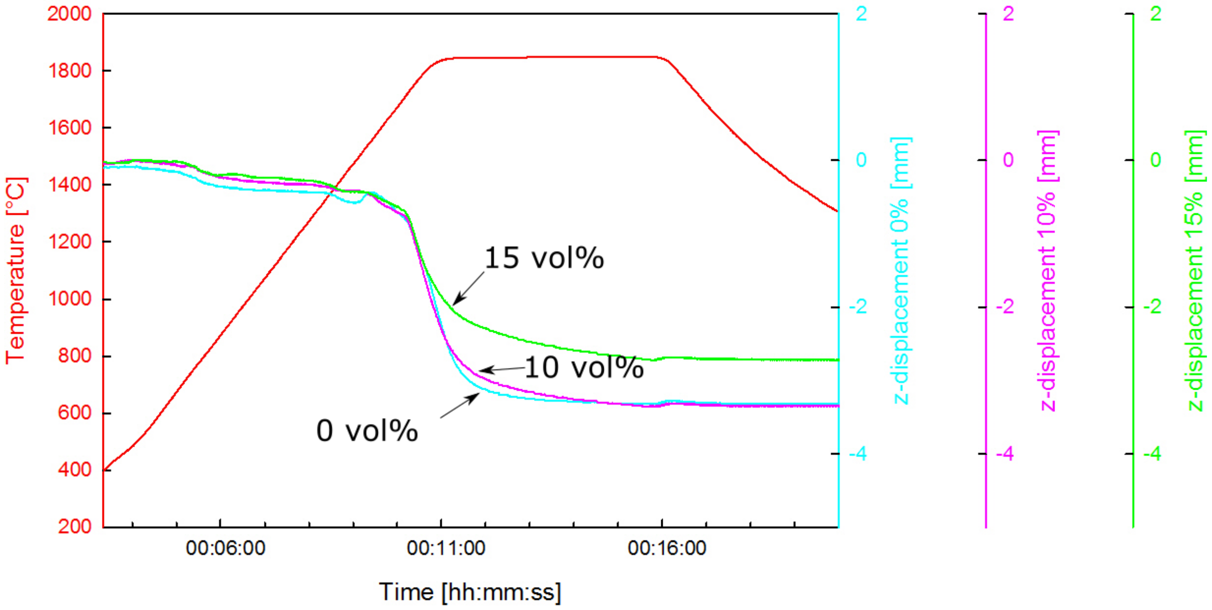

(b)

Figure 4.8: A side by side comparison of a) the chamber vacuum and b) the shrinkage of the 0, 10 and 15 vol% samples.

4.2.2 Phase Composition

The XRD diffractogram for the precursor powders is shown in Figure 4.9. The same polytypes, 6H, 4H and 15R, are present in all samples. The 0 vol% sample, however, seems to have more 4H compared to the others, indicated by the stronger peaks at around 33, 43, 50 and 57 °. No graphite phase is detected in the 0 vol% sample while it can be seen in both 10 and 15 vol% samples as a broad peak around 26 °. This is due to carbon fibers in these samples.

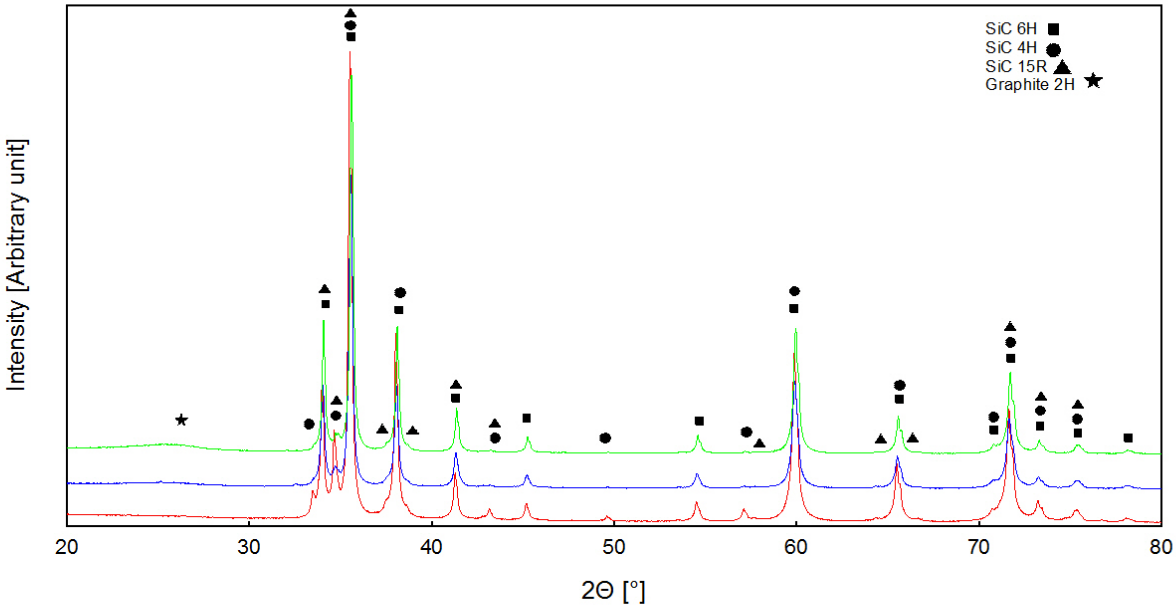

Figure 4.9: The XRD diffractogram of the precursor powders. The square represents SiC 6H (PDF 01-075-8314), the circle SiC 4H (PDF 04-010-5697), the triangle SiC 15R (PDF 00-039-1196) and the star graphite 2H (PDF 00-041-1487).

The wt% of the different phases obtained from Rietveld refinement can be seen in Table 4.1. Again the first sample has a higher amount of both 4H and 15R and no graphite. The two other powders have similar amounts of all the SiC polytypes, with an higher amount of graphite in the 15 vol% powder, as expected. It should be mentioned that it is challenging to get exact values during the refinement and the values change by a few % depending on the parameters used. This gives more of a rough idea of the quantitative phase composition of the samples. Though the graphite phases do match up well with the amount of fibers put in the powders.

Table 4.1: The wt% of the phases present in the precursor powders obtained by Rietveld refinement using the TOPAS software along with the Rwp value of the fitting.

vol% fibers	wt% 6H	wt% 4H	wt% 15R	wt% Graphite	Rwp value
0	68	16	16	0	7.27
10	81	10	3	6	8.77
15	76	7	6	11	8.81

For reference an XRD analysis was also done on just the fibers, as seen in Figure 4.10. The fibers have a strong peak centered around 26 °, with several smaller peaks at higher values. The shape of the peaks are also broad and slightly off-center compared to the graphite peaks found in the database, indicating the lack of defined long-range order.

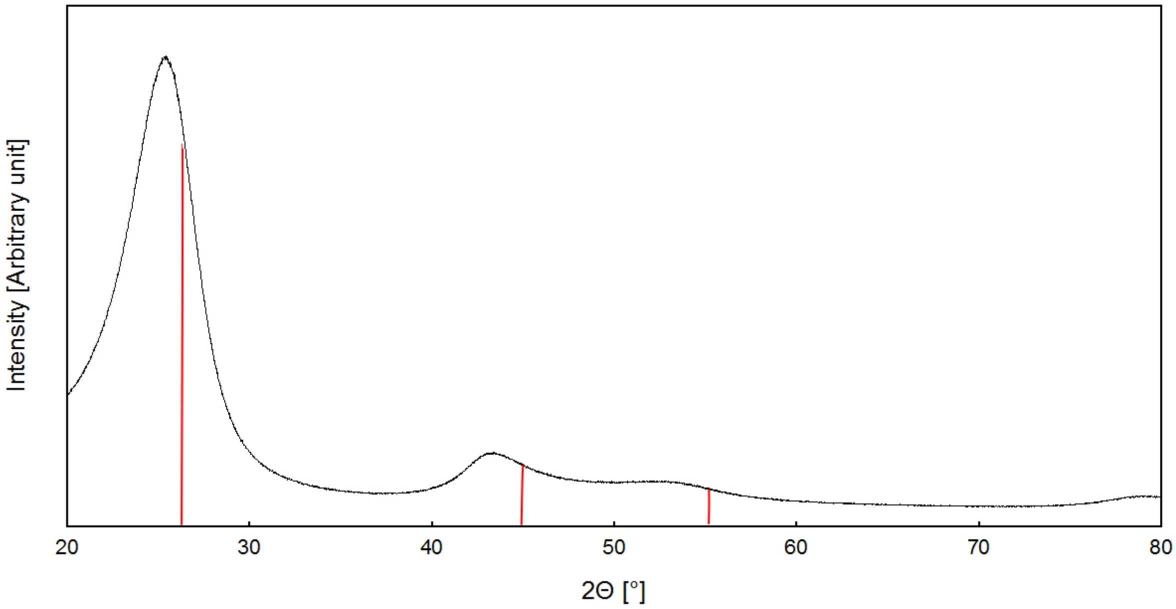

Figure 4.10: The XRD diffractogram of the fibers. The red lines show the major peaks of graphite 2H (PDF 00-041-1487).

The XRD diffractogram for the sintered samples is shown in Figure 4.11. The individual peaks are easier to see and match up with each other and the peaks from the powder analysis. This means that no new phases have been created during sintering. The larger amount of 4H and 15R in the 0 vol% sample can be more clearly seen. The sample also shows a graphite peak now, which is a result of the graphitization of carbon black in the sample. The other two samples show a clearer graphite peak as well, with a broader peak compared to the first sample. This matches up with the broad peak of the fiber diffractogram, but also indicates that the fibers have a more random orientation in the samples.

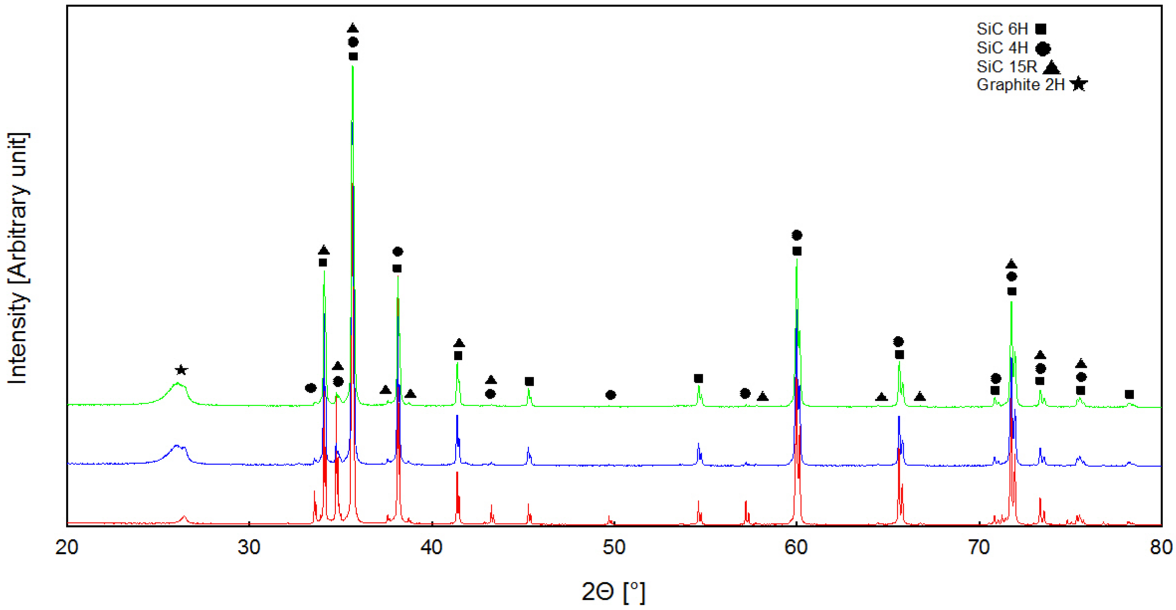

Figure 4.11: The XRD diffractogram of the sintered samples. The square represents SiC 6H (PDF 01-075-8314), the circle SiC 4H (PDF 04-010-5697), the triangle SiC 15R (PDF 00-039-1196) and the star graphite 2H (PDF 00-041-1487).

The wt% of the different phases obtained from Rietveld refinement can be seen in Table 4.2. The amount of 4H is still much higher in the 0 vol% sample than the other samples and has increased by 10 % during sintering. The graphite phase can also be detected. The values in general seem to be similar to the powder values, indicating that the fibers do not affect the phase composition during sintering. Though as mentioned before, some variations do occur by changing the parameters during refinement and these are not absolute values. The most important value is the graphite wt% and it indicates that the fibers have not lost any amount of their original weight.

Table 4.2: The wt% of the phases present in the sintered samples obtained by Rietveld refinement using the TOPAS software with the Rwp value of the fitting.

vol% fibers	wt% 6H	wt% 4H	wt% 15R	wt% Graphite	Rwp value
0	61	25	10	4	10.1
10	82	6	4	8	10.6
15	82	4	3	11	10.8

4.2.3 Densities

The relative densities of the samples with varying carbon fiber content content can be seen in Figure 4.12. The theoretical density used for the reference was that of α-SiC with 3.21 g/cm^3. For the 10 and 15 vol% samples the theoretical density was calculated by rule of mixtures between α-SiC and the fibers, at 3.07 and 3.00 g/cm^3, respectively. The relative densities are similar for the 0 and 10 vol% samples at around 92 % but it drops to 88 % for the 15 vol% sample, which indicates that it has lagged behind the other samples during sintering. Figure 4.13 shows the open and closed porosities of the samples. The open porosity sees an increase through all the samples, 3around 3 % for the 0 vol% sample, 7.5 % for the 10 vol% sample and up to 9.5 % for the 15 vol% sample. Even though the first two samples show similar densities, the difference in open porosity shows that the 10 vol% sample is behind the 0 vol% sample in the sintering cycle. Similarly the closed porosity drops from 4.5 % to around 1 % between the first to the second sample, but then increases again to 2 % for the final sample. There should not be any closed porosity below 92 % relative density and the final two values are a biproduct of the method, as mentioned before.

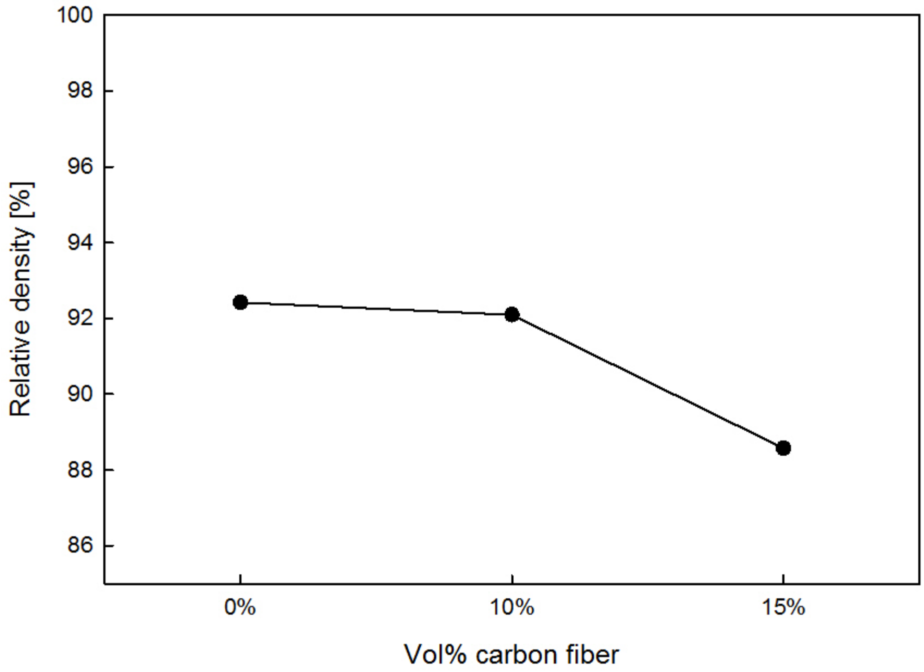

Figure 4.12: The relative densities of the samples with varying carbon fiber content. The lines are a guide to the eye.

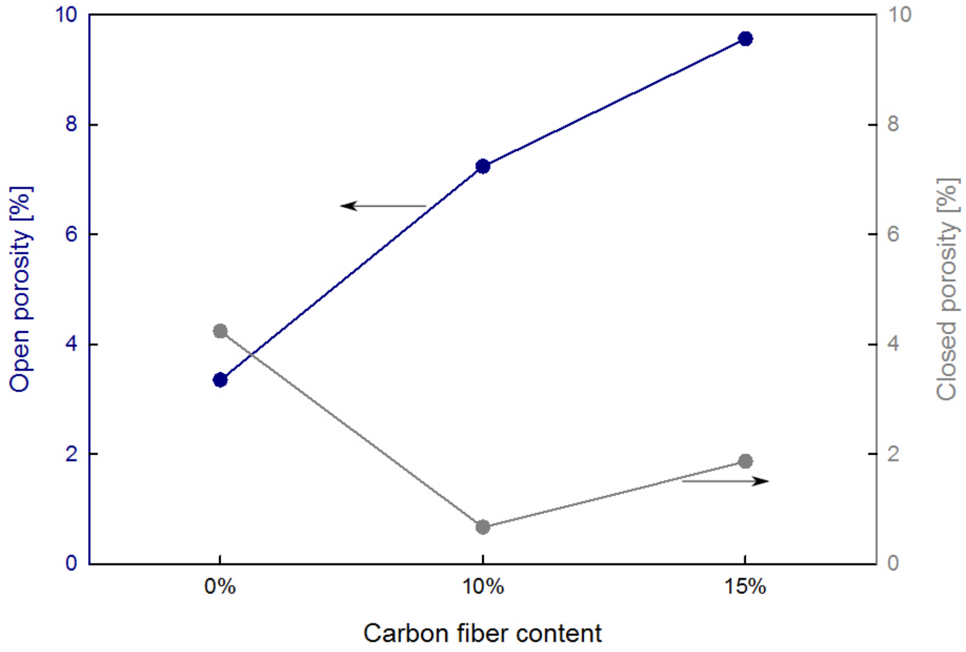

Figure 4.13: The porosities of the samples with varying carbon fiber content. The blue points are the open porosities while the grey points are the closed porosities. The lines are a guide to the eye.

4.2.4 Microstructure

Figures 4.14a, 4.14b and 4.14c show the IPF for the three samples. It can be seen that the grains are smaller than the resolution limit at that magnification. This indicates that no significant grain growth has happened during sintering. From Figure 4.14a it can be seen that the grains are somewhat bigger for the 0 vol% sample than the rest, indicating that it has come further in the sintering cycle. There is no difference between the other two samples. The concentrated green areas in Figures 4.14b and 4.14c are the fibers. SEM images of the polished surfaces of the samples are given in Appendix C.

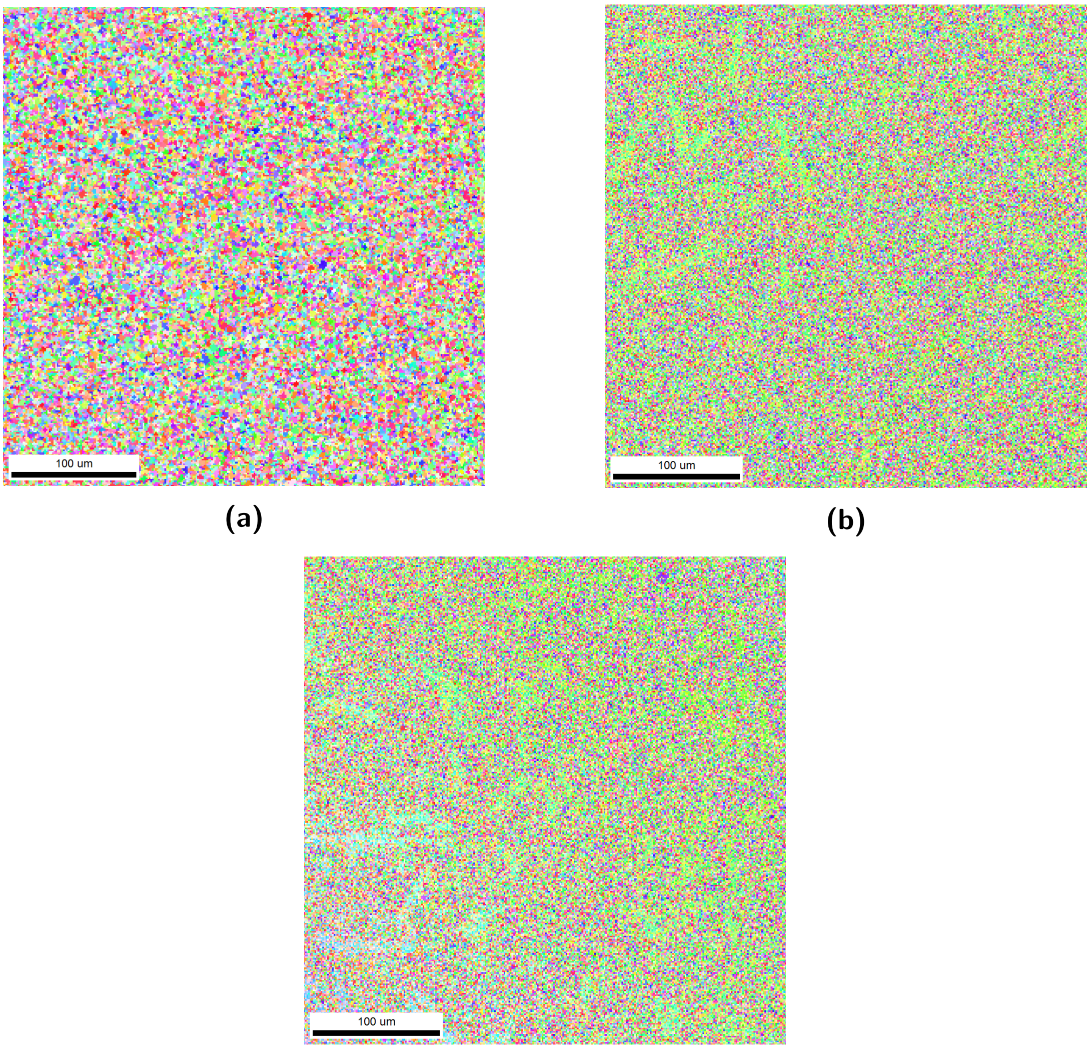

(a)

(b)

(c)

Figure 4.14: The IPFs obtained by EBSD for a) the 0 vol% sample, b) the 10 vol% sample and c) the 15 vol% sample. The colors indicate different orientations of the grains. The concentration of green areas in b) and c) are the fibers.

4.2.5 Mechanical Properties

Figure 4.15 shows the hardness values of the three samples, with 10 indents made on each sample and an average of those indents taken as the value with standard deviation as the error bars. The raw values can be seen in Appendix B. The 0 vol% sample has an average hardness of 2350 HV with little variation. The hardness drops to about 1900 HV for the 10 vol% sample with a much larger variation. For the 15 vol% sample the hardness drops to about 1100 HV with similar variation to that of the previous sample. Representative secondary electron and backscatter electron images of the indents made on each sample can be seen in Figures 4.18a-4.18f.

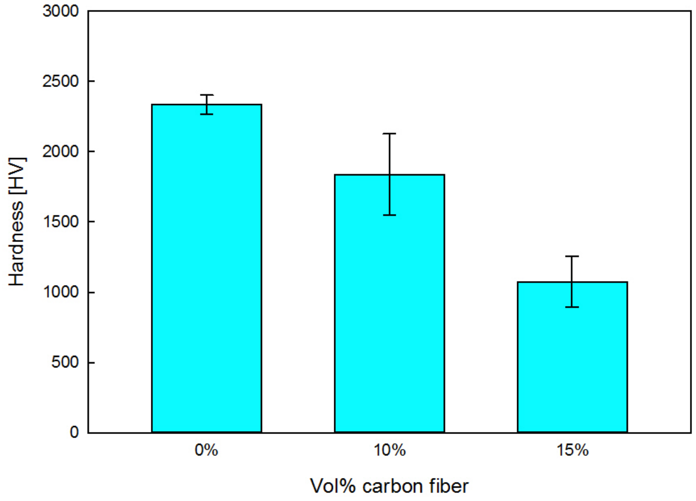

Figure 4.15: The measured hardness of the samples with varying fiber content. The error bars are a standard deviation of ten measurements.

Figure 4.16 shows the fracture toughness values calculated from the same indents as the hardness values, with the error bars as standard deviations. The calculations can be seen in Appendix B. The fracture toughness for the 0 vol% sample is 2.5 MPa$\sqrt{m}$ and increases to 3 and 3.5 MPa$\sqrt{m}$ for the 10 and 15 vol% samples, respectively. There is also little variation for the first sample and a large variation for the other two samples.

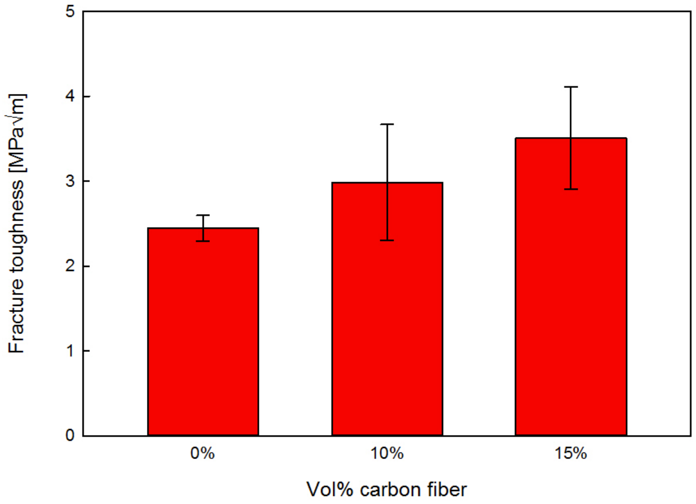

Figure 4.16: The measured fracture toughness of the samples with varying fiber content. The error bars are a standard deviation of ten measurements.

Figure 4.17 shows the flexural strength of the samples done with the ring-on-ring method. The error bars are standard deviations. The raw data can be seen in appendix B. The 0 vol% sample is used as a reference and has strength of 12 MPa. The strength drops to about 8 MPa for the 10 vol% sample and again to around 7 MPa for the 15 vol% sample. The reference had only one sample measured, while the other two had three and four samples, respectively. Their variation is similarly large of about 3 MPa.

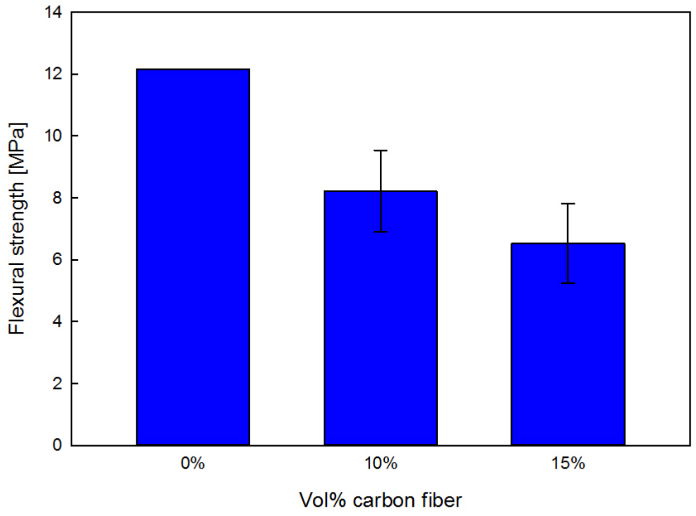

Figure 4.17: The measured flexural strength of the samples with varying fiber content. The error bars are a standard deviation of three and four measurements for the 10 and 15 vol% samples, respectively.

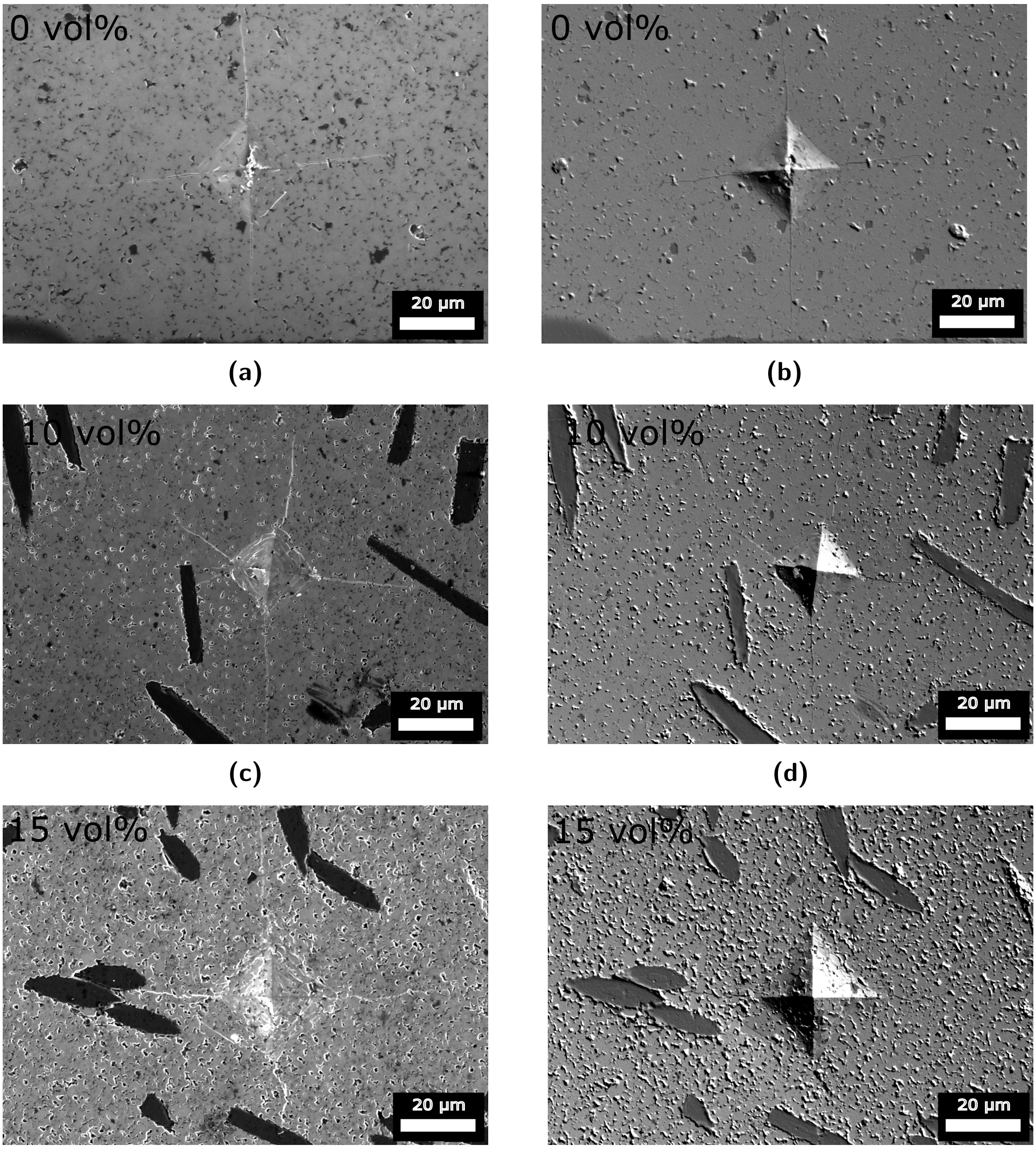

(a) (b)

(c) (d)

(e) (f)

Figure 4.18: Example secondary electron and backscatter electron images of the Vicker's microindents made on the samples with a) and b) 0 vol%, c) and d) 10 vol% and e) and f) 15 vol% carbon fibers.

4.2.6 Fiber/matrix Interaction

The interfaces between the fiber and the matrix for the 10 and 15 vol% samples can be seen in Figures 4.19a and 4.19b, respectively. For the 10 vol% sample, the bonding between the matrix and fiber is a combination of mechanical and chemical. In some places the particles only pressed against the surface of the fiber, while in other places a thin surface layer of SiC had formed on the fibers with neck formation between the particles and the film. This can be seen in Figure 4.19a. There were also instances where the fiber and the matrix bonded directly without a film, as seen in the lower right corner of Figure 4.19a. The 15 vol% sample did not show any signs of film formation and the bonding between the matrix and fibers was mechanical, as seen in Figure 4.19b. In both cases the fibers retain their original form.

There was also significant amount of fiber cluster formation in the samples with the 15 vol% sample having more of them in general. Examples of the clusters can be seen in Figures 4.19c and 4.19d. These clusters added big open pores in the samples and disrupted the general microstructure. It can also be seen that the grains get smaller around the fibers and there is more porosity along the interface, with the 15 vol% sample having larger pores.

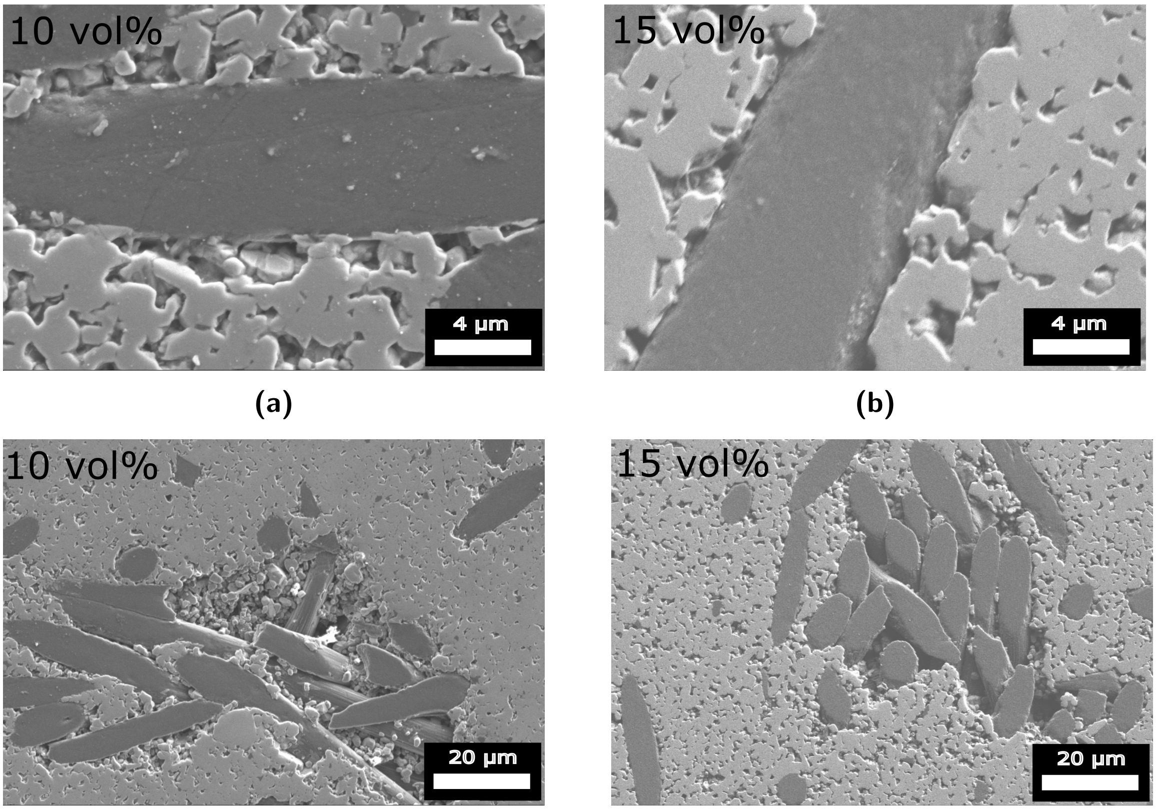

(a) (b) (c) (d)

Figure 4.19: SEM images of the bonding of the matrix and fibers for the a) 10 vol% sample and b) 15 vol% sample as well as the clusters formed in the c) 10 vol% sample and d) 15 vol% sample.

The fracture surface looks similar in both cases. Most of the fibers are oriented orthogonal to the applied pressure direction during sintering. Both fiber pullout and crack bridging are present as toughening mechanisms. Figures 4.20a-4.20d are from the fracture surfaces of the samples with 15 vol% carbon fiber content that were broken during the strength test. Figures 4.20a and 4.20b show fibers that have been pulled out from the matrix, while Figures 4.20c and 4.20d show fibers that have been cut through as a result of crack bridging. The mechanism that is in effect depends on orientation of the fiber to the crack propagation direction. When the crack propagates parallel or close to parallel to the fiber axis, the mechanism is fiber pullout. Crack bridging seems to be the dominating mechanism when the crack propagates orthogonal to the fiber axis. A combination of these mechanisms is present in between these extremes. There are also some fibers that have been cut along the fiber axis.

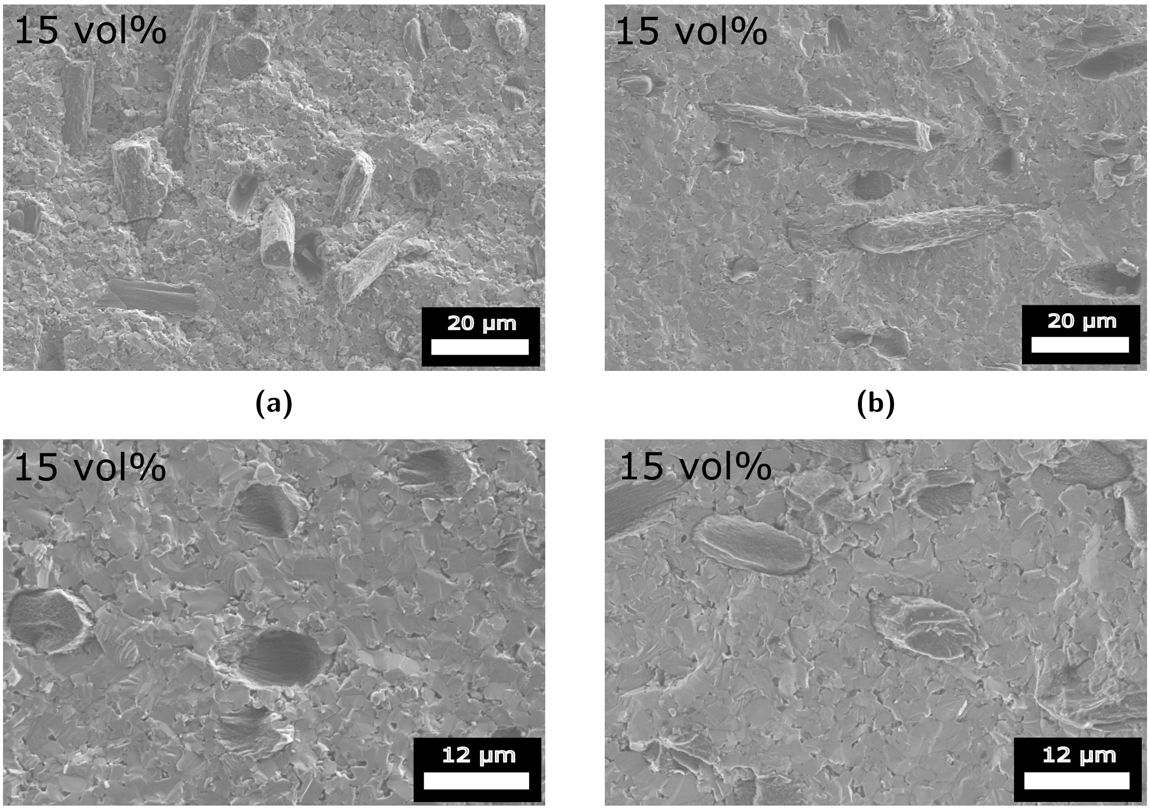

(a) (b) (c) (d)

Figure 4.20: SEM images of the fracture surface. a) and b) show fiber pullout, while c) and d) show cut fibers due to crack bridging. All the images are from the fracture surfaces of the samples with 15 vol% carbon fiber content that were broken during the strength test.

Figures 4.21a-4.22b are from the fracture surfaces of the samples broken with a hammer. Figure 4.21a and 4.21b show the surfaces of a fiber that has bonded with the matrix and been pulled out and a fiber in a cluster of fibers that has not been pulled out. The surface of the fiber that has been pulled out has a lot of surface deformations. The deeper holes have been made by particles pushing against the surface while the shallower scratches are a result of the matrix holding back the fibers during pullout. This indicates that the fibers and the matrix are strongly bonded and extra energy is needed for the fibers to be pulled out. The surface of the fiber that has not bonded with the matrix has a smooth surface similar to the surface of the precursor fibers. This means that heat alone does not deform the fibers at the given sintering parameters.

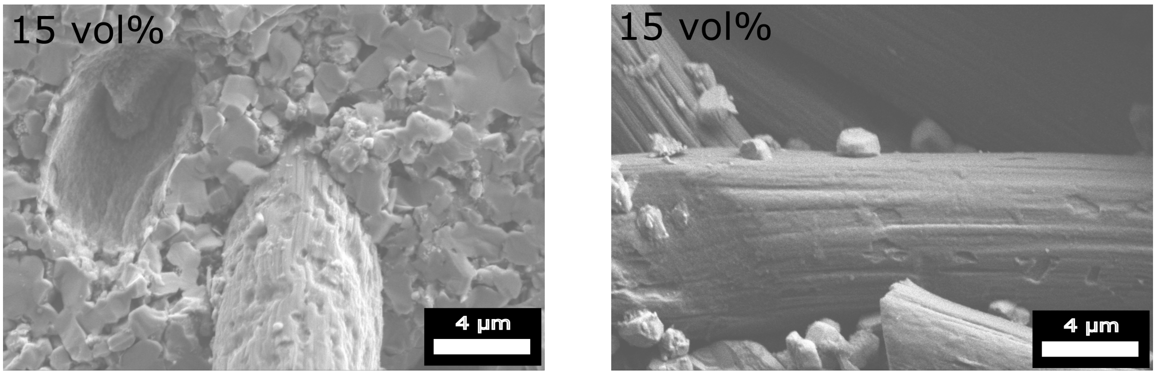

(a) **(b)**

Figure 4.21: a) SEM images of fiber surface of a pulled fiber. b) SEM image of a fiber that has not been pulled. Both images are from the fracture surfaces of the samples broken with a hammer.

Figures 4.22a and 4.22b show the surrounding matrix of the spot from where a fiber has been pulled out for 10 and 15 vol% samples, respectively. Smaller particles surround the fibers than the rest of the matrix in both cases. The particles are more connected and there is less porosity present in the 10 vol% sample than in the 15 vol% sample. This again indicates that there is a stronger bond present between the fibers and the matrix in the 10 vol% sample.

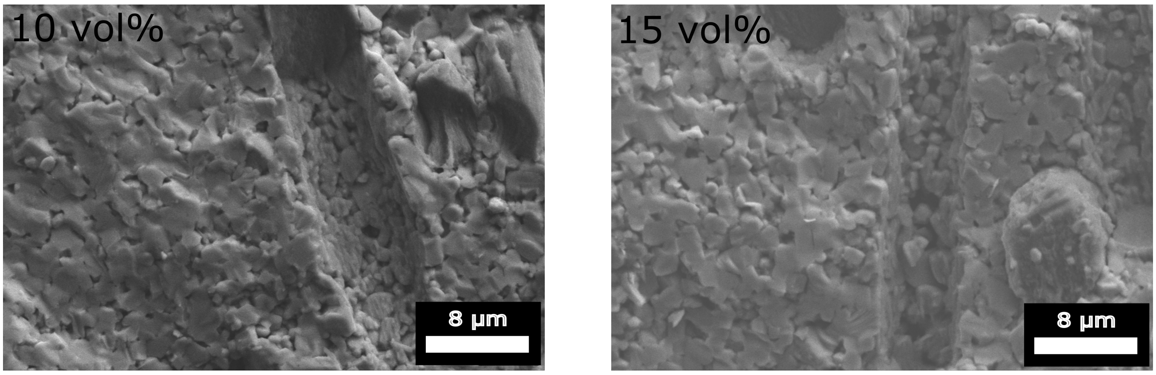

(a) **(b)**

Figure 4.22: a) SEM image of the surrounding matrix of a spot where a fiber has been pulled out in the 10 vol% sample. b) SEM image of the surrounding matrix of a spot where a fiber has been pulled out in the 15 vol% sample. Both images are from the fracture surfaces of the samples broken with a hammer.

5 Discussion

5.1 Optimization of Sintering Parameters

5.1.1 Effect of the Sintering Parameters

The initial sintering temperature of 2050 °C was too high for a method like SPS, which was also concluded by Skarpeid [54]. The shrinkage curves indicate that the densification is done before reaching the top temperature and from there on exaggerated grain growth occurs, which is also backed up by the near theoretical densities. Figure 4.5a shows large elongated grains, typical for a pressure assisted method like SPS. The grains flatten out orthogonal to the pressure direction and some grains will have preferential driving force in that direction. This makes these grains grow faster and consume grains which have other growth directions. This results in very long grains, which can effect the mechanical properties. There was little effect on the densities and microstructure by reducing the holding time to 5 minutes. Figure 4.5b still shows large elongated grains, which further confirms that the sintering temperature is too high.

The decision to reduce the sintering temperature was in part due to literature [48,49] and in part due to observations on the sintering curves. The densifcation seemed to stop at around 1850 °C, so that was chosen to be the new temperature. The heating rate was increased to 200 °C/min to get to the sintering window as fast as possible to avoid powder coarsening. As no densification happens before the silica layer is removed from the particles, the heating rate can be even higher. The holding time was also reduced to 3 min due to both 15 and 5 minutes being too long holding times for SPS. This program resulted in similarly high densities and a microstructure with smaller grains. From Figure 4.5c it can be seen that there are still long grains present, which is mostly because of the applied pressure. They are, however, much thinner and there is a larger amount of smaller grains present. These results indicate that these changes were a step in the right direction.

5.1.2 Effect of Carbon Paper Thickness

Even though the density and microstructure indicated a good sintering program, the fibers showed significant degradation, as seen in Figure 4.6a. The thin paper often fractured during sintering and left the powder without protection. This resulted in the sample sticking to the dies. The carbon paper thickness was increased to create a stable environment for the powder during sintering. The paper no longer fractured and the sample did not stick to the die. The difference can also be seen in the densification curves for the two paper thicknesses, Figures 4.1a and 4.1b. The latter curve is much smoother and does not have the initial movement at the start of the holding time. The bump is most likely a result of the fracture of the carbon paper, which would cause the sample to move slightly.

Although the fibers showed no degredation, the density of the sample went down to 90 %. By looking at Figure 4.2a it can be seen that there is a significant delay of the gas evolution for the sample sintered with a thick paper. As the chamber pressure is measured outside the die, the peaks represent a difference in how long the gas is held in the die before it reaches the gauge. Most probably the gases start to evolve at the same time around the same temperature, as the papers have no effect on the temperature curve. The surface silica reacts with carbon and SiO and CO gasses are produced, by Equation 2.8. The volatile SiO gas reacts further with carbon by Equation 2.9 and SiC and more CO gas are created. As the thick paper is less permeable to gases, the CO gas builds up around the powder and the atmosphere becomes saturated with CO. This significantly reduces the driving force of silica removal due to Le Chatelier's principle and as a result little to no densification can happen. At some point the paper will not be able to hold the gas that has built up and it is released in a burst, indicated by the more rapid gas evolution compared to the thin paper sample. After that the reactions proceed normally and there is no more gas buildup, resulting in rapid, though delayed, densification. For the thin paper, there is no gas buildup and the densification starts when the reaction starts. The density of the sample suggest that the sintering has not yet reached the final sintering stage. The fact that most of the porosity is open also supports this. This explains the lack of large grains in the microstructure, as grain growth dominates during the final sintering stage.

The stability of the fibers can be explained in a similar way. CO gas can itself react with silica by Equation 5.1 and form SiO and carbon dioxide gases.

$$\mathrm{CO\,(g) + SiO_2(s) \longrightarrow SiO\,(g) + CO_2(g)} \tag{5.1}$$

The presence of carbon dioxide creates an oxidizing environment for carbon, which is then oxidized to CO via the Boudard reaction, Equation 5.2.

$$\mathrm{CO_2(g) + C\,(s) \longrightarrow 2\,CO\,(g)} \tag{5.2}$$

As silica is removed, more carbon dioxide is created. With thin carbon paper, the CO gas leaves the die, increasing the driving force of carbon oxidation. As the fibers are mostly made of carbon and most of the carbon black is being used up by the removal silica, the fibers are more accessible to the carbon dioxide gas and are consumed as a result. With thick carbon paper, however, there is a gas buildup, which decreases the driving force of carbon oxidation and as a result the fibers are not consumed. The composition of the gas should be measured for a more detailed analysis.

The change to thick carbon paper is beneficial from the stability of the fibers point of view. To achieve higher densities either the temperature or the holding time should be increased to account for the delay of the densification. Further optimization should have been conducted, but the SPS unit broke down and the samples made with this program were characterized instead due to time constraints.

5.2 Main Sintering

5.2.1 Sintering Curves

The sintering curves look similar to the final curve of the optimization step. The rapid densification starts when silica is removed and slows down after the silica has been removed.

The shrinkage curves flatten out by the end of the holding time, but the densifcation does not stop completely. As mentioned in the optimization step, this indicates that the sintering is not completely finished and either a higher temperature or holding time is needed.

There is a significant difference in the shrinkage curves between the 15 vol% carbon fiber sample and the other samples, seen in Figure 4.8b. The rapid densification stops much sooner indicated by the earlier flattening of the curve, though it does not flatten as much as the other two curves. This results in less overall densification and that there is more densification going on at the end of the sintering cycle. There is also a slight difference between the curves of the 0 and 10 vol% carbon fiber samples. The latter curve flattens out a little sooner than the former, but again it doesnt flatten out as much. Both curves end up at the same overall densification by the end of the sintering cycle.

The differences between the curves suggest that it takes longer to completely sinter the samples with an increasing carbon fiber content and that the same program can not be used for all the samples. As the gas evolutions are similar for all samples, Figure 4.8a, the difference must be because of the composition of the samples and not due to silica removal. The main difference in composition is the fiber content and the fibers can obstruct the densification of the matrix by clustering together. The other difference in composition is the extra carbon black added to protect the fibers. As mentioned in the theory section, adding too much carbon will have a negative effect on the densification of SiC. This, however, is less likely as the two samples with fibers had the same added amount of extra carbon black and the curves have large differences. In the end, the sintering parameters should be tailored for each sample with emphasis on similar densities and microstructures.

5.2.2 Phase Composition

The phase compositions of the precursor powders are similar with two exceptions. Firstly, the powder with no fibers has a larger amount of both the 4H and 15R polytypes. This is due to the SiC in that powder coming form a different batch, while the powders with fibers have the same batch as a base. Secondly, the graphite phase increases with addition of fibers, as expected. Even though the fibers have no long range crystalline structure, they still show a broad peak around the expected graphite peak. No such peak is found in the reference powder, as carbon black is amorphous. The difference between the powders with fibers is due to fiber addition, which skews the weight percentages by a similar amount.

The phase composition of the sintered samples are similar as well. There are small changes in the wt% of the phases, but this is more due to the limitations of fitting the curves during Rietveld refinement as SiC has a complex crystal structure. The lack of big changes in the amount of polytypes in the samples with fibers indicates that fibers do not affect the stability and transformation of the polytypes. The graphite phase has a more defined peak for all samples, which is due to some of the carbon black graphitizing and forming a secondary phase in the samples. The shape of the peak in the samples with fibers is still broader than in the sample without fibers. This indicates that the fibers themselves have not graphitized during sintering as they retain their lack of long range crystal structure. No other new phases were detected in the samples.

5.2.3 Densities

From Figure 4.12 it can be seen that there is little change in density between the first two samples, while the 15 vol% sample shows significantly less density. This can be directly related to the shrinkage curves discussed earlier. The 15 vol% sample has not undergone as much densification as the other samples during the sintering program. The 0 and 10 vol% samples ended up at a similar shrinkage during sintering and therefore also have a similar density. The porosity, Figure 4.13, tells us that there is also a difference between the 0 and 10 vol% samples, a s the latter has much more open porosity while the former has a both open and closed porosity. This difference can also be seen in the shrinkage curve and shows that the 10 vol% sample lags a little behind the 0 vol% sample in densification. The 15 vol% sample has more, mostly open, porosity, as expected with the lower density.

Some of the open porosity and lower density is also a contribution of the clusters of fibers formed in the samples, as seen in Figures 4.19c and 4.19d. These create very large voids around the fibers as SiC granulates are not able to pass the tight spaces created by the fibers. A higher pressure could be applied to force the granulates into these voids to fill them.

5.2.4 Microstructure

The microstructures of the samples show that there are very small grains present. This is expected from densities of 92 % and lower, due to most of the grain growth taking place during the final sintering stage. The grains are most likely smaller than the resolution limit at the given magnification in Figures 4.14a-4.14c. The reference sample seems to have slightly larger grains, indicating that it has just entered the final stage of sintering. Higher magnification should have been used based on the densities as the initial average grain diameter of the SiC powder with 13 m^2/g specific surface area is around 150 nm. However, this would have just confirmed that the samples have not yet reached the final stage of sintering. The area around the fibers, seen on the IPFs as concentrated green areas, should have been investigated to determine if the fibers have an effect on the microstructure immediately surrounding them.

5.2.5 Mechanical Properties

At first glance, the hardness values seem to correlate to the density values, with the most dense sample, the 0 vol% sample, having the highest hardness and the least dense, the 15 vol% sample having the lowest hardness. While density and porosity does have an effect on hardness, as indicated by the much lower than theoretical hardness value for the first sample, fibers seem to also affect the hardness values. The 0 and 10 vol% samples have a similar density, while the hardness of the latter is much lower with a larger variance. The Vicker's microindentation is a very local measurement method and the position of the indent to the fibers had a big influence on the values. The measured hardness was in general lower close to fibers than in areas where there were no fibers. The bonding between the matrix and fibers is much weaker than than between the grains in the matrix, lowering the hardness. In the 15 vol% sample there were even fewer areas where the fibers did not influence the hardness. The indent should be made with a smaller diamond tip, to get more accurate hardness values for the matrix or a bulk hardness measurement method should be used.

The fracture toughness values show an opposite trend to the hardness values. Since hardness has an inverse proportionality to the fracture toughness when Equation 3.2 is used, lower hardness values would correlate to higher fracture toughness. However, the fibers also influence the values. The length of the cracks propagating from the indent had uniform values for the reference sample, which contribute to a small variance. The samples with fibers have a much larger variance, as the crack length varied a lot depending on if a fiber was hit or not. The 15 vol% sample had a higher chance for the cracks to hit the fibers, giving this sample a higher fracture toughness. Again because this measurement method is very localized it does not show the complete picture. A bulk measurement method, like the notched-beam method, would be a better option.

The flexural strength values again have a decreasing trend through the samples. Some of it is due to the porosity, as pores introduce a lot of defects into the matrix which in turn are detrimental to the strength of the samples. Though the densities of the 0 and 10 vol% samples are similar, the latter has more open porosity giving it a lower strength. Though the decrease between these samples is much larger than the decrease between the samples with fibers, indicating that the fibers themselves also influence the strength values. Another detrimental effect the fibers have on the matrix are the clusters of fibers, which create local weakpoints. Completely dense samples should be made to get a better understanding of the effect of the fibers on the strength of the material. Also more sample should be made to get better statistics as these values are based on only a few samples. This, however, was not possible in the present work as the SPS unit broke down before more samples could be made.

The values for the mechanical properties obtained in this work differ significantly from the values from the literature given in the theory section. The main reason for this is the difference in relative density. All of the experiments found in literature achieved higher densities, most to near theoretical densities. As porosity affects the mechanical properties more than the fibers, the mechanical properties are much lower when porosity increases. The powders used in literature were also different, consisting mostly of nanosized β-SiC, which will affect the grain size and mechanical properties differently than the sub-micron α-SiC used in this work. The fiber content varied also in literature, from as low as 1 vol% to as high as 33 vol%. Finally there was also a difference in measurement methods. Three-point bending was the prevalent strenght measurement method while the notched beam method was the most used fracture toughness measurement method.

5.2.6 Fiber/Matrix Interaction

There are two different bonding mechanisms present between the fibers and the matrix. The mechanical bonding is most likely caused by the applied pressure which forces the particles against the fibers. This does not break the fibers as the stress on the fiber is compressive and the fibers have a high compressive strength and only leaves indents on the surface. The places where the particles are in contact with the fiber surface act like anchor points and hold the fibers back during fracture. This leads to significant surface deformation of the fibers, but also increases the energy needed to fracture the matrix.

The chemical bonding creates a thin film of SiC on the surface of the fibers, seen in Figure 4.19a. Since the fibers are mostly made of carbon, the film of SiC might form by a reaction between the silica on the surface of the particles and the carbon in the fibers, similar to the reaction in the Acheson process given in Equation 2.1. The sintering temperature of 1850 °C falls into the range where this reaction can happen at 1700-2500 °C. It is not possible to determine what polytype of SiC this thin film is by SEM, so transmission electron microscopy should be used to analyze the thin film. Fibers that have bonded chemically with the matrix should require more energy to pull out during fracture than those that are bonded mechanically and this contribute more to the fracture toughness of the material. There were more of these bonds in the 10 vol% sample than in the 15 vol% sample, indicating that density and sinterability has an effect on the formation of these bonds.

The fibers are mostly oriented in a plane that is perpendicular to the direction of the applied pressure. They did not have a preferred orientation in that plane and were more or less randomly distributed in the matrix, with the exception of the large clusters observed. The fibers tend to stick to each other when they get close, so a homogenization step prior to sintering should be added, such as ultrasonication in ethanol.

The type of toughening mechanism present is affected by the angle between the fiber orientation and the crack propagation direction. Fiber pullout was seen more when the angle was low, while crack bridging was present when the angle was close to 90 °. As the fibers do not have a preferred orientation in the plane perpendicular to the applied pressure direction, the average toughening is a combination of these two mechanisms. This would also mean that the toughening is only in effect when stress is applied in one direction. To get composite that is strong in all directions, the fibers should be oriented randomly in all directions. This is difficult to achieve with pressure assisted sintering like the SPS, so pressureless sintering could be used to investigate this, with green bodies made by isostatic pressing.

6 Conclusion

SiC powders with 0, 10 and 15 vol% carbon fiber content were sintered using the spark plasma sintering method. A sintering optimization step was performed to introduce the fibers into the matrix with a final sintering temperature of 1850 °C, top pressure of 20 MPa and a holding time of 5 minutes. After sintering, the samples were characterized according to phase composition, density, microstructure and mechanical properties. The interaction between the fibers and the matrix was also analyzed. The main results are summarized below.

- The thickness of the carbon paper used to protect the sample during sintering had an effect on the stability of the fibers and the density of the samples. The fibers did not degrade when a thicker paper (0.25 mm) was used compared to a thinner paper (0.1 mm) while the densification of the samples was delayed when thicker paper was used compared to a thinner paper.
- Fiber content affected the densities of the samples when the same sintering parameters were used, from 92 % for the sample without fibers down to 88 % for the sample with 15 vol% fibers.
- The phase composition was largely unaffected by the addition of fibers.
- The hardness of the matrix decreased with fiber addition and the proximity of the fibers affected the hardness values.
- The fracture toughness of the samples increased with fiber addition but was dependent on whether the cracks came in contact with the fibers or not.
- The strength of the samples decreased with fiber addition.
- The fibers were oriented orthogonal to the direction of the applied pressure during sintering. Both mechanical and chemical bonding was observed between the fibers and the matrix.
- The dominating toughness mechanisms were fiber pullout and crack bridging, depending on the fiber orientation to the crack propagation direction. In the bulk of the

material both mechanisms were present in equal amounts and the average toughening was a combination of the two.

7 Future work

The sintered samples were not fully dense and had a considerable porosity in the structure. The sintering program should be further optimized to get fully dense samples by either increasing the sintering temperature or the holding time. The focus should still be the stability of the fibers in the matrix. As the amount of fibers affects the sinterability, the sintering parameters should be tailored individually for each sample. More samples should be made to test reproducibility and to get more statistics on the measured values.

The bonding and film formation between the fibers and the matrix should be investigated more closely by transmission electron microscopy. The strength of the bonds should also be investigated as well as their formation mechanisms.

Finally, since this is a bulk composite material, all the mechanical properties should be measured by a bulk measuring method. This is especially true for fracture toughness measurements, as localized methods like the Vicker's microindentation do not give the complete picture of the bulk properties of the material. For this the notched-beam method would give more reliable results.

References

[1] Webmineral, "moissanite". `http://www.webmineral.com/data/Moissanite.shtml#.W8r5tnszZhE`. Accessed: 20.10.2018.

[2] Saint-Gobain, "Silicon Carbide Production Process". `https://www.sic.saint-gobain.com/about-us/silicon-carbide-production-process`. Accessed: 20.10.2018.

[3] Branko Matovic and Toyohiko Yano. *Silicon Carbide and Other Carbides*, pages 225–244. Academic Press, 2013.

[4] Rebecca Cheung. *Silicon Carbide Microelectromechanical Systems for Harsh Enviornments*, page 3. ICP, Imperial College Press, 2006.

[5] Misasa Okayama, "VESTA crystallographic data". `http://www.misasa.okayama-u.ac.jp/~masami/pukiwiki/index.php?Vesta_data`. Accessed: 21.10.2018.

[6] G.L. Harris and INSPEC (Information service). *Properties of Silicon Carbide*. EMIS datareviews series. INSPEC, Institution of Electrical Engineers, 1995.

[7] N.W. Jepps and T.F. Page. Polytypic transformations in silicon carbide. *Progress in Crystal Growth and Characterization*, 7(1):259 – 307, 1983.

[8] Yoshizo Inomata, Zenzabro Inoue, Mamoru Mitomo, and Hiroshige Suzuki. Relation between growth temperature and the structure of sic crystals grown by the sublimation method. *Journal of the Ceramic Association, Japan*, 76:313–319, 01 1968.

[9] W.F. Knippenberg. *Growth Phenomena in Silicon Carbide*. Philips research reports. N. V. Philips' Gloeilampenfabrieken, 1963.

[10] P.A. Kistler-De Coppi and W Richarz. Phase transformation and grain growth in silicon carbide powders. *International Journal of High Technology Ceramics*, 2:99–113, 12 1986.

[11] N. I. Krasotkina, V. S. Yakovleva, N. I. Voronin, and S. P. Shmitt-Fogelevich. Stability of silicon carbide to hydrofluoric, nitric, and sulfuric acids. *Refractories*, 9(11):723–726, Nov 1968.

[12] Shur M.S. Levinshtein M.E., Rumyantsev S.L. *Properties of Advanced Semiconductor Materials: GaN, AlN, SiC, BN, SiC, SiGe*, pages 93–148. John Wiley & Sons, Inc., New York, 2001.

[13] D. N. Talwar and Joseph C. Sherbondy. Thermal expansion coefficient of 3c–sic. *Applied Physics Letters*, 67(22):3301–3303, 1995.

[14] A.W. Weimer. *Carbide, Nitride and Boride Materials Synthesis and Processing*, pages 115–128. Springer Netherlands, 2012.

[15] G. S. Gupta, P. Vasanth Kumar, V. R. Rudolph, and M. Gupta. Heat-transfer model for the acheson process. *Metallurgical and Materials Transactions A*, 32(6):1301–1308, Jun 2001.

[16] Tygre, "production of a high value ceramic material: Silicon carbide". `http://www.tygre.eu/cms/project/production`. Accessed: 16.04.2019.

[17] D. Richerson, D.W. Richerson, and W.E. Lee. *Modern Ceramic Engineering: Properties, Processing, and Use in Design, Third Edition*. Materials Engineering. Taylor & Francis, 2005.

[18] M.N. Rahaman. *Ceramic processing and sintering*. Materials engineering. M. Dekker, 1995.

[19] I.J. McColm and N.J. Clark. *Forming, shaping, and working of high performance ceramics*. Blackie, 1988.

[20] Zhijian Shen, Mats Johnsson, Zhe Zhao, and Mats Nygren. Spark plasma sintering of alumina. *Journal of the American Ceramic Society : a monthly journal devoted to the arts and sciences related to the silicate industries*, 85(8):1921–1927, 2002.

[21] Z. A. Munir, U. Anselmi-Tamburini, and M. Ohyanagi. The effect of electric field and pressure on the synthesis and consolidation of materials: A review of the spark plasma sintering method. *Journal of Materials Science*, 41(3):763–777, Feb 2006.

[22] U. Anselmi-Tamburini, J.E. Garay, Z.A. Munir, A. Tacca, F. Maglia, and G. Spinolo. Spark plasma sintering and characterization of bulk nanostructured fully stabilized zirconia: Part i. densification studies. *Journal of Materials Research*, 19(11):3255–3262, 2004.

[23] Olivier Guillon, Jesus Gonzalez-Julian, Benjamin Dargatz, Tobias Kessel, Gabi Schierning, Jan Räthel, and Mathias Herrmann. Field-assisted sintering technology/spark plasma sintering: Mechanisms, materials, and technology developments. *Advanced Engineering Materials*, 16(7):830–849, 2014.

[24] Denis Yushin, Andrey Vladimirovich Smirnov, Nestor Solis Pinargote, Pavel Peretyagin, and Ramón Torrecillas. Modeling process of spark plasma sintering of powder materials by finite element method. *Materials Science Forum*, 834:41–50, 11 2015.

[25] Dustin M. Hulbert, André Anders, Joakim Andersson, Enrique J. Lavernia, and Amiya K. Mukherjee. A discussion on the absence of plasma in spark plasma sintering. *Scripta Materialia*, 60(10):835 – 838, 2009.

[26] Zhao-Hui Zhang, Zhen-Feng Liu, Ji-Fang Lu, Xiang-Bo Shen, Fu-Chi Wang, and Yan-Dong Wang. The sintering mechanism in spark plasma sintering – proof of the occurrence of spark discharge. *Scripta Materialia*, 81:56 – 59, 2014.

[27] D Schwesig, G Schierning, R Theissmann, N Stein, N Petermann, H Wiggers, R Schmechel, and D E Wolf. From nanoparticles to nanocrystalline bulk: percolation effects in field assisted sintering of silicon nanoparticles. *Nanotechnology*, 22(13):135601, feb 2011.

[28] John S. Nadeau. Very high pressure hot pressing of silicon carbide. *American Ceramic Society Bulletin*, 52:170–174, 02 1973.

[29] Nobuyuki Tamari, Takahiro Tanaka, Koji Tanaka, Isao Kondo, Masakazu Kawahara, and Masao Tokita. Effects of spark plasma sintering on the densification and mechanical properties of silicon carbide. *Journal of the Ceramic Society of Japan*, 103(1199):740–742, 1995.

[30] Takeshi Yamamoto, Hidetoshi Kitaura, Yasuhiro Kodera, Takashi Ishii, Manshi Ohyanagi, and Zuhair A. Munir. Consolidation of nanostructured β-sic by spark plasma sintering. *Journal of the Ceramic Society of Japan*, 87(8):1436–1441, 2004.

[31] S. Hayun, V. Paris, R. Mitrani, S. Kalabukhov, M.P. Dariel, E. Zaretsky, and N. Frage. Microstructure and mechanical properties of silicon carbide processed by spark plasma sintering (sps). *Ceramics International*, 38(8):6335 – 6340, 2012.

[32] Svante Prochazka. *Sintering of Silicon Carbide*, pages 421–431. Springer US, Boston, MA, 1975.

[33] William J. Clegg. Role of carbon in the sintering of boron-doped silicon carbide. *Journal of the American Ceramic Society*, 83(5):1039–1043, 2000.

[34] M. S. Datta, A. K. Bandyopadhyay, and B. Chaudhuri. Sintering of nano crystalline α silicon carbide by doping with boron carbide. *Bulletin of Materials Science*, 25(3):181–189, Jun 2002.

[35] Ludoslaw Stobierski and Agnieszka Gubernat. Sintering of silicon carbide i. effect of carbon. *Ceramics International*, 29:287–292, 12 2003.

[36] Y. Murata and H. Smoak. *Densification of Silicon Carbide by the Addition of BN,BP and B4C, and Correlation to Their Solid Solubilities.*, pages 382–392. Association of Science Document Information: Hakone, Japan., 1978.

[37] Yo Tajima and W. D. Kingery. Solid solubility of aluminum and boron in silicon carbide. *Journal of the American Ceramic Society*, 65(2):C-27–C-29, 1982.

[38] K.K. Chawla. *Ceramic Matrix Composites*. Springer US, 2013.

[39] D.J. Johnson. Structure property relationships in carbon fibers. *J. Phys. D: Appl. Phys.*, 20(3):287–291, 1987.

[40] M. Guigon, A. Oberlin, and G. Desarmot. Microtexture and structure of some high tensile strength, pan-base carbon fibres. *Fibre Science and Technology*, 20(1):55 – 72, 1984.

[41] D.D. Edie. The effect of processing on the structure and properties of carbon fibers. *Carbon*, 36(4):345 – 362, 1998.

[42] I. Mochida, S.-H. Yoon, N. Takano, F. Fortin, Y. Korai, and K. Yokogawa. Microstructure of mesophase pitch-based carbon fiber and its control. *Carbon*, 34(8):941 – 956, 1996.

[43] Yaodong Liu and Satish Kumar. Recent progress in fabrication, structure, and properties of carbon fibers. *Polymer Reviews*, 52(3):234–258, 2012.

[44] Marilyn MInus and Satish Kumar. The processing, properties, and structure of carbon fibers. *JOM*, 57(2):52–58, Feb 2005.

[45] D.D. Edie, K.E. Robinson, O. Fleurot, S.P. Jones, and C.C. Fain. High thermal conductivity ribbon fibers from naphthalene-based mesophase. *Carbon*, 32(6):1045 – 1054, 1994.

[46] Nakano Kikuo, Kamiya Akira, Ogawa Hiroyuki, and Nishino Yoichi. Fabrication and mechanical properties of carbon fiber reinforced silicon carbide composite ceramics. *Journal of the Ceramic Society of Japan*, 100(1160):472–475, 1992.

[47] Nakano Kikuo, Kamiya Akira, Nishino Yoichi, Imura Toru, and Tsu-Wei Chou. Fabrication and characterization of three-dimensional carbon fiber reinforced silicon carbide and silicon nitride composites. *Journal of the American Ceramic Society*, 78(10):2811–2814, 1995.

[48] Yusheng Ding, Shaoming Dong, Zhengren Huang, and Dongliang Jiang. Fabrication of short c fiber-reinforced sic composites by spark plasma sintering. *Ceramics International*, 33(1):101 – 105, 2007.

[49] Ehsan Ghasali, Masoud Alizadeh, Amir Hossein Pakseresht, and Touradj Ebadzadeh. Preparation of silicon carbide/carbon fiber composites through high-temperature spark plasma sintering. *Journal of Asian Ceramic Societies*, 5(4):472–478, 2017.

[50] ZOLTEK, "Carbon fiber properties". `http://zoltek.com/products/px35/`. Accessed: 10.05.2019.

[51] International Organization for Standardization, "Determination of bulk density, apparent porosity and true porosity". `https://www.iso.org/standard/56179.html`. Accessed: 08.12.2018.

[52] Lise Donzel and Steve G. Roberts. Microstructure and mechanical properties of cubic zirconia (8ysz)/sic nanocomposites. *Journal of the European Ceramic Society*, 20(14):2457 – 2462, 2000.

[53] Kedar Kirane, Zdeněk P. Bažant, and Goangseup Zi. Fracture and size effect on strength of plain concrete disks under biaxial flexure analyzed by microplane model m7. *Journal of Engineering Mechanics*, 140(3):604–613, 2014.

[54] H. Skarpeid. The effect of carbon and boron carbide additions in pressure assisted sintered silicon carbide. Master's thesis, Norwegian University of Science and Technology (NTNU), 2017.

[55] M. Madsen. Ceramic matrix composites based on silicon carbide and carbon fibers. Specialization project, Norwegian University of Science and Technology (NTNU), 2018.

Appendix A Equations

A.1 Equations for Archimedes method

The density of isopropanol dependent on the temperature:

$$\rho_{liq} = -0.0009T + 0.8018 \tag{A.1}$$

The bulk density was calculated from:

$$\rho_b = \frac{m_1}{m_3 - m_2} \cdot \rho_{liq} \tag{A.2}$$

The apparent porosity was calculated from:

$$\pi_a = \frac{m_3 - m_1}{m_3 - m_2} \cdot 100 \tag{A.3}$$

The total porosity was calculated from:

$$\pi_t = \frac{\rho_t - \rho_b}{\rho_t} \cdot 100 \tag{A.4}$$

Appendix B Raw data

B.1 Additional sintering curves

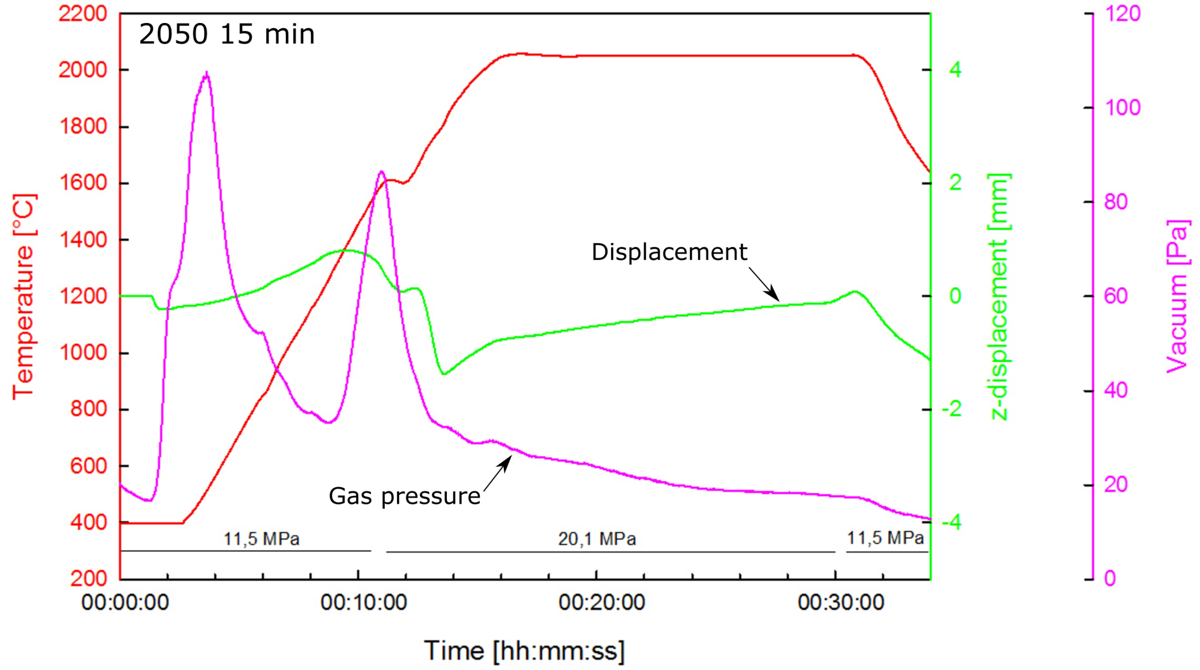

(a)

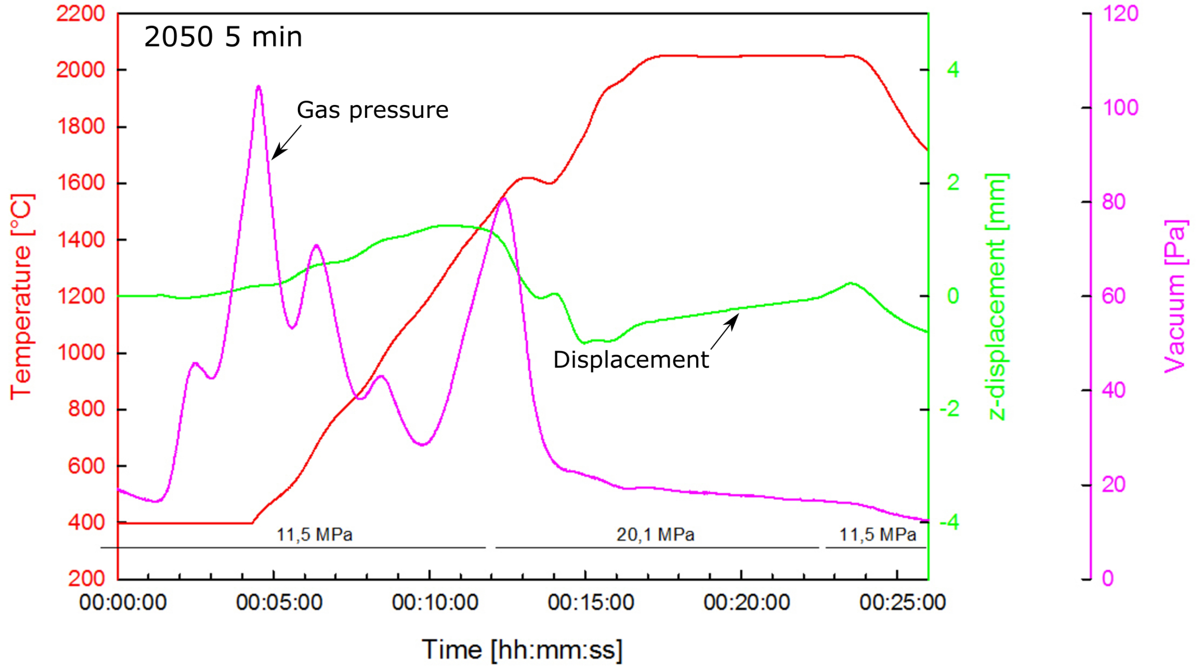

(b)

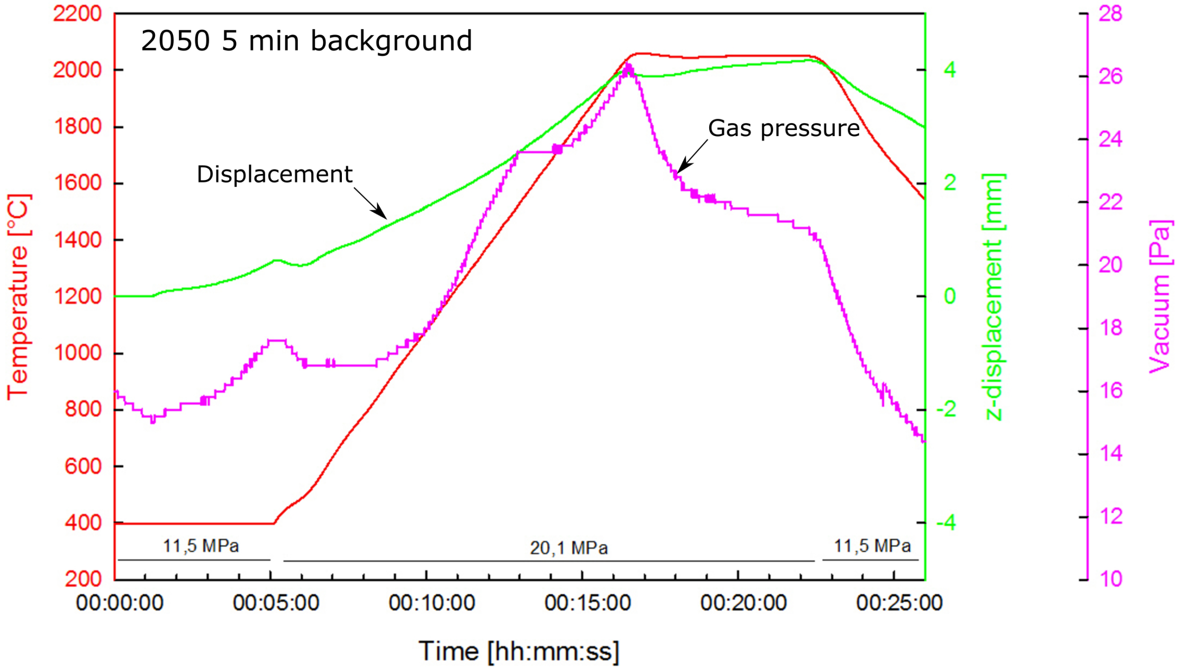

(c)

Figure B.1: The sintering data gathered from the SPS for samples with 0 vol% carbon fibers sintered at a) 2050 °C for 15 minutes and b) 2050 °C for 5 minutes. c) The background data gathered without a sample powder sintered at 2050 °C for 5 minutes. The red curve is the temperature, the green curve is the displacement in the z direction, the pink curve is the chamber vacuum and the black lines show the pressure change.

B.2 Density

Table B.1: The density, relative density, open porosity and closed porosity for the samples sintered during the optimization step.

Sample	Density [g/cm^3]	Relative density [%]	Open porosity [%]	Closed porosity [%]
2050 ℃ 15 minutes	3.13	97.6	1.08	1.35
2050 ℃ 5 minutes	3.15	98.2	0.71	1.09
1850 ℃ thin paper	3.11	97.2	0.65	2.19
1850 ℃ thick paper	2.89	90.2	8.18	1.66

Table B.2: The density, relative density, open porosity and closed porosity for the samples with 0, 10 and 15 vol% fibers.

Sample	Density [g/cm^3]	Relative density [%]	Open porosity [%]	Closed porosity [%]
0 vol% carbon fibers	2.97	92.4	3.35	4.23
10 vol% carbon fibers	2.82	92.1	7.24	0.67
15 vol% carbon fibers	2.65	88.6	9.56	1.87

B.3 Hardness and fracture toughness

Table B.3: The hardness, average crack length and fracture toughness of the sample with 0 vol% carbon fiber.

Hardness [HV]	Average crack length [$\mu\mathrm{m}$]	Fracture toughness [$\mathrm{MPa}\sqrt{\mathrm{m}}$]
2283	42.0	2.47
2251	43.4	2.36
2459	42.4	2.35
2402	44.8	2.19
2348	43.4	2.32
2283	39.9	2.67
2332	42.1	2.43
2316	41.6	2.49
2269	41.4	2.53
2399	39.1	2.67

Table B.4: The hardness, average crack length and fracture toughness of the sample with 10 vol% carbon fiber.

Hardness [HV]	Average crack length [$\mu\mathrm{m}$]	Fracture toughness [$\mathrm{MPa}\sqrt{\mathrm{m}}$]
2131	36.5	3.16
1380	32.6	4.63
2026	43.0	2.53
1974	46.2	2.30
2252	45.7	2.19
2033	39.2	2.90
1749	38.8	3.18
1544	43.0	2.90
1749	38.8	3.18
1544	43.0	2.90

Table B.5: The hardness, average crack length and fracture toughness of the sample with 15 vol% carbon fiber.

Hardness [HV]	Average crack length [$\mu\mathrm{m}$]	Fracture toughness [$\mathrm{MPa}\sqrt{\mathrm{m}}$]
1033	47.7	3.03
1268	41.6	3.36
902	37.2	4.70
1373	35.7	4.06
978	50.9	2.83
1195	41.7	3.45
896	46.1	3.43
952	47.0	3.22

Table B.6: The flexural strength values of the samples measured with the ring-on-ring method.

Sample	vol% carbon fiber	Flexural strength [MPa]
0% str-1	0	12.16
10% str-1	10	7.34
10% str-2	10	9.74
10% str-3	10	7.58
15% str-1	15	7.11
15% str-2	15	5.98
15% str-3	15	5.05
15% str-4	15	7.99

Appendix C SEM images

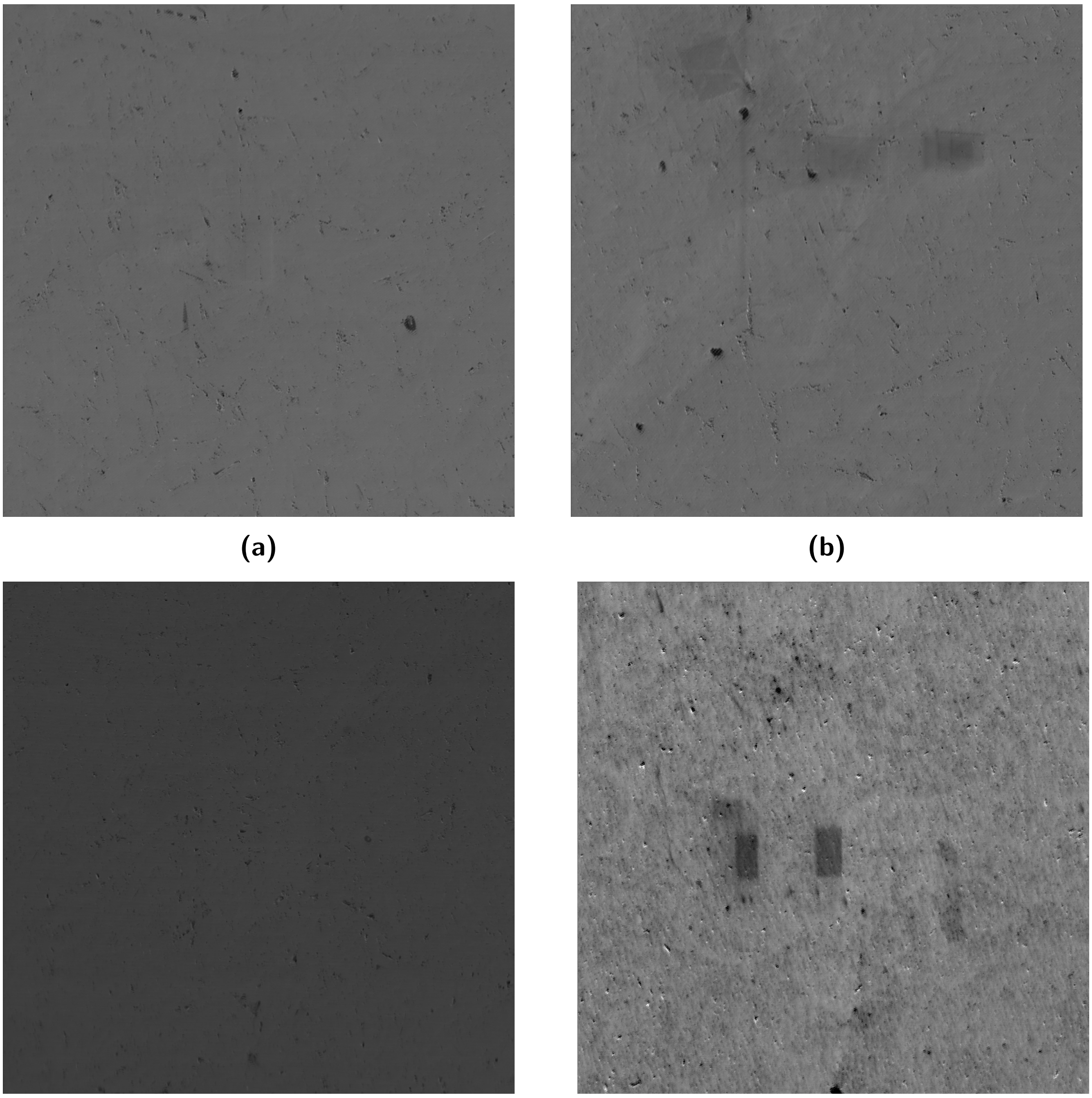

(a) (b)

(c) (d)

Figure C.1: SEM images from which the IPFs were made for microstructure analysis during the optimization step.

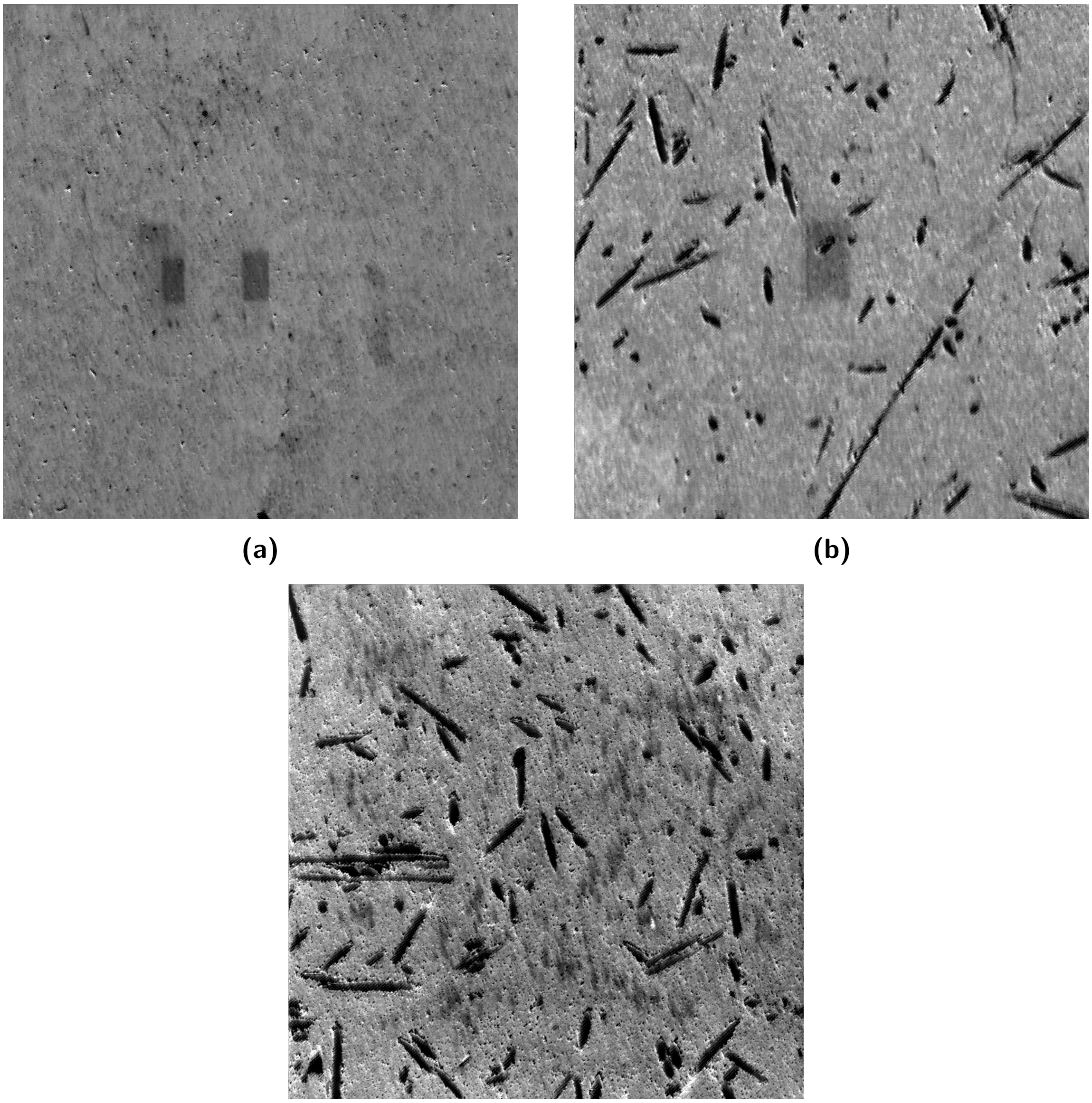

(a)

(b)

(c)

Figure C.2: SEM images from which the IPFs were made for microstructure analysis of the samples with 0, 10 and 15 vol% carbon fiber content.

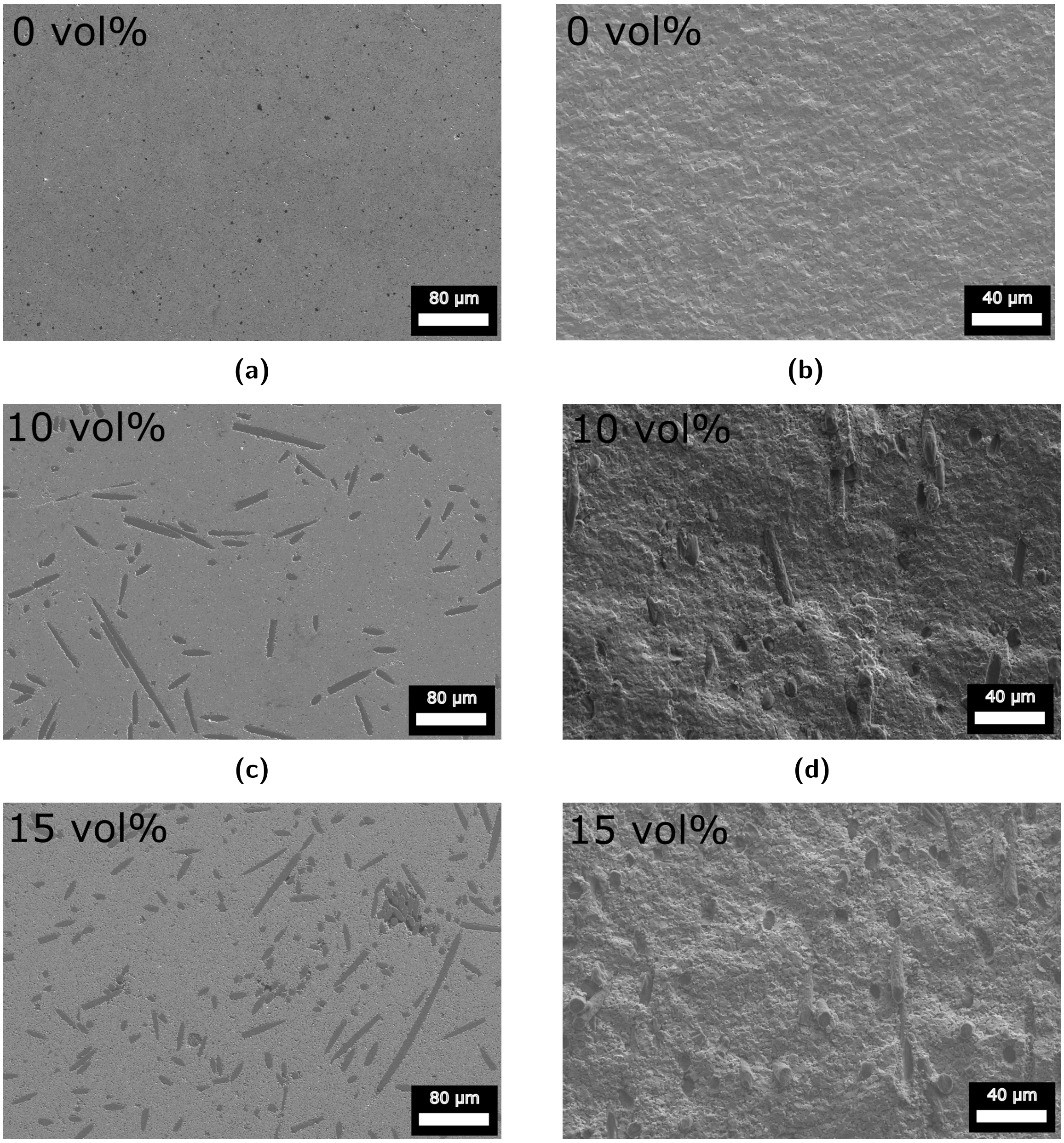

(a) **(b)** **(c)** **(d)** **(e)** **(f)**

Figure C.3: SEM images of the polished and fracture surfaces of the samples with a) and b) 0 vol%, c) and d) 10 vol% and e) and f) 15 vol% carbon fibers.